# AN EXPERIMENTAL INVESTIGATION OF WATER INFLUENCE ON DRY FORWARD IN-SITU COMBUSTION

A Thesis

by

PHILIPP KUDRYAVTSEV

Submitted to the Office of Graduate and Professional Studies of
Texas A&M University
in partial fulfillment of the requirements for the degree of

MASTER OF SCIENCE

| | |
|---|---|
| Chair of Committee, | Berna Hascakir |
| Committee Members, | Maria A. Barrufet |
| | Eduardo Gildin |
| Head of Department, | A. Daniel Hill |

December 2013

Major Subject: Petroleum Engineering

# ABSTRACT

In-situ combustion (ISC), also known as fire flooding, is not a new thermal enhanced oil recovery (EOR) technique. It is a potential alternative for heavy oil production when other thermal EOR methods are not adequate in certain reservoir conditions. A number of successful ISC application examples have been amply covered in the literature; however, the technique is still not widely used. Additional research on the influence of heterogeneities on ISC performance is required to improve predictability of this promising EOR technique.

To investigate the influence of initial water saturation on ISC performance, seven combustion tube experiments were conducted. The experimental investigations were performed on a Canadian bitumen sample (7.5 $^{o}$API) from the Peace River region. During the experimental runs, initial bitumen saturation varied between 31.23% and 54.86%. Initial water saturation varied between 0% and 36.87%.

Temperature distribution along the combustion tube and effluent gas composition were recorded for each run and further analyzed. ISC dynamics were also investigated in terms of liquid production and postmortem analysis. Combustion front dynamics were interpreted with a CT scanner and a numerical simulation was used to obtain a chemical reaction scheme for one of the experiments.

The results showed that initial water saturation is a critical parameter to determine the success of dry forward combustion.

# DEDICATION

I dedicate the effort put into this thesis to my dear mother. Thank you for all you have done for me.

# ACKNOWLEDGMENTS

First of all, I would like to thank my advisor at Texas A&M, Professor Berna Hascakir, for guiding and tutoring me. Dr. Hascakir, thank you for motivating and supporting me. I am grateful to you because you have taught me so much. It has been an honor to know you and work with you.

I would also like to give special thanks to Professor Maria A. Barrufet who served as my committee member and allowed me to use the Ramey Thermal Recovery Laboratory. I would like to express gratitude to Dr. Barrufet for establishing a joint program between Texas A&M University and the Gubkin Russian State University (RSU) of Oil and Gas.

I would like to acknowledge Professor Eduardo Gildin for serving as my committee member and for his consultations on the numerical simulation part of my thesis. His assistance helped me greatly.

I would like to thank Dr. Dualat Mamora for equipping the Ramey Thermal Recovery Laboratory.

I would also like to thank the entire faculty and staff of the Harold Vance Department of Petroleum Engineering for making my time at Texas A&M University memorable.

I devote special thanks to Professor Anatoly B. Zolotukhin, who made the greatest contribution on the Russian side in establishing the joint program. Managing many international programs, Dr. Zolotukhin has provided bright opportunities for the most talented graduate students of Gubkin RSU.

I would also like to thank Professor Igor T. Mischenko, department head of the oil field development faculty at Gubkin RSU. I became a specialist through Professor Mischenko's wisdom and knowledge, and he always provided strong support.

Additionally I want to express gratitude to Dmitry N. Lambin, International Program Coordinator, for his continued assistance in every aspect of studying abroad.

I would also like to give praise to Alexey V. Dengaev and Vladimir S. Verbizky for useful knowledge and valuable life lessons.

Special acknowledgement goes to Alexey A. Khrulenko, Artem V. Fomkin, and Sergey S. Urazov, who also contributed to my educational process. These kind people shared their knowledge and helped me to understand the peculiarities of ISC modeling.

Finally, I would like to thank my closest friends Denis, Yusuf, Alexey, and Alen. I am the only child in my family, but throughout the years they have become like brothers to me.

# TABLE OF CONTENTS

Page

ABSTRACT .......... ii

DEDICATION .......... iii

ACKNOWLEDGMENTS .......... iv

TABLE OF CONTENTS .......... vi

LIST OF FIGURES .......... vii

LIST OF TABLES .......... x

CHAPTER I INTRODUCTION AND LITERATURE REVIEW .......... 1

CHAPTER II EXPERIMENTAL PROCEDURE .......... 14

- II.1. Experimental setup .......... 14
- II.2. Sample characterization .......... 18
- II.3. Bitumen dewatering .......... 19
- II.4. Experimental procedure .......... 19

CHAPTER III EXPERIMENTAL RESULTS AND DISCUSSION .......... 23

CHAPTER IV NUMERICAL SIMULATION .......... 68

CHAPTER V CONCLUSIONS AND RECOMMENDATIONS .......... 82

NOMENCLATURE .......... 85

REFERENCES .......... 88

APPENDIX A .......... 100

# LIST OF FIGURES

Page

Figure 1. World energy consumption by fuel types, 1990-2035 (Conti et al. 2011) ........1

Figure 2. Thermal EOR techniques classification (adapted from (Farouq Ali et al. 1994))........................................................................................................2

Figure 3. ISC scheme (adapted from (DOE 2013))..........................................................4

Figure 4. Oil-sand micro-structure (Mossop 1982)..........................................................8

Figure 5. The effect of steam on coke yield from bitumen coking at 450 $^{o}$C (adapted from (Dutta et al. 1999)) ....................................................................12

Figure 6. ISC setup........................................................................................14

Figure 7. ISC setup scheme (adapted from (Mamora et al. 1993)).................................15

Figure 8. Peace River oil sands location (adapted from (Hein 2000))............................18

Figure 9. Temperature profiles in time for all experiments ............................................24

Figure 10. Temperature profiles in position for all experiments.....................................28

Figure 11. Temperature profiles for the 37 cm position below the air injection point ....30

Figure 12. Heating rates for the 37 cm position below the air injection point................31

Figure 13. The combustion front position in time..........................................................32

Figure 14. Combustion front velocities at stable zone ....................................................33

Figure 15. Gas composition profiles for all experiments................................................34

Figure 16. $CO_2$ profile comparisons.......................................................................36

Figure 17. Experimental average values for the $CO_2$ concentration in the mole percentage..................................................................................................38

Figure 18. Temperature front profile vs. $CO_2$ profile.....................................................39

Figure 19. Average and maximum combustion front temperatures ................................ 40

Figure 20. Cumulative liquid production and oil recovery ............................................ 42

Figure 21. Oil upgrading ................................................................................................ 44

Figure 22. Air injection time vs. oil recovery factor ...................................................... 46

Figure 23. Cumulative oil recovery vs. time ................................................................. 47

Figure 24. Oil production start time ............................................................................... 48

Figure 25. Postmortem photographs, E1-E5 .................................................................. 49

Figure 26. Postmortem photographs, E6-E7 .................................................................. 50

Figure 27. Average CT number in position for all postmortem samples ........................ 58

Figure 28. Cross-sectional images for E1: $S_{oi}$ = 33.64%; $S_{wi}$ = 0% ................................ 60

Figure 29. Cross-sectional images for E2: $S_{oi}$ = 33.77%; $S_{wi}$ = 34.05% .......................... 61

Figure 30. Cross-sectional images for E3: $S_{oi}$ = 52.43%; $S_{wi}$ = 0% ................................ 62

Figure 31. Cross-sectional images for E4: $S_{oi}$ = 54.12%; $S_{wi}$ = 17.85% .......................... 63

Figure 32. Air bypassing around the thermowell (from E4 postmortem) ........................ 64

Figure 33. Cross-sectional images for E5: $S_{oi}$ = 53.02%; $S_{wi}$ = 35.63% .......................... 65

Figure 34. Cross-sectional images for E6: $S_{oi}$ = 31.23%; $S_{wi}$ = 0% ................................ 66

Figure 35. Cross-sectional image for E7: $S_{oi}$ = 54.86%; $S_{wi}$ = 36.87% ........................... 67

Figure 36. Grid sizes used in the simulation study ......................................................... 69

Figure 37. Two phase relative permeability curves ........................................................ 71

Figure 38. Viscosity variation with temperature ............................................................. 74

Figure 39. Experimental (E5) and numerical simulation (N5) results ............................. 77

Figure 40. Temperature matches for each thermocouple position for E5 ........................ 78

Figure 41. Experimental (E3) and numerical simulation (N3) results ............................80

Figure 42. E1 combustion tube cross-sectional CT images, every 9 mm interval .........100

Figure 43. E2 combustion tube cross-sectional CT images, every 9 mm interval .........101

Figure 44. E3 combustion tube cross-sectional CT images, every 9 mm interval .........102

Figure 45. E4 combustion tube cross-sectional CT images, every 9 mm interval .........103

Figure 46. E5 combustion tube cross-sectional CT images, every 9 mm interval .........104

Figure 47. E6 combustion tube cross-sectional CT images, every 9 mm interval .........105

Figure 48. E7 combustion tube cross-sectional CT images, every 9 mm interval .........106

# LIST OF TABLES

Page

Table 1. Screening criteria for ISC and steam injection (adapted from (Taber et al. 1997)) ....3

Table 2. SARA composition of Liaohe heavy oil before and after aquathermolysis (adapted from (Hongfu et al. 2002)) ....11

Table 3. Changes in physical properties of oil samples in presence and absence of water (adapted from (Lee et al. 1989)) ....13

Table 4. Thermocouple positioning ....16

Table 5. Peace River reservoir and bitumen properties (adapted from (Hamm et al. 1995, Svrcek et al. 1989)) ....19

Table 6. Sample preparation data ....20

Table 7. List of equipment ....21

Table 8. CT scan parameters ....22

Table 9. Oil upgrading summary ....45

Table 10. Postmortem analysis summary ....53

Table 11. Mass balance summary ....57

Table 12. Grid properties ....68

Table 13. Rock and fluid properties ....70

Table 14. Relative permeability curves endpoints temperature dependency ....72

Table 15. Properties of components ....73

Table 16. Viscosity correlation coefficients used in the simulation study ....74

Table 17. Kinetic parameters of reactions ....76

Table 18. Activation energy values for the cracking reaction..........................................76

# CHAPTER I

# INTRODUCTION AND LITERATURE REVIEW

According to the 2011 International Energy Outlook (Conti et al. 2011), the demand for liquid fuel will increase 28% by 2035 - from 83.3 million barrels per day in 2011 to 106.4 million barrels per day in 2035 (Figure 1).

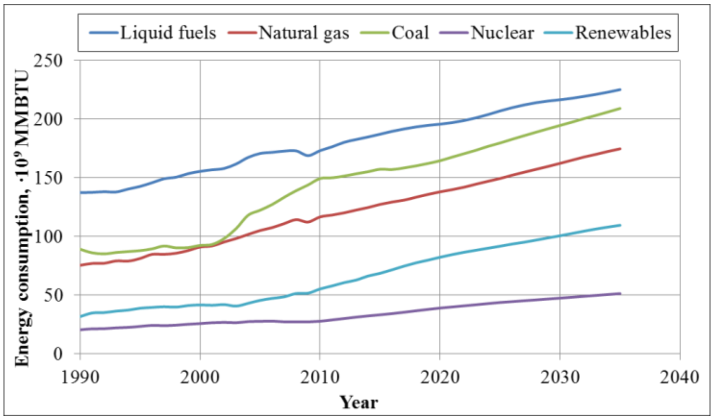

**Figure 1.** World energy consumption by fuel types, 1990-2035 (Conti et al. 2011)

While demand for liquid fuels increases, conventional oil reserves continue to deplete. Unconventional resources such as deep water formations, shale oil and gas reservoirs, tight gas strata, and in particular, oil sands, are becoming more important. At the end of 2010, reliable estimations placed worldwide reserves at 1.28 trillion barrels of oil (Attanasi et al. 2010). This amount represents just conventional oil reserves and does not include the amount of heavy oil, extra-heavy oil, and bitumen in place. Natural bitumen is reported in 598 deposits in 23 countries and the total amount in place is estimated at 3.38 trillion barrels (Attanasi et al. 2010), which is 2.6 times more than conventional oil reserves.

As defined by the U.S. Geological Survey (Meyer et al. 2007), heavy oil is chemically characterized by its asphaltene content, which is categorized by its density and viscosity. The upper limit for heavy oils has been set at 22 °API gravity and a viscosity of less than 100 cp. Extra-heavy oil has gravity of less than 10 °API and a viscosity between 100 cp and 10,000 cp. Natural bitumen has gravity of less than 10 °API and a viscosity greater than 10,000 cp (Attanasi et al. 2010).

Due to the high viscosity of bitumen, thermal enhanced oil recovery (EOR) methods are the most suitable for extraction (Figure 2).

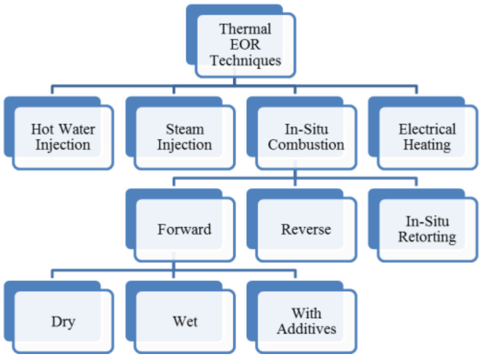

**Figure 2.** Thermal EOR techniques classification (adapted from (Farouq Ali et al. 1994))

Among thermal EOR techniques, hot water injection (HWI) and steam injection are the most common methods (Spreight 2009).

In steam injection process, steam is injected continuously through injection wells and oil is produced from the production wells (Butler 1991). During HWI, hot water is introduced into the reservoir instead of steam. HWI is less effective than steam injection because of the lower heat content of hot water and early breakthrough of hot water due to its higher mobility then oil. The main limitations for steam injection and HWI are reservoir thickness and reservoir depth. For deep reservoirs, heat losses that occur along the injection well may result in low steam quality or in low injection water temperature (Liang et al. 2013) (Table 1).

However, in-situ combustion (ISC) does not have the same limitations as either steam injection or HWI (Table 1). The main advantage of ISC is that heat is not transferred from the surface but generated inside the reservoir. Another undisputed advantage is the upgrade of oil in the ISC process because the least desired for production heavy fraction of oil is consumed for fuel formation and less dense and viscous oil is produced (Martin et al. 1958, Xu et al. 2000, Xia et al. 2001).

**Table 1.** Screening criteria for ISC and steam injection (adapted from (Taber et al. 1997))

| **Parameter, unit** | **Net pay thickness, m** | **Permeability, md** | **Reservoir depth, m** |
|---|---|---|---|
| **ISC** | > 3 | > 50 | > 3,505 |
| **Steam injection** | > 6.1 | > 200 | > 1,371.6 |

ISC is a process of oil ignition in the porous media of rock (Prats 1982) that involves air or oxygen-enriched gas injection into a preheated near-wellbore zone. This causes an intense exothermic reaction. A small amount of initial oil is consumed for heat generation. The continuous heat generation by burning the available fuel maintains the stable combustion front (Mahasneh 2012). Released heat increases oil mobility and causes inflow to production wells (Figure 3). In ISC, a heat wave moves along the reservoir faster than it could have moved with the combined processes of conduction through saturated rock media and convection with gas flow (Martin et al. 1958).

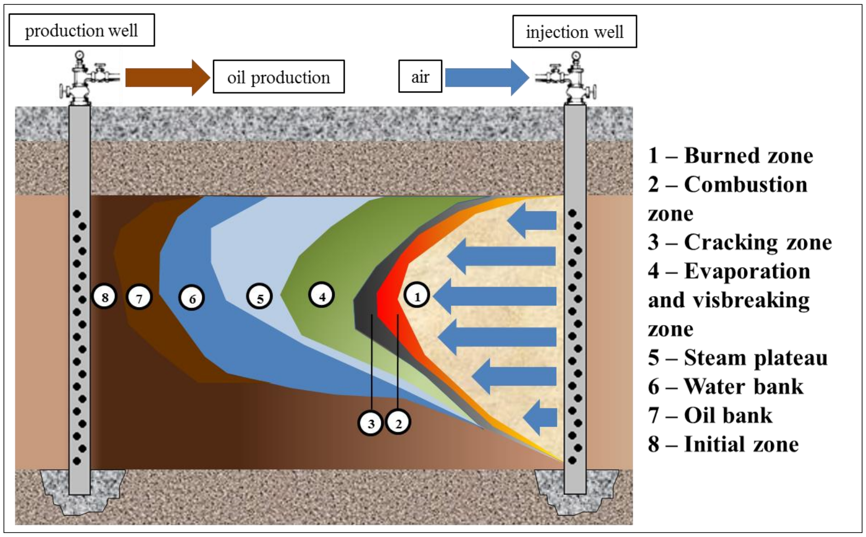

**Figure 3.** ISC scheme (adapted from (DOE 2013))

In dry forward combustion, the established front initiated near the injection well propagates toward production wells by combined gas, steam, and water drive, forming several zones with contrasting properties and residual oil saturation (Sarathi 1999).

Considered one of the oldest EOR techniques, the patent for ISC was obtained by Frank Howabd in 1923 (Howabd 1923). ISC has shown great potential by demonstrating a recovery factor up to 60% during field-scale applications. For example, 56.7% of oil recovery was achieved in South Belridge (Shen 2002), and 50% of oil recovery in the Balol Field Phase-1 Pilot (Dayal et al. 2010). Around 3,500 bbl/day production increase was reported after air injection started in the Santal field (Chattopadhyay et al. 2004).

However, the use of ISC has not achieved wide popularity. In 2002, 1.3 million bbl/day were produced by means of thermal EOR methods, and only 2.2% of this amount was the contribution of ISC (Moritis 2002). The most important reason for such narrow application of ISC is probably that the process is complex and not well understood.

The effects of reservoir heterogeneities on ISC have been previously investigated. Fuel availability is the major factor determining ISC project success (Mahasneh 2012). It increases with increasing initial oil saturation (Alexander et al. 1962). Another significant factor is oil API gravity. Fuel availability decreases as the API gravity of the crude oil increases (Alexander et al. 1962). Oil viscosity at reservoir conditions also influences fuel availability. Fuel availability increases with increasing oil viscosity (Alexander et al. 1962) and the chemical composition of oil has a significant influence on ISC (Bae 1977). However, it is not just oil characteristics that influence ISC performance; increasing reservoir pressure also results in increasing the combustion front temperature and decreasing the combustion front velocity (Wilson et al. 1963). Reservoir mineralogy also has an important impact on ISC performance because rock surface area determines chemical reaction kinetics (Drici et al. 1985). The presence of clay was reported to decrease the activation energy of combustion reactions (Bousaid et al. 1968) and increase the amount of coke deposition and generated heat (Vossoughi et al. 1982). Metallic salt additives act as catalysts (Castanier et al. 1992, Gerritsen et al. 2004), and decrease the activation energy of combustion reactions (Bagci et al. 2004).

Because the ISC process remains not fully understood and is affected by a large number of factors (Gutierrez et al. 2009), it could not be simulated in a field performance. The only way to estimate the performance of the technique is through an expensive pilot test.

Early attempts to simulate ISC date back to the late 1950s. Ramey was the first to model ISC in 1959 (Ramey 1959). His work was followed by the work of Bailey and Larkin, also in 1959. Ramey, Bailey, and Larkin considered conduction to be the only mode of heat transfer in the ISC (Bailey et al. 1959). In 1960, Bailey and Larkin, disregarding heat losses, introduced convection as a heat transfer mode (Bailey et al. 1960). Chu improved the model in 1963 by including conductive heat losses to the surrounding formations (Chu 1963). His next step was the inclusion of the condensation-vaporization effect in 1964 (Chu 1964). In 1971, Smith and Farouq Ali presented a mathematical model of ISC for a two-dimensional reservoir. In their model, single-phase fluid moved in two directions, and conduction-convection heat transfer spread in a third direction (Smith et al. 1971). The approach to ISC simulation radically changed in 1979, when chemical reactions as a heat source were first introduced (Crookston et al. 1979). The proposed reaction scheme consisted of four reactions, including cracking of heavy oil into light oil, coke, and inert gas; burning of heavy oil; burning of light oil; and burning of coke. These chemical reactions are used in commercial simulators (2009).

Another widely applied kinetic model was proposed by Belgrave, Moore, Ursenbach, and Bennion in 1993 (Belgrave et al. 1993). The principal difference of this model was in the description of coke as an asphaltene derivative. The proposed model described the transformation of maltene fraction into asphaltenes and then asphaltene oxidation to coke. The coke burning reaction was defined as in the model by Benham and Poettman (Benham et al. 1958). In the model proposed by Dechelette et al. in 2006, coke burning reactions were considered to be the main source of heat (Dechelette et al. 2006). Dechelette's model included three reactions and two types of coke. The first type of coke was formed during oil oxidation reaction while the second type of coke was a residue product of the first type of coke burning. The third reaction in the proposed model was the formation of water and carbon oxides from type two coke burning. The next stage of ISC simulation development was the introduction of compositional models, that described oil in terms of saturate, aromatic, resin, and asphaltene (SARA) fractions. In these models, the transformation of SARA fractions under oxidation conditions was described (Freitag et al. 2006, Jain et al. 2010).

Despite all the advances in the modeling of oil component transformations, a model to predict the oxidation behavior of various oils was not achieved (Gutierrez et al. 2012). This remains one of the most complicated issues along with the development of new approaches to reservoir gridding. Combustion front thickness is estimated to be several centimeters long (Bagci 1998). While grid block dimensions in field-scale simulation studies account for hundreds and thousands of meters (de Zwart et al. 2008). Large grid block volumes require sufficient energy to maintain temperature-dependent reactions

(Gutierrez et al. 2009). This causes problems associated with combustion front quenching due to low temperatures in grid blocks (Tingas et al. 1996). Gridding problems can be solved by dynamic gridding techniques (Druganova et al. 2010, van Batenburg et al. 2011, Christensen et al. 2004) or by constructing field elements out of one-dimensional combustion tubes (Marjerrison et al. 1992).

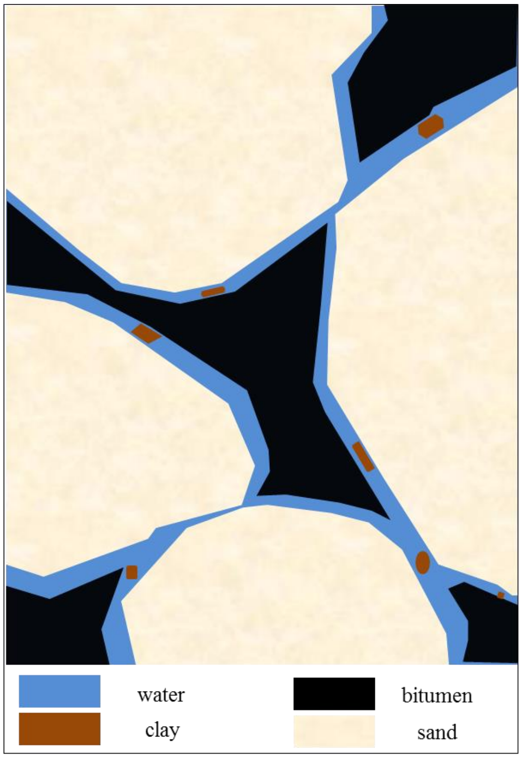

**Figure 4.** Oil-sand micro-structure (Mossop 1982)

ISC field performance can be mimicked with an adequate chemical reaction scheme introduced into the numerical simulator. However, constructed reaction schemes until now have been built on the basis of average reservoir properties, and ISC dynamics change with reservoir heterogenities. The effect of initial water saturation on dry forward combustion has not yet been investigated.

First, initial water saturation changes the wetting characteristics of rock. The hydrophilic nature of the silica sand results in the formation of a thin water film covering the sand grain surface (Figure 4). This water film prevents the bitumen from contact with the sand grain surface, which makes the bitumen extraction process feasible (Takamura et al. 1983).

During the thermal EOR processes, formation water is heated and vaporized, creating an additional drive mechanism , which is described as an “internal-steam drive” or an “in-situ steam drive” (Dehghani et al. 1997). Experimental results have shown that the contribution of an in-situ steam drive to cumulative oil recovery accounts for an additional 8-10% (Dehghani et al. 2001). In addition, the mobilization of water and oil phases forms a pressure drop, which leads to the liberation of the gas from the oil, resulting in the creation of a dissolved gas drive (Wang et al. 2006).

However, the formation water creates more than additional drive mechanisms. Under EOR temperature conditions, it also interacts with bitumen in a group of reactions known as aquathermolysis or hydrous pyrolysis. Aquathermolysis results in the decomposition of asphaltic components, thus decreasing the concentration of the least-desired fractions and increasing oil mobility (Brons et al. 1994, Johnson et al. 1987). A comparison study of bitumen pyrolysis in hydrous and anhydrous conditions indicated that the presence of water determines bitumen transformations. In the presence of water, bitumen is cracked to form light oil, while in the absence of water, pyrobitumen, a highly cross-linked aromatic structure with decreased mobility, is formed (Lewan 1991).

Temperature borders for hydrous pyrolysis conditions vary significantly for different oil compositions. The mineral composition of rock also affects the aquathermolysis process (Monin et al. 1988). In hydrous pyrolysis experiments conducted on the Alberta Basin bitumen, cracking was reported to occur within the temperature range of 300 and 360 $^{o}$C (Markano et al. 2010, Markano et al. 2013). Bitumen reactivity was not discovered below 300 $^{o}$C. Chen et al. studied aquathermolysis on bitumen sands of Athabasca, Peace River, Cold Lake, and Wabasca (Chen et al. 1990). The corresponding temperature range for bitumen cracking was reported to be 250-300 $^{o}$C. Bitumen cracking was also reported in the studies related to oil shale. In a study of Kimmeridge shale, bitumen cracking occurred above 320 $^{o}$C (Barth et al. 1989). In the experiments conducted on the Santa Maria Basin shale, bitumen cracking took place above 300 $^{o}$C (Peters et al. 1990). Bitumen cracking was initiated at the same temperature for the Woolford shale (Lewan 1985), while for the Phosphoria Retort shale the low-temperature limit for bitumen cracking corresponded to 340 $^{o}$C (Lewan 1985). Liaohe heavy oil was tested for SARA composition before and after a 24-hour treatment with water under 240 $^{o}$C (Hongfu et al. 2002). These experiments were repeated three times. The composition of heavy oil before and after the treatment is summarized in Table 2. The compositional change of oil after the steam treatment revealed a decrease in resin and asphaltene content by an average of 14% and 24%, correspondingly. The decrease in heavy fraction weight was accompanied by an increase in saturate and aromatic content that corresponded to an average of 27% and 13%, respectively.

**Table 2.** SARA composition of Liaohe heavy oil before and after aquathermolysis (adapted from (Hongfu et al. 2002))

| **Sample** | **1** | | **2** | | **3** | |
|---|---|---|---|---|---|---|
| | **Initial oil** | **Oil after treatment** | **Initial oil** | **Oil after treatment** | **Initial oil** | **Oil after treatment** |
| **Saturate, wt%** | 27.4 | 30.7 | 25.4 | 28.2 | 20.7 | 32.8 |
| **Aromatic, wt%** | 31.4 | 33.5 | 25.9 | 33.2 | 36.6 | 38.5 |
| **Resin, wt%** | 34.4 | 30.6 | 41.9 | 33.8 | 28.3 | 25.2 |
| **Asphaltene, wt%** | 6.8 | 5.2 | 6.8 | 4.8 | 4.4 | 3.5 |

The main source of heat for maintaining a stable ISC process is coke. In various kinetic models, coke is considered as an asphaltene derivative (Belgrave et al. 1993, Freitag et al. 2006, Jain et al. 2010). The influence of steam on ISC for Athabasca bitumen was investigated and found to affect the coke formation process (Dutta et al. 1999, Dutta et al. 2000). Steam stabilizes free radicals produced in the process of C-C and C-S bond depletion. Under coking conditions, water donates hydrogen to the radicals and stabilizes them. Stabilized radicals are not likely to recombine and form coke, so initial water results in less coke yield. In Figure 5, two curves are represented. The red curve represents the amount of coke formed at different times in a closed reactor in the absence of water, while the blue curve represents the amount of coke formed at different times in a closed reactor with initial water added to bitumen.

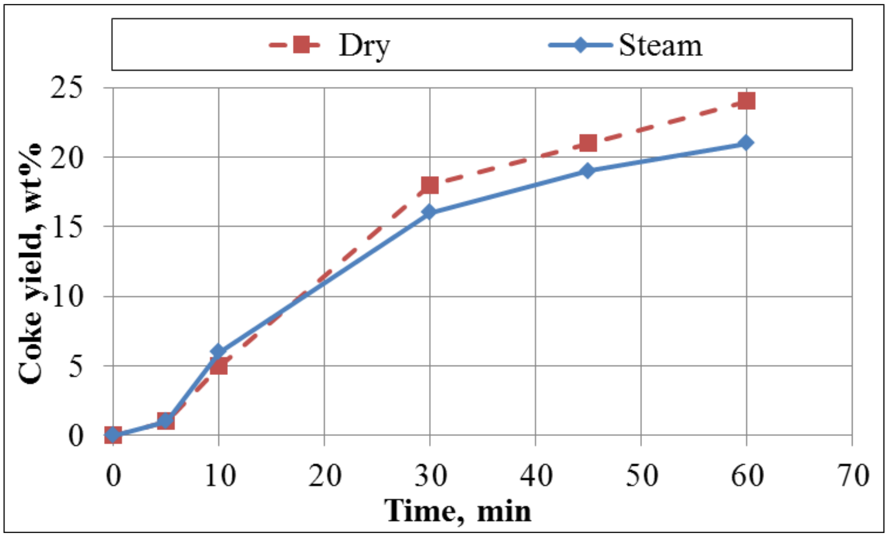

**Figure 5.** The effect of steam on coke yield from bitumen coking at 450 $^{o}$C (adapted from (Dutta et al. 1999))

In other research, a steam atmosphere with metallic catalysts reduced coke generation from the cracking reaction and thus promoted the production of larger amounts of light oil (Fumoto et al. 2010). Steam itself with no addition of catalysts also reduced the coke yield.

Lee and Noureldin investigated the influence of water on the low temperature oxidation (LTO) reactions (Lee et al. 1989). Approximately 3.7 times more $CO_2$ was received while heating heavy oil in the presence of water. They concluded that carboxylic acid was the main $CO_2$ source. Water served as a proton acceptor and the following reaction took place:

$$RCOOH + H_2O \leftrightarrows RCOO^- + H_3O$$

$$RCOO^- \rightarrow R^- + CO_2$$

$$R^- + H_3O \rightarrow RH + H_2O$$

At the same time, oxidation of sulfides took place during LTO to create this reaction:

$$RSR + O_2 \rightarrow RSO_2R$$

$$RSO_2R \rightarrow RR + SO_2$$

Both carboxylic acid and sulfides were found to decrease the quality of upgraded oil and increase its acidity and viscosity. The presence of water increases the quality of LTO products (Table 3).

**Table 3.** Changes in physical properties of oil samples in presence and absence of water (adapted from (Lee et al. 1989))

| **Parameter, unit** | **Original oil** | **LTO @ 200 $^{o}$C** | |
|---|---|---|---|
| | | **Absence of water** | **Presence of water** |
| **H/C** | 1.58 | 1.51 | 1.47 |
| **Acid number, mg of KOH/g** | 1.35 | 2.5 | 1.37 |
| **Viscosity, cp (@40 $^{o}$C)** | 2,400 | 9,530 | 2,950 |

Research performed by Urban and Udell showed that the presence of steam during LTO reduced oxygen consumption and as a result, consumption of oxygen in HTO grew (Urban et al. 1990).

As an EOR method, ISC is complex and has not yet been studied enough. To increase the predictability of this promising technique, this study was conducted to investigate the influence of the initial water saturation on dry forward combustion.

# CHAPTER II

# EXPERIMENTAL PROCEDURE

## II.1. Experimental setup

The setup that was used to perform ISC runs consisted of a combustion tube, thermowells, and the following systems: an electrical heating system, a gas injection system, a liquid production system, a gas production system, and a gas analysis system.

A general overview of the setup is given in Figure 6 and a schematic view is presented in Figure 7.

**Figure 6.** ISC setup

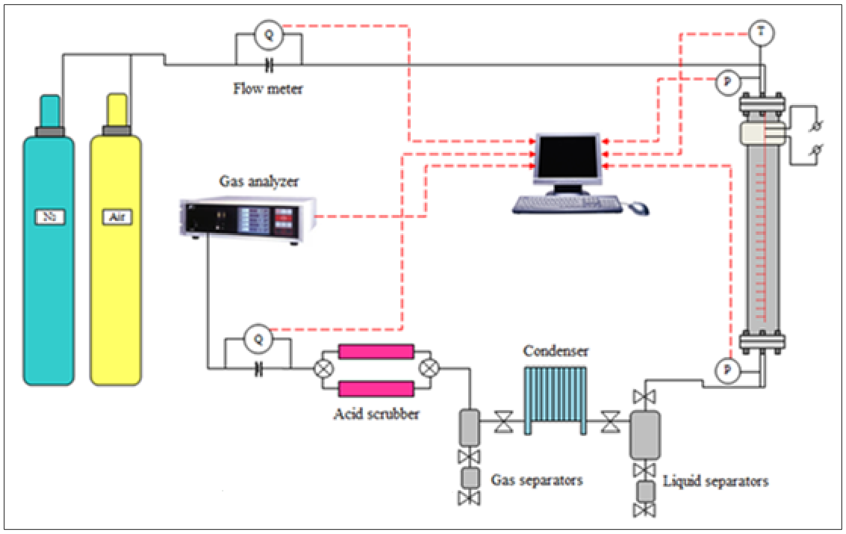

**Figure 7.** ISC setup scheme (adapted from (Mamora et al. 1993))

The combustion tube is a stainless steel pipe with an outer diameter of 3 in. (7.62 cm) and a wall thickness of 1/16 in. (0.16 cm). The tube length is 39-7/8 in. (101.2 cm). Sharp-edged 5 in. (12.7 cm) flanges seal the ends of the combustion tube with copper gaskets. The combustion tube was placed inside the insulation jacket, which is a 46 in. (116.84 cm)-long tube with 6-1/2 in. (16.51 cm) inner and 11 in. (28.16 cm) outer diameters. The 4-1/2 in. (11.43 cm)-thick annulus of the insulation jacket is filled with an insulation material made from calcium silicate. To reduce heat loss, the combustion tube was wrapped with additional insulation materials (cotton and cloth fiberglass) before being installed inside the insulation jacket.

Two thermowells were used for permanent temperature monitoring along the combustion tube. Each thermowell is a 1/8 in. (0.32 cm) welded-end stainless steel tube, equipped with OMEGA® J-type JQMSS-020G thermocouples that are inserted at different positions of the thermowell. Thermocouple positioning for each run is summarized in Table 4.

**Table 4.** Thermocouple positioning

| | # | **E1** | **E2** | **E3** | **E4** | **E5** | **E6** | **E7** |
|---|---|---|---|---|---|---|---|---|
| **Thermocouple position, cm** | 1 | 2.7 | 2.7 | 2.7 | 10.2 | 10.2 | 2.7 | 10.2 |
| | 2 | 9.5 | 14.9 | 9.5 | 14.9 | 14.9 | 9.5 | 14.9 |
| | 3 | 15.6 | 26.0 | 15.6 | 21.0 | 21.0 | 15.6 | 21.0 |
| | 4 | 22.2 | 30.2 | 22.2 | 26.0 | 26.0 | 22.2 | 26.0 |
| | 5 | 30.2 | 33.2 | 30.2 | 30.3 | 30.3 | 30.2 | 30.3 |
| | 6 | 37.0 | 36.8 | 37.0 | 36.8 | 36.8 | 37.0 | 36.8 |
| | 7 | 66.5 | 51.3 | 44.5 | 45.4 | 45.4 | 59.1 | 45.4 |
| | 8 | 73.7 | 59.1 | 51.3 | 51.3 | 51.3 | 66.5 | 51.3 |
| | 9 | 78.6 | 73.7 | 59.1 | 59.7 | 59.7 | 73.7 | 59.7 |
| | 10 | 89.4 | 78.6 | 66.5 | 64.6 | 64.6 | 78.6 | 64.6 |
| | 11 | | | 73.7 | 73.5 | 73.5 | | 75.3 |
| | 12 | | | 78.6 | 96.4 | 84.0 | | 84.0 |
| | 13 | | | | | 96.4 | | 96.4 |

The temperature necessary for the bitumen ignition was reached with electrical heaters, and placed at the top of the combustion tube (Prats 1982). Two band heaters and one cartridge heater were used during the experiments (OMEGA® 400 W band heater model MBH-3015400T/120, OMEGA® 200W band heater model MBH-3015400T/120, and an OMEGA® cartridge heater model CIR-2066/120V-905-600 W). Due to the extremely high temperature values (i.e. ~700 $^{o}$C) that were achieved at the top of the combustion tube, the cartridge heaters quickly broke and could not be used for the other experiments. Therefore, cartridge heaters were not used for all experiments.

The gas injection system consisted of the air and nitrogen cylinders connected to the injection end of the combustion tube and an OMEGA® PX621 pressure transducer that was connected in series with an analog manometer.

The liquid production system consisted of two separator assemblies. A condenser connected the liquid separator assembly to the gas separator assembly. The condenser consisted of a 1/4 in. (0.64 cm) stainless steel spiral pipe installed inside a plastic pipe of a larger diameter. During the experiments, cold water circulated in the annular space of the condenser, to cool the produced gases on the way from the liquid separators to the gas separators. The gas separator assembly consisted of two separators that were used for the elimination of condensed water and light hydrocarbons from the gas flow.

The produced gases traveled through production lines and arrived at acid scrubbers first to capture $H_2S$ and water vapor and then reached a 2 μ dust particle filter and gas filters, which were installed prior to the gas analyzer.

The produced gas composition was measured with a FUJI® infrared gas analyzer type ZRE NDIR/$O_2$ in terms of $O_2$, $CO_2$, CO, and $CH_4$. The gas flow to the gas analyzer was set to 0.5 l/min. It was kept constant by the means of a valve installed before the inlet of the gas analyzer.

### II.2. Sample characterization

The experimental studies were conducted with a Canadian bitumen taken from the Peace River region. The Peace River is one of the four largest oil sand deposits located northwest of Canada in the Alberta province (Figure 8). The reservoir covers an area of approximately 6,200 square kilometers and contains 12 billion cubic meters of bitumen in place (Hamm et al. 1995). Peace River bitumen viscosity at 25 $^{o}$C is 72,600 cp (Svrcek et al. 1989). The reservoir permeability varies between 200 and 1650 md. High permeability values are observed in the Basal Transition Zone. The reservoir properties are summarized in Table 5.

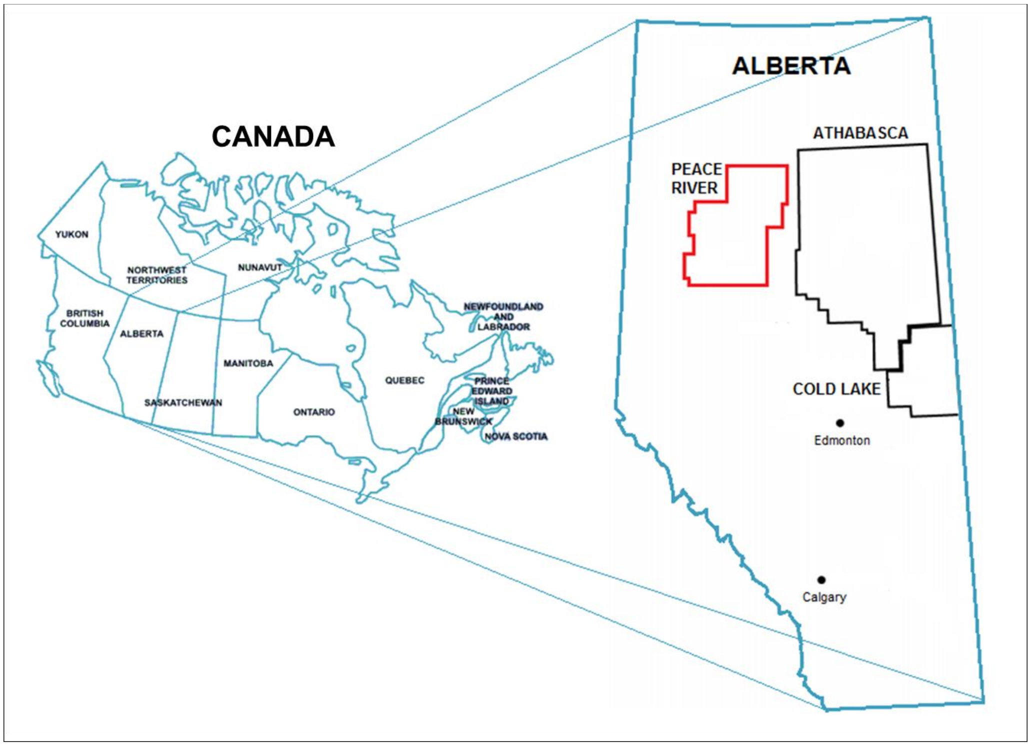

**Figure 8.** Peace River oil sands location (adapted from (Hein 2000))

**Table 5.** Peace River reservoir and bitumen properties (adapted from (Hamm et al. 1995, Svrcek et al. 1989))

| **Parameter, unit** | **Value** |
|---|---|
| **Oil gravity @ reservoir conditions, $^{o}$API** | 7.5 |
| **Oil viscosity @ 25 $^{o}$C, cp** | 72,600 |
| **Oil molar mass, g/mol** | 527.5 |
| **Reservoir temperature, $^{o}$C** | 16.7 |
| **Reservoir pressure, psi** | 536.6 |
| **Oil bubble point pressure, psi** | 464.1 |
| **Reservoir thickness, m** | 26 |
| **Depth to top of reservoir, m** | 551 |
| **$k_w/k_h$** | 0.3 |
| **Porosity, frac.** | 0.28 |
| **Formation compressibility, psi$^{-1}$** | $4.2*10^{-7}$ |
| **Formation thermal conductivity, kJ/m$^{3}$-$^{o}$C** | 2,345 |
| **Oil saturation in tar rich zone, frac.** | 0.84 |

### II.3. Bitumen dewatering

Water content of the laboratory bitumen sample was measured with the Yamato® RE-71 rotary evaporator. A 660 ml bitumen sample was loaded inside the evaporator flask and was conditioned for 5 hours at 100 $^{o}$C until the amount of evaporated water volume stopped changing. The amount of the evaporated water corresponded to 40 ml, which is equal to 6 volume percent water in bitumen. Combustion tube tests were conducted without the original bitumen dewatering.

### II.4. Experimental procedure

Experimental samples were prepared one night before the combustion tube run. To meet reservoir rock mineralogy, the samples were prepared with 89 weight percent of

20-40 mesh silica sand and 11 weight percent of kaolinite clay (Bayliss et al. 1976). Porosity of the unconsolidated sand-clay mixture was equal to 32% and amounts of initial water and oil varied. Initial conditions for each experiment are summarized in Table 6.

**Table 6.** Sample preparation data

| **Parameter, unit** | **E1** | **E2** | **E3** | **E4** | **E5** | **E6** | **E7** |
|---|---|---|---|---|---|---|---|
| **Sand, g** | 6,194 | 6,219 | 6,431 | 6,502 | 6,508 | 5,857 | 6,768 |
| **Clay, g** | 796 | 799 | 827 | 836 | 837 | 753 | 870 |
| **Ø, %** | 32 | 32 | 32 | 32 | 32 | 32 | 32 |
| **Oil, ml** | 456 | 458 | 711 | 733 | 719 | 423 | 744 |
| **Water, ml** | 0 | 462 | 0 | 242 | 483 | 0 | 500 |
| **$S_o$, %** | 33.64 | 33.77 | 52.43 | 54.12 | 53.02 | 31.23 | 54.86 |
| **$S_w$, %** | 0 | 34.05 | 0 | 17.85 | 35.63 | 0 | 36.87 |
| **$S_g$, %** | 66.36 | 32.17 | 47.57 | 28.04 | 11.35 | 68.77 | 8.27 |

The prepared mixture was packed inside the combustion tube, and both ends of the combustion tube were sealed properly with the flanges and copper gaskets. The thermowells were inserted from the top of the combustion tube. The leak test was achieved under nitrogen injection at 100 psig.

The combustion tube was wrapped with the additional insulation material and placed into the insulation jacket. The top of the jacket was insulated with fiberglass cotton to reduce heat loss. The external band heaters were connected to electricity through the voltage controller.

The external band heaters were turned on and the nitrogen injection was started at an average 0.5 l/min flow rate. The cold water circulation was started in the condenser unit. After a temperature of around 450 $^{o}$C was reached, the nitrogen injection was switched to 3.4 l/min air injection and the heaters were turned off. The air injection rate was kept constant during the experiments.

The temperature was recorded with NI LabVIEW 2012 software and the gas composition was recorded through TracerDAQ software. A list of equipment used is summarized in Table 7. The experiment was terminated when the temperature peak was reached on the last thermocouple. The termination procedure included shutting down the air injection and starting the nitrogen injection at an approximate rate of 7 l/min to sweep the combustion gases from the system for safety reasons. When the experiment was terminated, the combustion tube was removed from the insulation jacket and left for cooling.

**Table 7.** List of equipment

| Equipment type | Brand name | Model |
|---|---|---|
| thermocouple | OMEGA | JQMSS-020G |
| band heater | OMEGA | MBH-3015400T/120 |
| pressure transducer | OMEGA | PX621 |
| mass flow meter | OMEGA | FMA4000 |
| mass flow meter | OMEGA | FMA-770A-V |
| rotameter | Fischer and Porter | 10A1755S |
| gas analyzer | FUJI | ZRE NDIR/$O_2$ |
| rotary evaporator | Yamato | RE-71 |
| computed tomography | SIEMENS | SOMATOM AS-40 Slice |

The cooled down combustion tube was scanned with an X-ray computed tomography (CT) scanner. Approximately 300 cross-sectional images were taken along the combustion tube for each experiment. The CT scan was performed on the SIEMENS® Somatom Definition AS 40 Slice. The CT scan parameters are summarized in Table 8. The CT images were processed with ImageJ.

**Table 8.** CT scan parameters

| **Parameter, unit** | **Value** |
|---|---|
| **Tube current, mA** | 120 |
| **Tube voltage, kV** | 140 |
| **Rotation time, s** | 1 |
| **Slice thickness, mm** | 3 |

As the last step, visual inspection of postmortem samples was achieved by taking pictures of the unpacked burned sand.

The mass of the produced samples during the experiments, total injected air mass, and the total mass of postmortem were used for mass balance calculations.

# CHAPTER III

# EXPERIMENTAL RESULTS AND DISCUSSION

To estimate the effect of initial water saturation on a dry forward ISC, seven experimental runs were conducted on the Peace River bitumen.

Runs E1 and E2 were performed to check the impact of water existence on ISC. In these two runs, initial bitumen saturation was kept constant at around 33% and initial water saturation was varied, corresponding to 0% in E1, and to 34.05% in E2.

Runs E3, E4, and E5 were performed to determine how the amount of initial water saturation affects the ISC performance. Approximately 53% of initial bitumen saturation was used for these experiments. Initial water saturation varied from 0% in E3, to 17.85% in E4, and to 35.63% in E5.

Reproducibility of the experimental data was achieved with E6 and E7. These runs were performed under the same initial and experimental conditions as E1 and E5, respectively.

ISC success is determined with the stable sustainable combustion front temperature on the basis of oxygen consumption and carbon dioxide production, and oil recovery factor (Alexander et al. 1962, Alamatsaz et al. 2011).

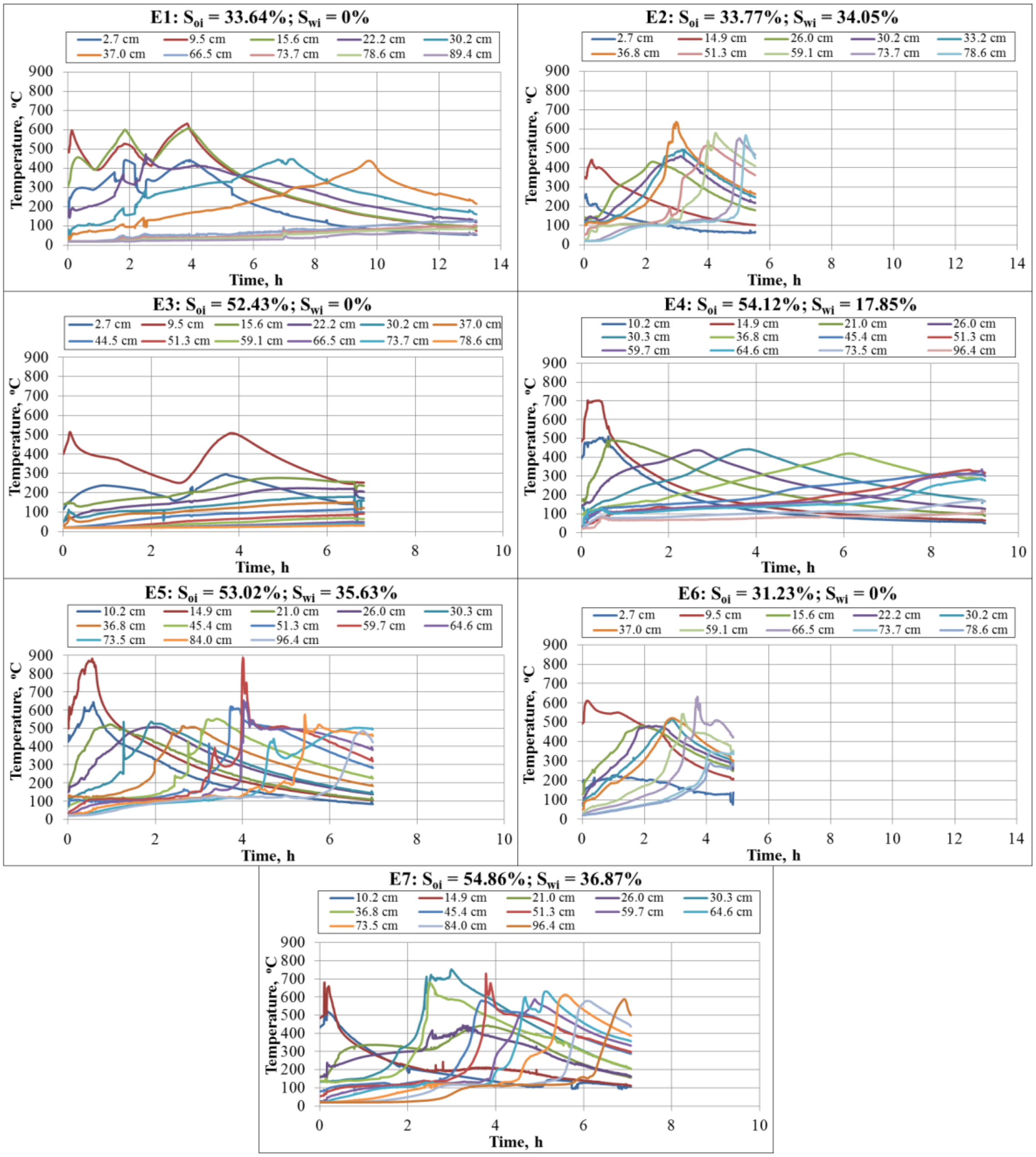

**Figure 9.** Temperature profiles in time for all experiments

In Figure 9, temperature versus time graphs are represented. Each curve on each graph represents a fixed thermocouple position below from an air injection point of the combustion tube.

In E2, the lowest temperature was achieved on the first thermocouple installed in position 14.9 cm. In all the runs, except for E2 and E3, air injection was started when the thermocouple closest to the heater indicated 450 $^{o}$C, but for E2, the cartridge heater broke at 350 $^{o}$C. To save the combustion run, air injection was started. A sustained combustion front was achieved after 3 hours, which proves that the Peace River bitumen is a good candidate for ISC application.

In E1, three temperature peaks registered at 9.5 cm below the air injection point, which was the result of external heating. The first attempt to start air injection failed due to unstable gas outflow, and so the decision was made to pump the system with nitrogen at a high rate, which led to cooling the ignition zone. After flushing the tube with nitrogen, air injection was restored and the problem with unstable outflow was eliminated. To maintain ISC, the decision was made to turn on the heaters again and raise the temperature in the ignition zone under air injection. When the temperature rose above 530 $^{o}$C, the external heaters were turned off. Ignition occurred only after 2.5 hours. A sustained combustion front was also achieved in E1.

In E3, two peaks were registered by at 9.5 cm below the injection point, which was the result of external heating. In E3, ignition did not occur when air injection was started. To support ISC, external heaters were turned on again and ignition finally occurred at around 1.8 hours after air injection started; however, the combustion front still did not sustain in that run.

The following can be said: while comparing runs E1 and E3, initial water saturation was equal and corresponded to 0%, but initial bitumen saturation was significantly greater in E3 (52.43% in E3 vs. 33.64% in E1). ISC performance decrease can be observed for E3. This behavior falls into the ISC frontal advance model (Prats 1982). According to this model, high initial oil saturation results in the surface of the oil bank moving faster than the temperature front. And some conditions, i.e. viscosity of crude oil and initial oil saturation may result in the speed at which the oil bank increases, shifts the temperature front speed significantly. This will cause oil bank to form insuperable flow resistance. As a result, the heat generated during the combustion reactions will be diffused as heat loss to the nearby rocks and will not be transferred along the reservoir. As a result, ISC will collapse.

In terms of sustainability, E5 showed the best performance among all the experiments. Temperature peaks were registered along the entire length of the combustion tube. The combustion front initiated and propagated successfully. Within the seven experimental runs in this study, the ultimate temperature of 887 $^{o}$C was obtained in E5. This result characterizes the Peace River bitumen as a highly reactive oil and a good candidate for ISC application.

With 17.85% of the initial water saturation, as in E4, combustion temperatures could be achieved; however, combustion zone stability could not be maintained as in E5. In

E4, peak temperatures were lower and time intervals between temperature peaks were longer.

A plateau region can be mentioned for E5 for positions 51.3, 59.7, and 64.6 cm below the injection point. This indicates that a source of continuous heat generation was located between 51.3 and 64.6 cm. At 84 cm, a leap can be seen and this leap can be interpreted as coke left behind.

Comparing runs E1 and E6, which were performed under equal conditions, similarities on temperature graphs can be seen. In both runs nearly the same temperatures (609 $^{o}$C in E1 and 611 $^{o}$C in E6) were obtained at ignition. Similar propagation characteristics are general for both experiments: the temperature front propagated slowly. E6 was terminated earlier then E1. Similarities can also be observed in ISC behavior in experiments E5 and E7. Thus, a combustion front successfully sustained in both runs.

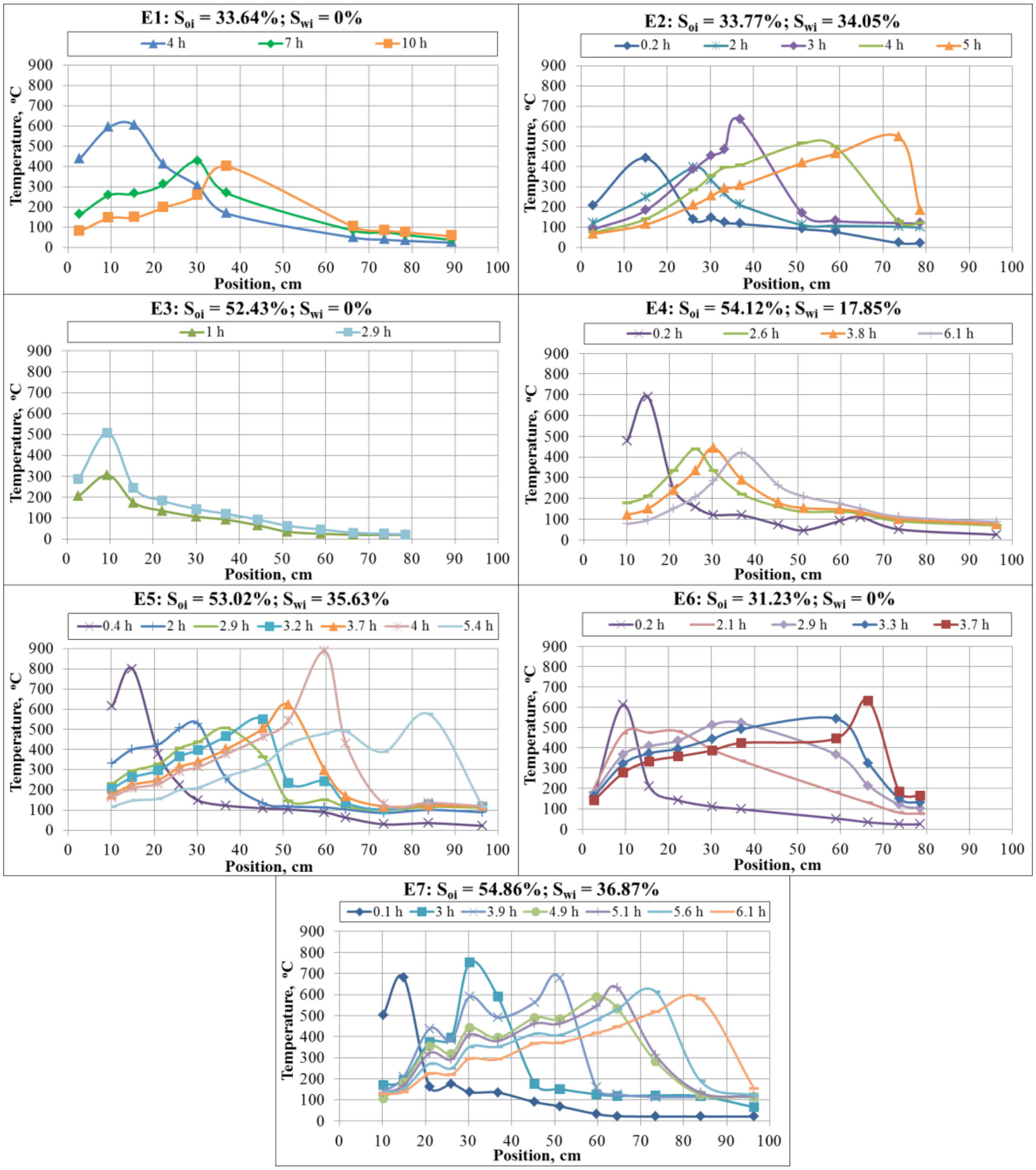

**Figure 10.** Temperature profiles in position for all experiments

Figure 10 represents temperature versus position graphs. These graphs represent temperature profiles along the combustion tube at certain times. A peak on each curve indicates the combustion front position.

Experiments E1, E3, and E6 were conducted with the physically bonded water only. Combustion did not sustain effectively in these runs. However, for E2, E4, E5, and E7, propagation of the combustion front was effective. High temperature regions were observed even at the end of the combustion tube.

Temperature propagation was not good for E1. Temperature peaks were registered at 4, 7, and 10 hours. The decreasing peak temperature trend indicates a quenching combustion. The opposite behavior was observed for E2 - a low temperature was received on the first thermocouple, and after 2.5 hours the combustion front stabilized and showed good propagation characteristics.

The temperature front did not move for E3 and stayed 9.5 cm below the injection point. In comparing E3 and E4, it can be noted that E4 displays better propagation characteristics. In addition, the front temperature tends to decrease. Within experiments E3, E4, and E5, the most stable front was achieved in E5. The front temperature along the tube did not decrease as in E4.

Comparing experiments E1 and E3, the following can be said: increasing bitumen saturation negatively influences front propagation characteristics. In E1, the combustion front moved slowly, while in E3 it stayed in the same position for the whole experiment.

Comparing E1 and E6, better propagation characteristics were observed for E6, but in both of these runs, a decreasing front temperature tendency can be highlighted.

In both E5 and E7 runs, stable combustion fronts were observed.

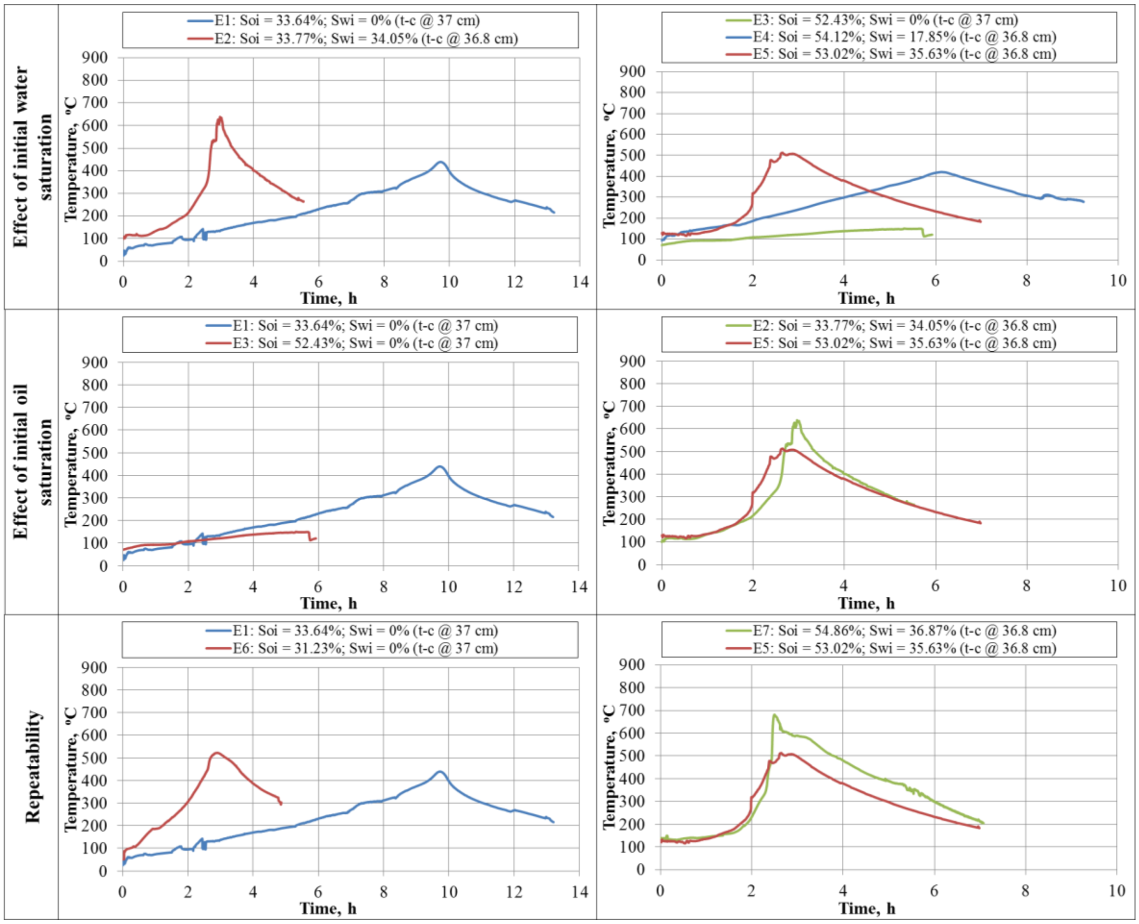

**Figure 11.** Temperature profiles for the 37 cm position below the air injection point

Figure 11 represents temperature peaks registered at the fixed position of 37 cm below the air injection point. E1 was conducted with connate water only, while in E2 34.05% of initial water was added. The addition of water increases the combustion front speed. In E2, the temperature front reached the fixed position much earlier than in E1. The same behavior was also observed for experiments E3, E4, and E5. With increasing initial water saturation, the combustion front velocity increased.

The temperature profile curve slope indicates the heat generation intensity, which is proportional to the chemical reaction rate constant that determines reaction speed. The heating rate can be estimated as the time required for the temperature to increase from 200 to 400 $^{o}$C. Calculated heating rates for each run are summarized in Figure 12.

While comparing experiments E1 and E2, it can be seen that the heating rate is higher for E2. The increasing initial water saturation resulted in the increasing heating rate. The same tendency can also be observed for experiments E3, E4, and E5. In the presence of water, the heating rate also increases with increasing initial oil saturation (E2 and E5), while in the absence of water the opposite tendency can be observed (E1 and E3).

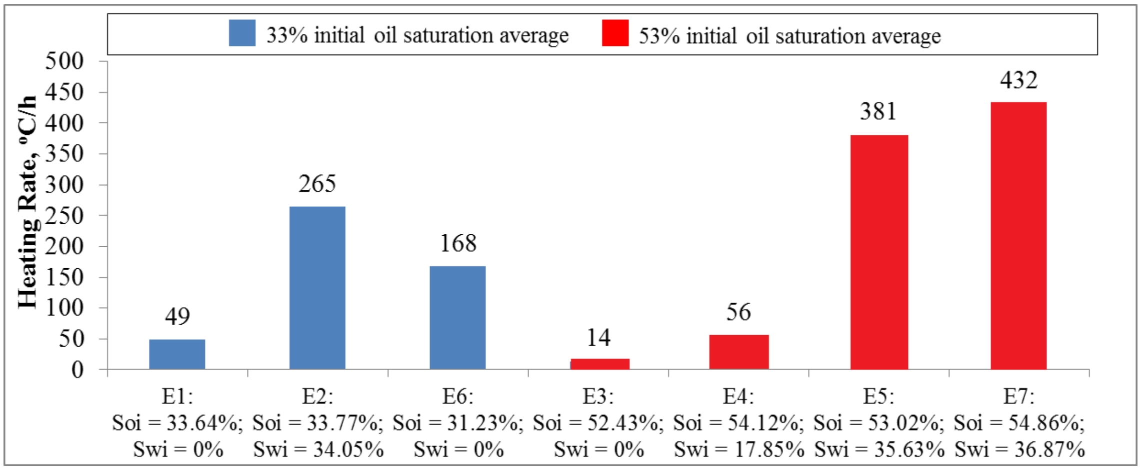

**Figure 12.** Heating rates for the 37 cm position below the air injection point

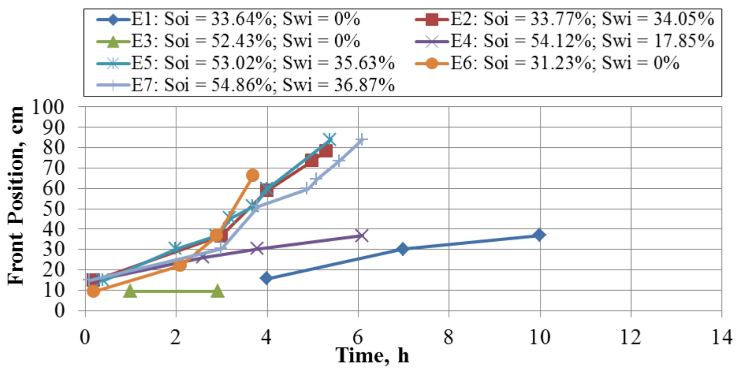

| **Exp.** | **Trend line** | **R²** |
|---|---|---|
| E1 | *y = 3.573 x + 2.56* | 0.9582 |
| E2 | *y = 12.668 x + 8.26* | 0.9572 |
| E3 | *y = 9.5* | - |
| E4 | *y = 3.713 x + 15.21* | 0.9824 |
| E5 | *y = 13.721 x + 3.72* | 0.9551 |
| E6 | *y = 14.966 x + 0.48* | 0.8378 |
| E7 | *y = 11.428 x + 7.38* | 0.9327 |

**Figure 13.** The combustion front position in time

In Figure 13, the combustion front movement for each experiment is given. Each curve on this graph represents an experiment. The combustion front location at a certain time is determined from the highest temperature registered in the combustion tube (Figure 10). To the left of Figure 13 is the trend line equation. The average combustion front velocity can be estimated from the coefficient k in the linear equation. However, combustion front velocity in a stable region is more representative. To estimate the combustion front velocity in a stable region, two temperature peaks close to the end of the combustion tube were chosen (Figure 14). Positions between which combustion front velocities were estimated are listed to the right of the figure.

From E1 to E2, the combustion front velocity increased from 2.5 to 18.3 cm/h with the addition of 34.05% initial water saturation.

The combustion front velocity was estimated to be 0 for E3. In E4, the front velocity corresponded to 2.7 cm/h. The highest combustion front speed of 12.4 cm/h was observed in E5.

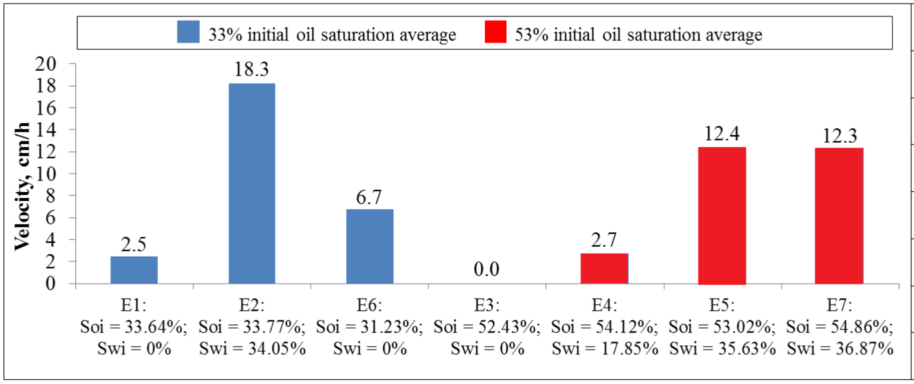

| **Exp.** | **Positions, cm** |
|---|---|
| E1 | 30.2 – 37 |
| E2 | 59.1 –73.7 |
| E3 | – |
| E4 | 30.3 –36.8 |
| E5 | 84 –96.4 |
| E6 | 59.1 –66.5 |
| E7 | 51.3 –73.5 |

**Figure 14.** Combustion front velocities at stable zone

Comparing experiments with the same initial bitumen saturation (E1 and E2; E3, E4, and E5), a general tendency of the front velocity increase with increasing initial water saturation can be observed. The same front velocities were not achieved in E1 and E6 repeatability runs. However, nearly the same velocities were observed for experiments E5 and E7. ISC is a complex process that is highly affected by heterogeneities, for example, heterogeneities of bitumen, or sample packing force.

The effect of initial fluid saturation on ISC performance can be seen in the examples of runs E2 and E5. ISC front velocity decreased with increasing fluid saturation. Because the amount of initial oil saturation was increased from E2 to E5, the load on the combustion front increased as well, resulting in decreasing front velocity (Gutierrez et al. 2009).

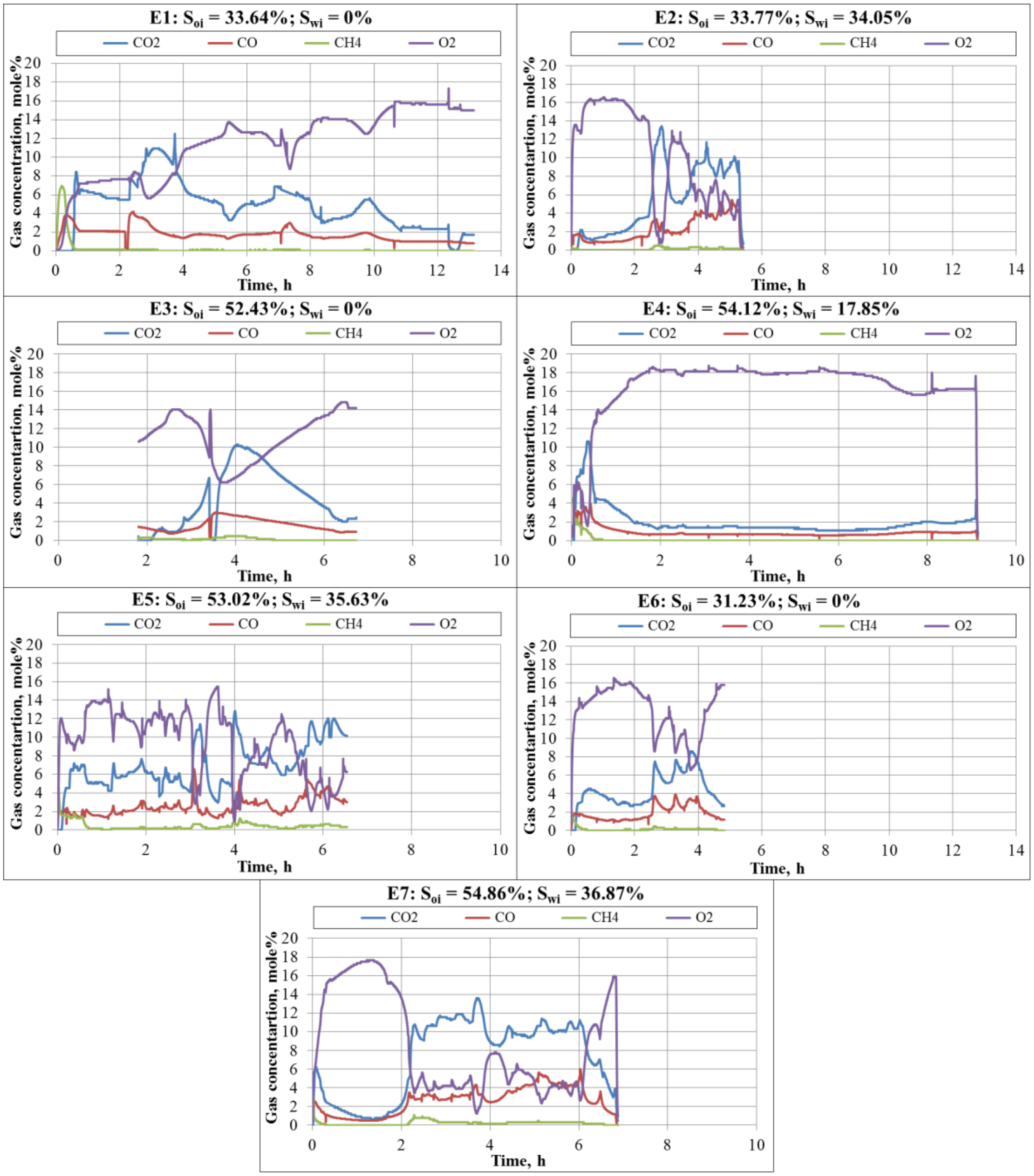

Figure 15 represents gas composition versus time graphs. Each curve represents the mole percentage of $CO_2$, CO, $CH_4$, and $O_2$, in effluent gas flow as a function of time. A variety of gases is formed during ISC. However, ISC success is determined by these four components. A successful experiment is defined by a high $O_2$ consumption over a high $CO_2$ production. ISC starts after an $N_2$ injection; therefore, after air injection starts, $CO_2$ and $O_2$ productions require a stabilization period to demonstrate the real ISC performance. This period is known as the transition period (Hascakir, Glatz, et al. 2011).

In E1, ISC did not stabilize. A rise in the $CO_2$ concentration above 10% is clearly observed at around 2.4 hours, but after 3.9 hours the $CO_2$ concentration stayed below the $O_2$ concentration, which indicates that ISC was fading. Temperature peaks at positions 30.2 and 37 cm were probably received due to LTO reactions (Figure 9).

In E2, it can be noted that stabilization occurred after 2.5 hours. This overlaps with the temperature versus time graph (Figure 9). The time period between 0 and 2.5 hours is defined as the transition period.

As mentioned in E3 (Figure 9), ignition was achieved at the end of 1.8 hours. The time period between 0 and 1.8 hours is not represented in Figure 15 because of an error in the recording software. An increase in the $CO_2$ concentration at around 3.8 hours can be clearly seen in the graph; however, E3 still cannot be declared a successful run for two reasons. The first is that the $CO_2$ concentration stayed mainly below the $O_2$ concentration. The second reason is that the temperature did not sustain. From this point of view, E4 can be considered a controversial evaluation. On the one hand, the combustion front sustained and propagated successfully (Figure 9); on the other hand, $O_2$ was not consumed effectively.

In E5, stabilization occurred at 3 hours, but fluctuations in the $CO_2$ concentration were observed after 4 hours. Similar fluctuations were also observed in E2.

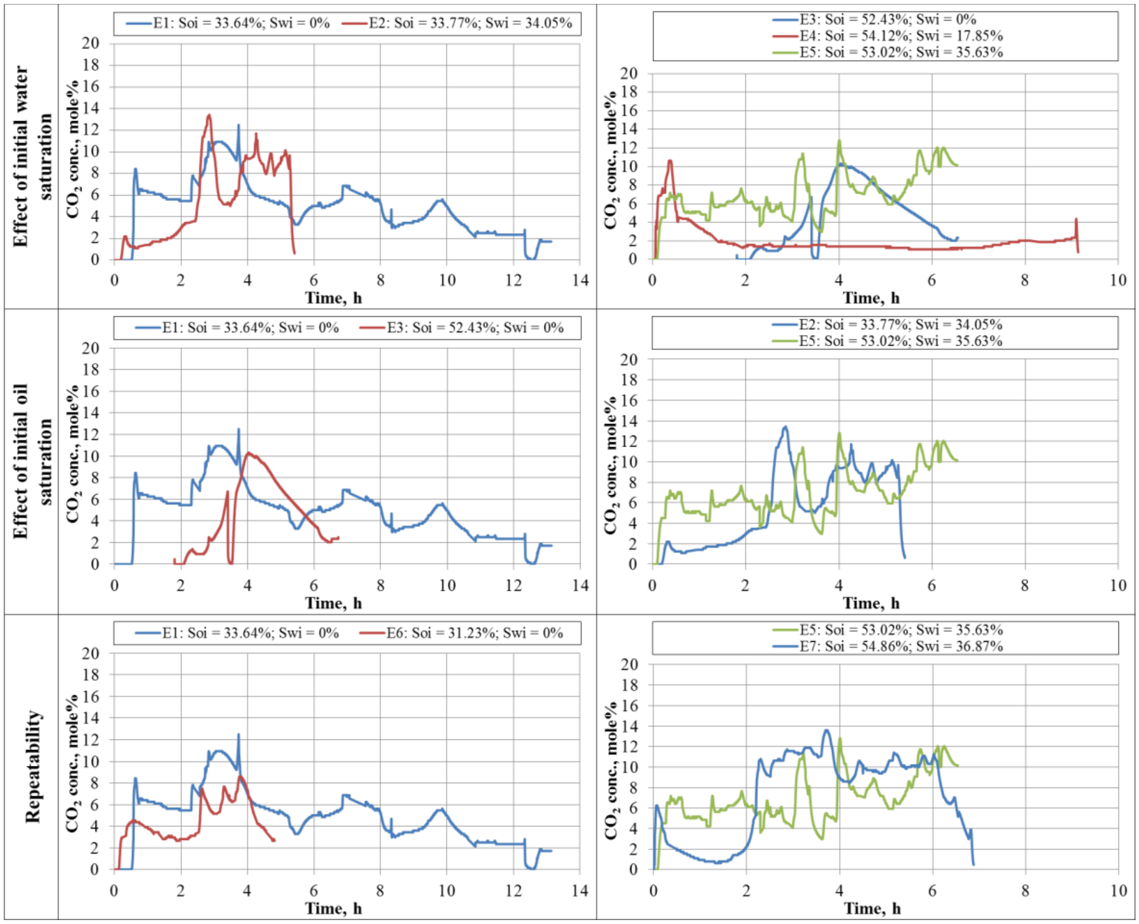

**Figure 16.** $CO_2$ profile comparisons

In Figure 16, $CO_2$ profiles are represented. Each curve on each graph represents the $CO_2$ concentration as a function of time. Runs are combined according to the initial bitumen saturation. Each repeatability run is grouped separately with a pairing run.

Comparing E1 and E2, the following can be pointed out: in E1, the $CO_2$ concentration reached a maximum value at 3.8 hours and continuously decreased, then remained at a low level for the rest of the experiment. Meanwhile in E2, the $CO_2$ concentration stabilized at a high level after 2.3 hours, but significant fluctuations were observed.

In E3, the $CO_2$ concentration did not stabilize. It reached the maximum value of 10% and smoothly decreased, then stayed at 2% by the end of the run.

E5 showed the same behavior as E2; after 3 hours the $CO_2$ concentration stabilized at around 10%. Fluctuations in the $CO_2$ concentration after stabilization were also observed.

The $CO_2$ profile of E4 differed from the $CO_2$ profiles of the other runs, in that the $CO_2$ concentration mainly stayed below 2%. This behavior will be discussed further.

In general, repeatability was reached in E1 and E6. The same $CO_2$ mole fraction values in time were not achieved, but trends for both runs looked similar.

Repeatability was also achieved for E5 and E7. Although a significant $CO_2$ concentration drop can be seen between 0.5 and 2 hours for E7, it can be still said that the $CO_2$ concentration stabilized at around 11%.

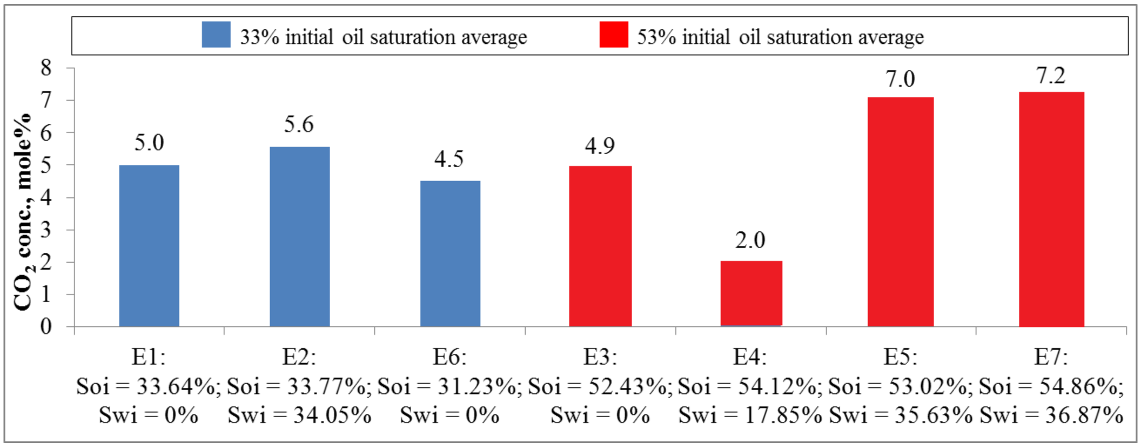

**Figure 17.** Experimental average values for the $CO_2$ concentration in the mole percentage

Average values of the $CO_2$ concentration for all of the experiments are represented in Figure 17. In E1 and E2, with an increase in the initial water saturation, average $CO_2$ concentration during the runs also increased. The same can be said for E3 and E5. As the initial water saturation increased from 0% to 35.63%, the average $CO_2$ concentration increased from 4.9% to 7%. However, in E4, the trend observed for E3 and E5 changes. This behavior will be discussed further. Two sets of repeatability runs (E1 and E6; E5 and E7) demonstrated nearly the same average $CO_2$ values.

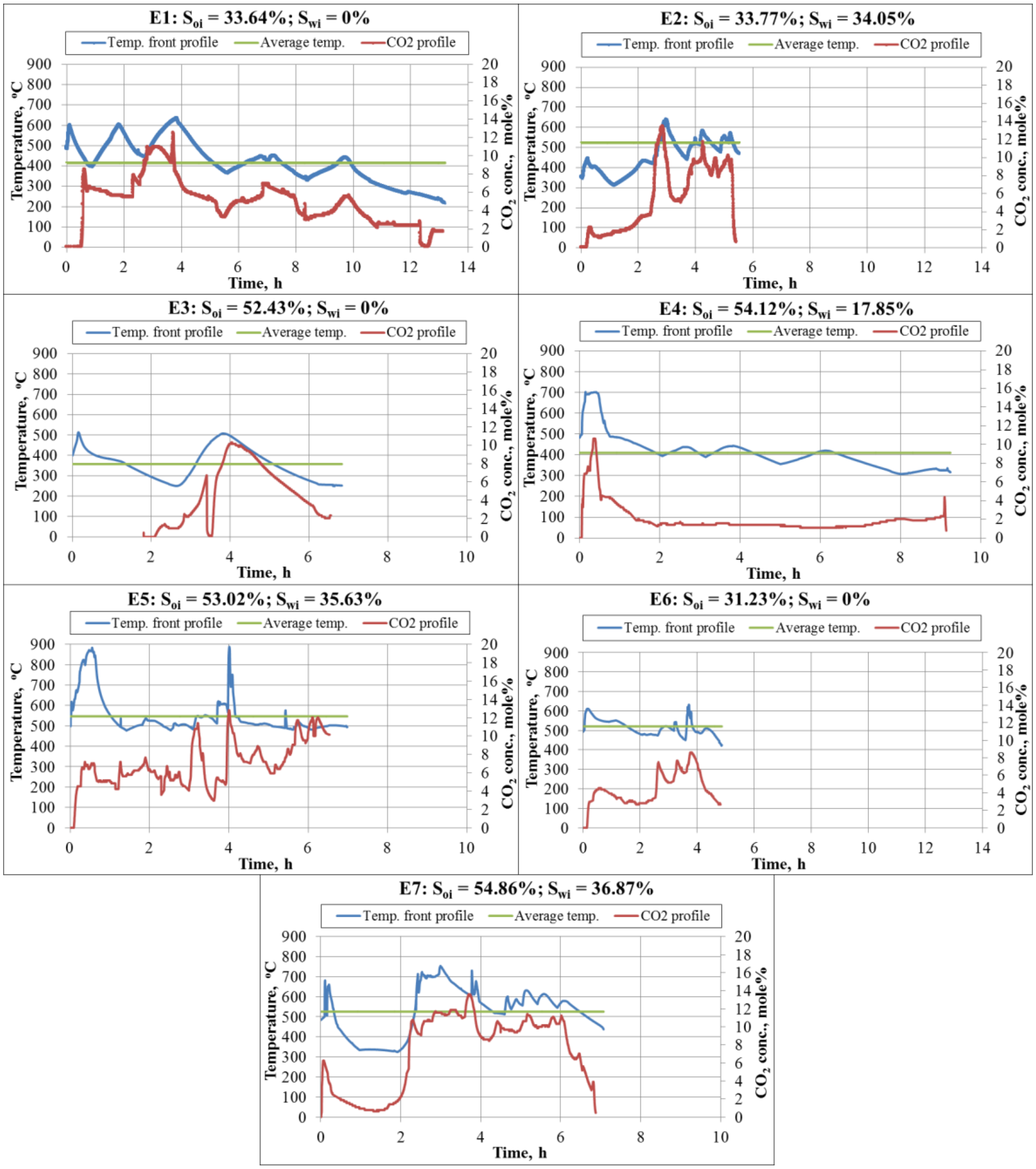
E1: $S_{oi}$ = 33.64%; $S_{wi}$ = 0%

E2: $S_{oi}$ = 33.77%; $S_{wi}$ = 34.05%

E3: $S_{oi}$ = 52.43%; $S_{wi}$ = 0%

E4: $S_{oi}$ = 54.12%; $S_{wi}$ = 17.85%

E5: $S_{oi}$ = 53.02%; $S_{wi}$ = 35.63%

E6: $S_{oi}$ = 31.23%; $S_{wi}$ = 0%

E7: $S_{oi}$ = 54.86%; $S_{wi}$ = 36.87%

**Figure 18.** Temperature front profile vs. $CO_2$ profile

In Figure 18, front temperature values are plotted against $CO_2$ profiles. In E1 and E2, the average front temperature corresponded to 414 and 522 $^oC$, respectively. In addition, maximum temperatures acquired in the combustion tube were 633 $^oC$ for E1 and 638 $^oC$ for E2. From E1 to E2, increased initial water saturation resulted in increased average and maximum temperatures. In E1 and E2, each temperature peak corresponded to an increase in the $CO_2$ concentration.

In E3, E4, and E5, corresponding average front temperature values were 347, 410, and 547 $^oC$; while maximum temperature values were 507, 703, and 887 $^oC$, respectively. The same tendency as for E1 and E2 was observed: as initial water saturation increased from E3 to E5, the average and maximum front temperatures also increased. The average and maximum combustion front temperature values are summarized in Figure 19.

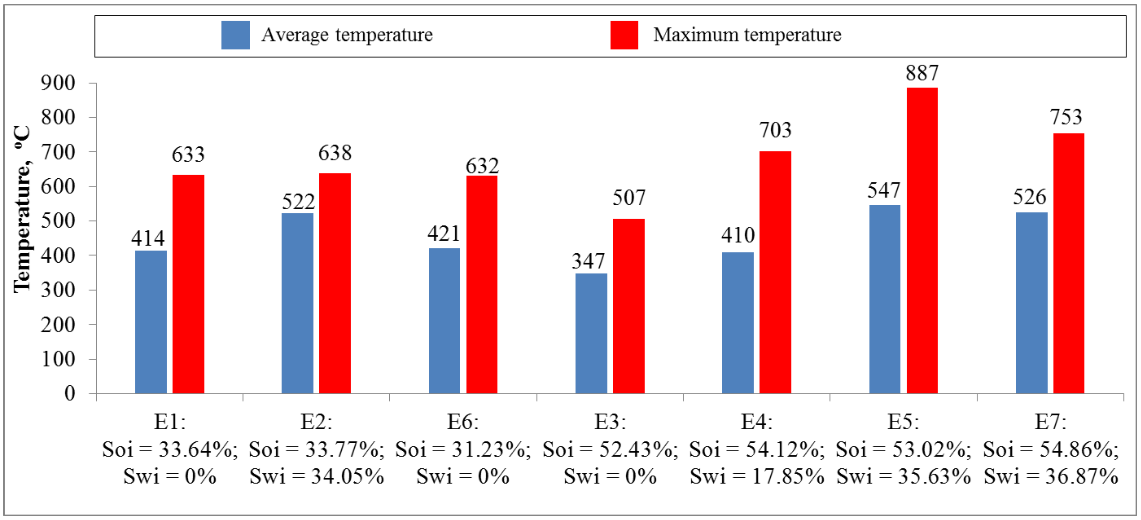

**Figure 19.** Average and maximum combustion front temperatures

In E3, increases in the front temperature overlapped with rises in the $CO_2$ concentration. The same was observed for E4: the temperature peak registered at around 0.4 hours was associated with the corresponding $CO_2$ concentration rise above 11%. In E4, starting from 0.8 hours, the $CO_2$ concentration did not exceed 2%, but the temperature was maintained at an average value of 400 $^{o}$C. LTO reactions dominated in E4. This conclusion can be drawn from a relatively low but stable temperature in the burned zone and low oxygen consumption.

In E5, two regions, corresponding to 0.5 and 4.3 hours, can be highlighted. In this time period, immediate drops in the $CO_2$ concentration followed temperature increases above 600 $^{o}$C. The same behavior occurred for E2 at 2.5 hours.

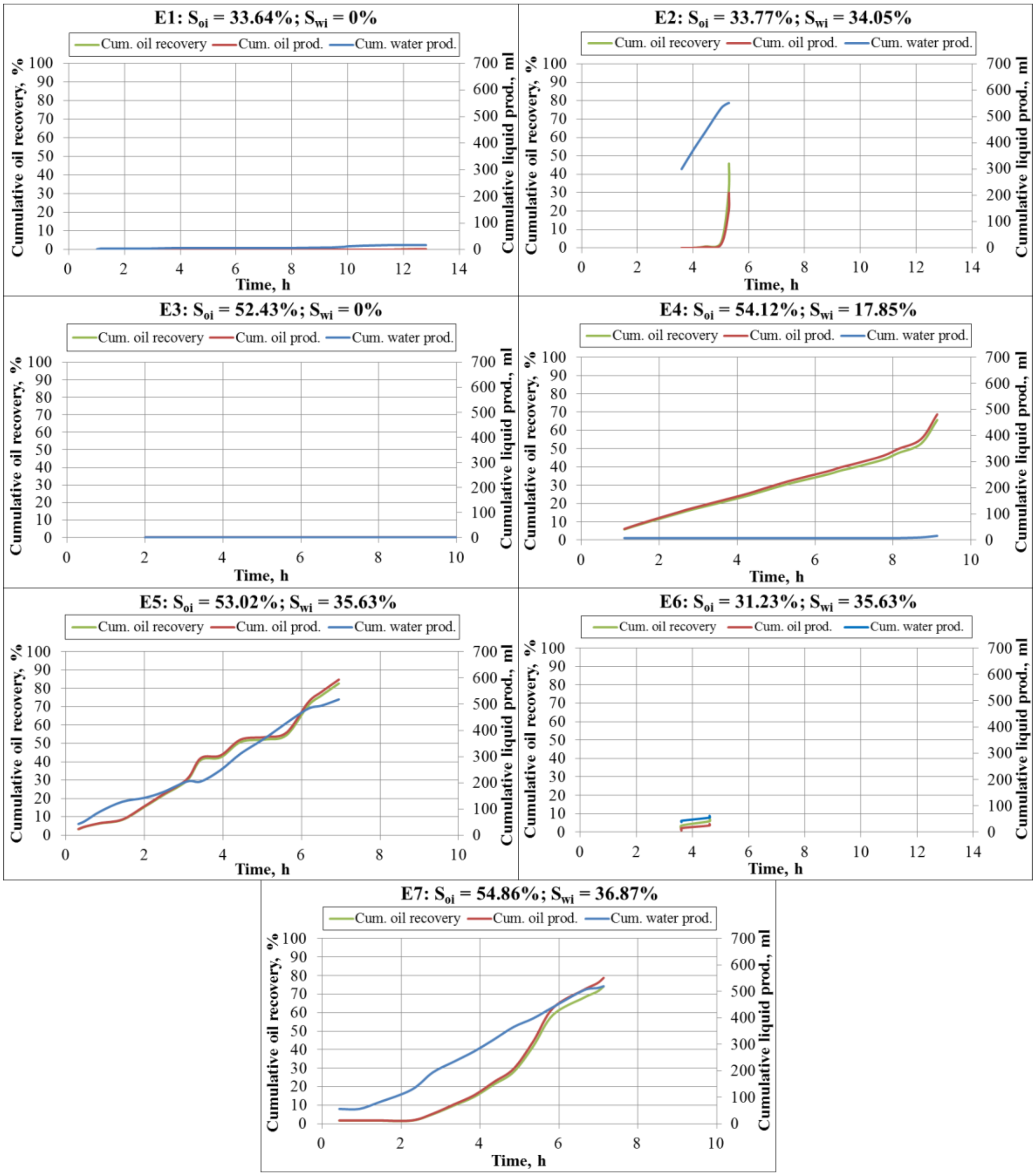

**Figure 20.** Cumulative liquid production and oil recovery

In Figure 20, green curves correspond to the cumulative oil recovery in volumetric percentage and values are given on the left-hand side y-axis. Red and blue curves represent cumulative oil and water production in ml, respectively, and the values are given on the right-hand side y-axis.

In E1, water production was received 1 hour after air injection had been started and oil production was obtained only after 12 hours. With an increasing amount of initial water from E1 to E2, the ISC performance changed. Water production was received 2 hours after the start of air injection. When the oil bank was recovered after 5 hours, oil was received in samples, which is typical behavior for ISC. Several zones are formed during ISC, one of them is a water bank, and the other one is an oil bank. Due to the differences in the condensation temperatures of water and oil, water reaches production wells first. In E2, a 45.8% recovery factor was achieved, while in E1 the recovery factor corresponded only to 0.4%.

Initial water saturation strongly affects ISC performance and determines the success of ISC application. Both E1 and E3 runs were conducted without the addition of water to the sample and both of these runs were unsuccessful in terms of oil recovery.

Comparing recovery graphs for E3, E4, and E5, it can be proved that E3 was unsuccessful, since no oil production was received. A controversial evaluation was given to E4 from the analysis of temperature and gas composition graphs (Figure 10, Figure 15). However, oil production started 1 hour after air injection and 65.6% of oil were recovered. It is worth noting that in E4, a low amount of water was produced. Just 16 ml out of 242 ml of the initially packed water were produced for the whole experiment.

E5 showed the best performance in terms of combustion front stability (Figure 10) and $O_2$ consumption (Figure 15). E5 also demonstrated the best performance in terms of oil production. The recovery factor that was achieved during E5 corresponded to 82.7%, and throughout the entire experiment, oil was produced with water. The same behavior was observed previously by other researchers (Satman 1979).

Initial bitumen

E4: $S_{oi} = 54.12\%$; $S_{wi} = 17.85\%$ @9.2 h

E5: $S_{oi} = 53.02\%$; $S_{wi} = 35.63\%$ @7 h

**Figure 21.** Oil upgrading

Values of the recovery factor achieved during E4 and E5 were very close, but visual comparison of oil samples produced at the end of the experiments (9.2 and 7 hours for E4 and E5, respectively) indicated significant differences in oil upgrading (Figure 21). To understand the influence of water on ISC, oil produced from all the experiments was examined to understand the difference in the oil upgrade rate (Table 9). Two oil samples from each run, except for E2 (the production period was narrow), were chosen for comparison. The first sample was taken in the middle of the experiment and another at the end just before the run termination. Produced oil viscosity decreased by the end of each experiment. This shows how LTO and HTO reactions change the viscosity of the oil (Xia et al. 2001). As can be seen, less viscous oil was produced in E5 when compared with E4. Such behavior was described by Fumoto (Fumoto et al. 2010). With increasing initial water saturation, coke formation is suppressed and more light products appear at the outcome.

**Table 9.** Oil upgrading summary

| **Sample** | **Sampling time, h** | **Viscosity, cp (@23 $^{o}$C)** | **Gravity, $^{o}$API (@23 $^{o}$C)** |
|---|---|---|---|
| **Initial bitumen** | - | 53,146 | 8.85 |
| **E2: $S_{oi}$ = 33.77%; $S_{wi}$ = 34.05%** | 5.3 | 400 | 12.1 |
| **E4: $S_{oi}$ = 54.12%; $S_{wi}$ = 17.85%** | 4.6 | 871 | 13.2 |
| | 9.2 | 250 | 15.5 |
| **E5: $S_{oi}$ = 53.02%; $S_{wi}$ = 35.63%** | 3.5 | 257 | 16.1 |
| | 7 | 158 | 17.8 |
| **E6: $S_{oi}$ = 31.23%; $S_{wi}$ = 0%** | 3.6 | 18 | 21.3 |
| | 4.6 | 8.5 | 21.6 |
| **E7: $S_{oi}$ = 54.86%; $S_{wi}$ = 36.87%** | 3.6 | 115.2 | 16.4 |
| | 7.1 | 35 | 17.7 |

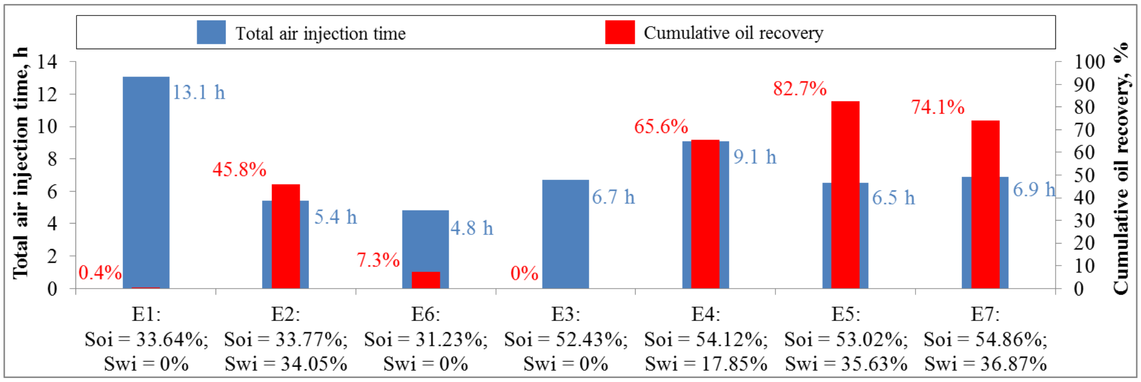

**Figure 22.** Air injection time vs. oil recovery factor

In Figure 22, oil recovery factors at different initial water saturations are compared with air injection time.

In E1, the combustion front sustained and propagated slowly; however, the amount of oil production was insufficient and corresponded only to 0.4% for 13.1 hours of air injection. This characterizes E1 as an unsuccessful run. In E2, 45.8% oil recovery factor was achieved with only 5.5 hours of air injection.

For nearly 6 hours of air injection during E3, no production was observed. However, 65.6% and 82.7% oil recovery factors were observed in E4 and E5 for 9.1 and 6.5 hours, respectively. Cumulative oil recovery-total air injection time ratio indicates that the best case scenario is E5, in which maximum oil recovery was achieved within the minimum air injection time.

Different oil recovery factors were attained in E5 and E7 with almost the same air injection time, with 82.7% of initially packed oil produced in E5 and 74.1% recovery factor in E7. ISC is a complex process with a lot of factors affecting its performance.

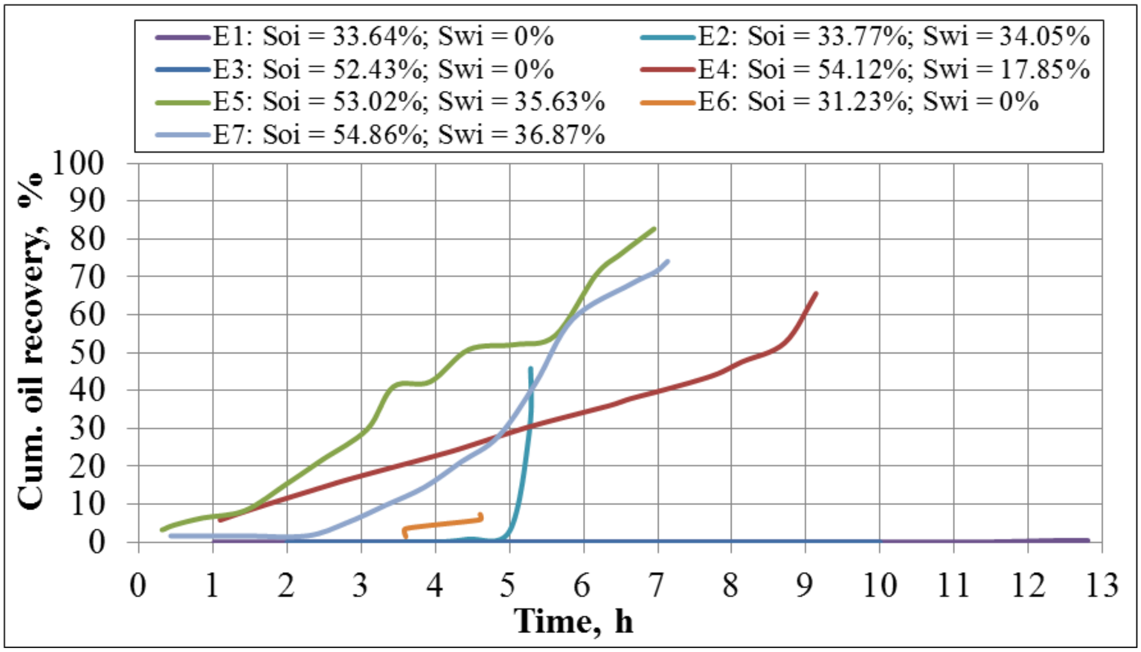

**Figure 23.** Cumulative oil recovery vs. time

The cumulative oil recovery versus time graph is represented in Figure 23. In this graph, each curve corresponds to the cumulative oil recovery for each run.

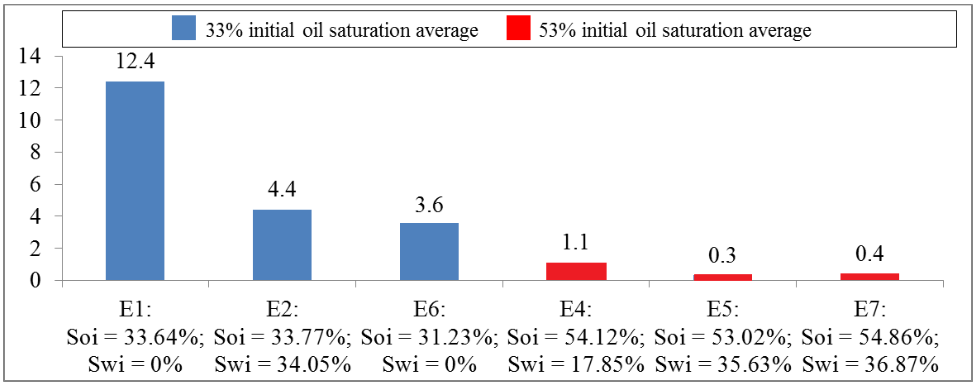

**Figure 24.** Oil production start time

In Figure 24, production start times are summarized. As initial water saturation increased from 0% in E1 to 34.05% in E2, the production start time decreased from 12.4 hours to 4.4 hours, respectively. This also occurred for cases E4 and E5. As initial water saturation increased from 17.85% in E4 to 35.63% in E5, production start time also decreased.

E7 demonstrated similar behavior to E5. Oil production occurred at nearly the same time after air injection was started. However, repeatability was not achieved for E1 and E6. This also proves that ISC is a complex process affected by a great variety of factors.

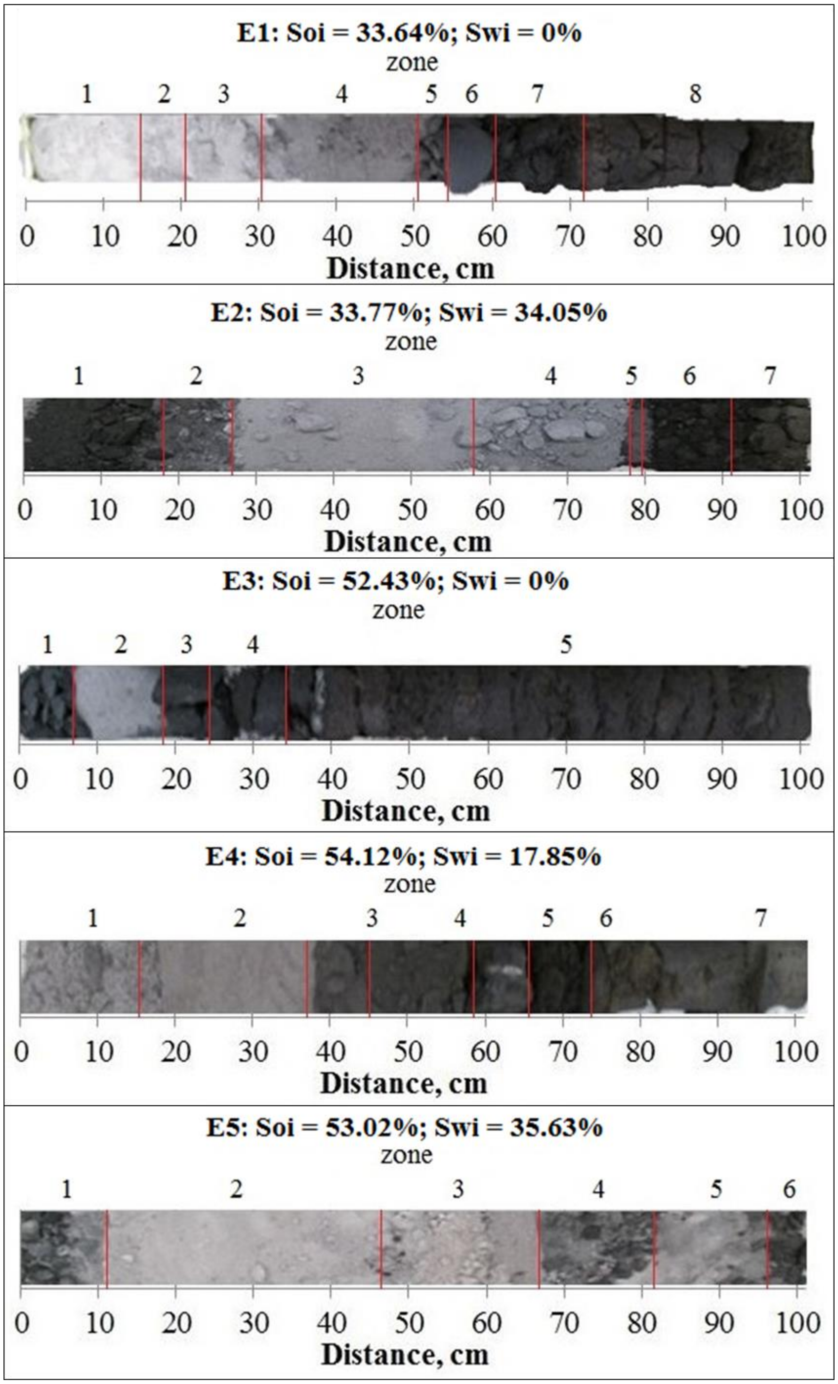

**Figure 25.** Postmortem photographs, E1-E5

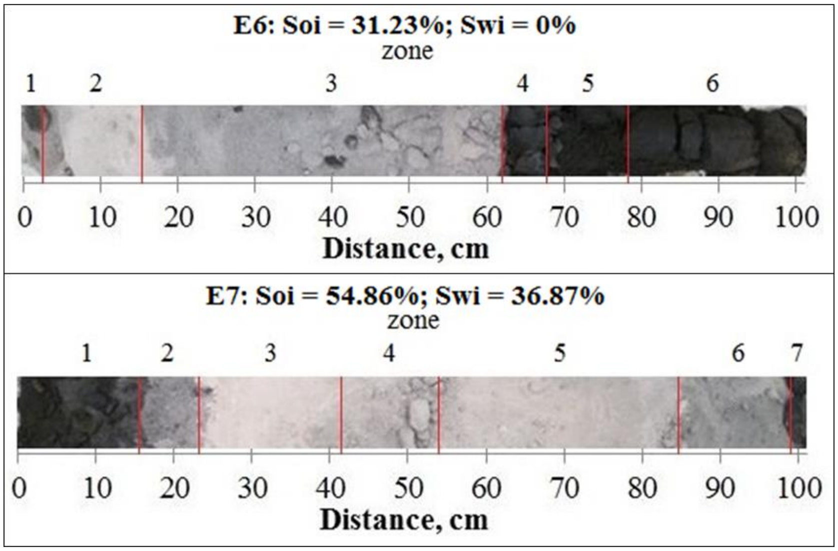

**Figure 26.** Postmortem photographs, E6-E7

Postmortem photographs of all the experiments are given in Figure 25 and in Figure 26. Postmortem analysis provides a better understanding of coke deposition and sweep efficiency along the combustion tube. The postmortem analysis of E1 indicates that the combustion front could only sweep 50 cm of the tube for 13.1 hours of the air injection time. Nearly half of the length of the tube remained untouched. In E2, the combustion front swept nearly the entire tube length, and only 20 cm remained untouched.

An initial coke-like residue zone can be observed between 0 and 14 cm in the postmortem of E2. The initial coke zone was observed by other researchers in the cases where initial water existed (Hascakir, Ross, et al. 2011). This means that the initial coke, generated under the $N_2$ injection in the medium containing initial water has a higher activation energy barrier than the initial coke formed in the absence of water (Glatz et al. 2011). While the activation energy is higher, the enthalpy is also higher, which assists the combustion process in sustaining. In E1, the initial coke-like residue zone did not exist. This is probably because of the high temperature maintained by the external heaters. As can be seen in Figure 9, an average temperature of 500 $^{o}$C held constant between the positions of 9.5 and 15.6 cm from 0 until 4 hours. A high temperature supported fuel consumption for this zone and as a result, the first 20 cm of E1 postmortem appear to be lighter when compared with the first 20 cm of E2 postmortem. Comparing the 30-40 cm zone of E1 postmortem with the 30-75 cm zone of E2 postmortem, the opposite conclusion can be made. The sand of E2 postmortem looks lighter. As can be seen in Figure 9, the temperature between positions 30.2 and 37 cm in E1 slightly exceeded 400 $^{o}$C, while temperature between 30.2 and 78.6 cm in E2 shifted 550 $^{o}$C. This resulted in better fuel consumption.

In E3, the smallest burned zone of nearly 11 cm can be observed. The major volume of the combustion tube remained untouched. In E4, the combustion front swept nearly half the length of the tube, which overlaps with a final front position estimated to be 50 cm (Figure 10). The sand color changed from light gray to dark gray at around 37 cm. The burned zone for E4 can be subdivided into two intervals: 10-37 cm and 37-50 cm (0-10 cm interval was affected by the heaters). In E4, the last temperature peak was registered at around 6 hours in the 36.8 cm position. An average front temperature corresponded to 352 $^{o}$C between 6 and 9 hours. The combustion front was located at 15 cm at around 0.5 hours (Figure 13). In Figure 18, it appears that the average front temperature between 0.5 and 6 hours was 472 $^{o}$C, while the average front temperature between 6 and 9 hours corresponded to only 352 $^{o}$C. The lower front temperature between positions 37 and 55 cm caused lower fuel consumption in the named region and as a result, the sand appears darker.

In E5, the combustion front swept nearly the entire tube length. In the postmortem photograph of E5, an evenly different zone is located between 68 and 82 cm. A leap at 84 cm was observed in Figure 9 and interpreted as left-behind coke. The evenly different zone observed in the postmortem photograph of E5 corresponds to the observations made from Figure 9.

The initial coke-like residue zone was observed in E3 and E5. It did not exist in E4. In E5, a higher temperature was received at ignition, however, the initial coke-like residue was consumed in E4 and left unconsumed in E5. Activation energy of the initial coke increased with increasing initial water saturation in the media.

Comparing experiments E1 and E6, it should be noted that the postmortem photographs of both runs look similar. In E1, 50 cm of the combustion tube were swept, while in E6 the combustion front swept 60 cm. The clearly burned sand at the beginning of the combustion tube was observed in both experiments. The burned zones are almost the same length in E1 and E6, however some initial coke-like residue was left unconsumed in E6.

Significant differences in the initial coke-like residue zones can be highlighted in comparing experiments E5 and E7. In E5, the initial coke-like residue zone corresponds to 5 cm only, while in E7, it occupies nearly 15 cm. Temperatures received at ignition (Figure 9) correspond to 883 $^{o}$C for E5 and to 681 $^{o}$C for E7. A higher temperature at ignition during E5, explains the difference in the initial coke-like residue zone length.

**Table 10.** Postmortem analysis summary

| **Parameter, unit** | | | **Value** | | | | | | |
|---|---|---|---|---|---|---|---|---|---|
| **Experiment** | | | **E1** | **E2** | **E3** | **E4** | **E5** | **E6** | **E7** |
| **$S_{oi}$, %** | | | **33.64** | **33.77** | **52.43** | **54.12** | **53.02** | **31.23** | **54.86** |
| **$S_{wi}$, %** | | | **0** | **34.05** | **0** | **17.85** | **35.63** | **0** | **36.87** |
| **zones** | **1** | **interval, cm** | 0-15.2 | 0-18.2 | 0-6.1 | 0-14.2 | 0-11.6 | 0-2.5 | 0-15.2 |
| | | **weight, g** | 521.3 | 1587 | 508.1 | 963.4 | 803.6 | 186.3 | 1123.6 |
| | **2** | **interval, cm** | 15.2-21.3 | 18.2-26.3 | 6.1-18.2 | 14.2-35.9 | 11.6-47 | 2.5-16 | 15.2-22.8 |
| | | **weight, g** | 238 | 636.06 | 736.3 | 1269.8 | 2598 | 808.8 | 615.3 |
| | **3** | **interval, cm** | 21.3-30.4 | 26.3-57.7 | 18.2-23.8 | 35.9-44 | 47-67.8 | 16-61.5 | 22.8-40.9 |
| | | **weight, g** | 447 | 1583.4 | 429.3 | 523.4 | 1511.5 | 3183.4 | 1076.8 |
| | **4** | **interval, cm** | 30.4-51.1 | 57.7-77.9 | 23.8-33.4 | 44-59.2 | 67.8-80.9 | 61.5-67.5 | 40.9-53.6 |
| | | **weight, g** | 1156.3 | 1460 | 1378.4 | 1536.8 | 888.1 | 357 | 885.8 |
| | **5** | **interval, cm** | 51.1-53.6 | 77.9-78.9 | 33.4-101.2 | 59.2-64.7 | 80.9-96.6 | 67.5-78 | 53.6-84.5 |
| | | **weight, g** | 184.8 | 83.1 | 4723.2 | 629.7 | 1158.9 | 832.6 | 2499.5 |
| | **6** | **interval, cm** | 53.6-60.7 | 78.9-91.1 | | 64.7-72.9 | 96.6-101.2 | 78-101.2 | 84.5-99.2 |
| | | **weight, g** | 514.1 | 802.3 | | 630 | 351 | 1448 | 1205.1 |
| | **7** | **interval, cm** | 60.7-73.9 | 91.1-101.2 | | 72.9-101.2 | | | 99.2-101.2 |
| | | **weight, g** | 2031.4 | 961 | | 2197.3 | | | 141.1 |
| | 8 | **interval, cm** | 73.9-101.2 | | | | | | |
| | | **weight, g** | 2210.5 | | | | | | |
| **Total** | | **length, cm** | 101.2 | 101.2 | 101.2 | 101.2 | 101.2 | 101.2 | 101.2 |
| | | **weight, g** | 7303.4 | 7112.9 | 7775.3 | 7750.4 | 7311.1 | 6816.1 | 7547.2 |

In Table 10, postmortem zones with corresponding lengths and weights are represented.

In E1, zones 1-4 corresponded to the burned zone. In the burned zones, the sand color changed from white (zone 1) to dark gray (zone 4). Zones 5 and 6 represent coke-like residue zones. Coke-like residue properties in zones 5 and 6 are different. Zone 7 is defined as an oil bank and zone 8 represents an untouched zone.

In E2, zone 1 represents the initial coke-like residue zone. The initial coke-like residue zone observed in E2 is the largest one within the seven conducted experiments. Zones 2-4 form the burned zone. In E2, a thin layer of 1 cm, defined as zone 5, represents the coke-like residue zone. The coke-like residue zone is followed by the oil bank (zone 6), and the untouched zone (zone 7).

In E3, the initial coke-like residue zone is also observed (zone 1). Zone 2 characterizes the burned zone and the sand color in zone 2 is gray. Zone 3 is defined as a coke-like residue zone and zones 4 and 5 represent the oil bank and the untouched zone, correspondingly.

The initial coke-like residue zone is not observed in E4. Zones 1-3 correspond to the burned zone. Zones 4 and 5 represent the coke-like residue zone. The coke-like residue in zone 5 is highly consolidated. Zones 6 and 7 represent the oil bank and the untouched zone.

In E5, zone 1 represents the initial coke-like residue zone that was not fully consumed. Zones 2-5 represent the burned zone. Properties of zone 4 are evenly different. A lot of coke-like residue was left unconsumed in zone 4. Zone 6 represents the coke-like residue zone.

In E6, traces of the initial coke-like residue, created under the $N_2$ injection, are observed in zone 1. Both zones 2 and 3 contribute to the burned zone. Zone 4 corresponds to the coke-like residue zone. Zones 5 and 6 represent the oil bank and the untouched zone, respectively.

In E7, initial coke-like residue zone (zone 1) is distinguished. Zones 2-6 represent the burned zone; and zone 7 is a coke-like residue zone.

Lump formations were found in the runs E2, E5, E6, and E7. The highly energetic nature of ISC rearranges unconsolidated sand-clay mixture and compresses it (Hascakir, Glatz, et al. 2011). Clay and coke-like residue serve as a cementing material.

Mass balance calculations were performed after the postmortem analysis. The following equations were used for mass balance calculations:

$$m_{sp} + m_{ig} = m_{sp-m} + m_{pl} + m_{pg}$$

where

$m_{sp}$ - mass of packed sample, g

$m_{ig}$ - mass of injected gas, g

$m_{sp-m}$ - mass of postmortem sample, g

$m_{pl}$ - mass of produced liquid, g

$m_{pg}$ - mass of produced gas, g

The mass of injected air was calculated with the following formula:

$$m_{ig} = \frac{q_i * t_i * P_i * M}{z\,|(689\,kPa, 300\,K) * R * T_i}$$

where

$q_i$ - injection flow rate, $m^3/h$

$t_i$ - injection time, h

$P_i$ - injection pressure, kPa

$M$ - gas mixture molar mass, kg/mol

$z\,|(689\,kPa, 300\,K)$ - gas mixture compressibility factor

$R$ - universal gas constant, 8.31 J/mol-K

$T_i$ - injection temperature, K

The following assumptions were made:

- the injected air consists of 21% $O_2$ and 79% $N_2$;
- the produced gas mixture consists of the following components: $CO_2$, CO, $CH_4$, $O_2$, and $N_2$;
- injection and production flow rates are equal;
- injected air and produced gases have the same temperature;
- pressure on the inlet of the combustion tube is equal to the pressure on the inlet of the gas analyzer.

The molar mass of the produced gas mixture was calculated according to the formula:

$$M_{pg} = y_{CO_2} * M_{CO_2} + y_{CO} * M_{CO} + y_{CH_4} * M_{CH_4} + y_{O_2} * M_{O_2} + y_{N_2} * M_{N_2}$$

where

$y_i$ – mixture component molar fraction, frac.

$M_i$ – mixture component molar mass, kg/mol

The results of the mass balance calculations are summarized in Table 11. The mass of the packed sample, the mass of postmortem, and the mass of produced liquid were measured. The mass of produced gas was calculated according to the equations above.

**Table 11.** Mass balance summary

| **Parameter, unit** | **Value** | | | | | | |
|---|---|---|---|---|---|---|---|
| **Experiment** | **E1** | **E2** | **E3** | **E4** | **E5** | **E6** | **E7** |
| **$S_{oi}$, %** | **33.64** | **33.77** | **52.43** | **54.12** | **53.02** | **31.23** | **54.86** |
| **$S_{wi}$, %** | **0** | **34.05** | **0** | **17.85** | **35.63** | **0** | **36.87** |
| **Sample packed, g** | 7,450 | 7,941.3 | 7,975.8 | 8,317 | 8,552.2 | 7,034 | 8,893 |
| **Sample postmortem, g** | 7,303.4 | 7,112.9 | 7,775.3 | 7,750.4 | 7,311.1 | 6,816.1 | 7,547.2 |
| **Liquid production, g** | 20.1 | 754.8 | 0 | 461.6 | 1,084.7 | 88.9 | 1,194.1 |
| **Gas production, g** | 126.5 | 73.64 | 200.5 | 105 | 156.4 | 129 | 151.7 |

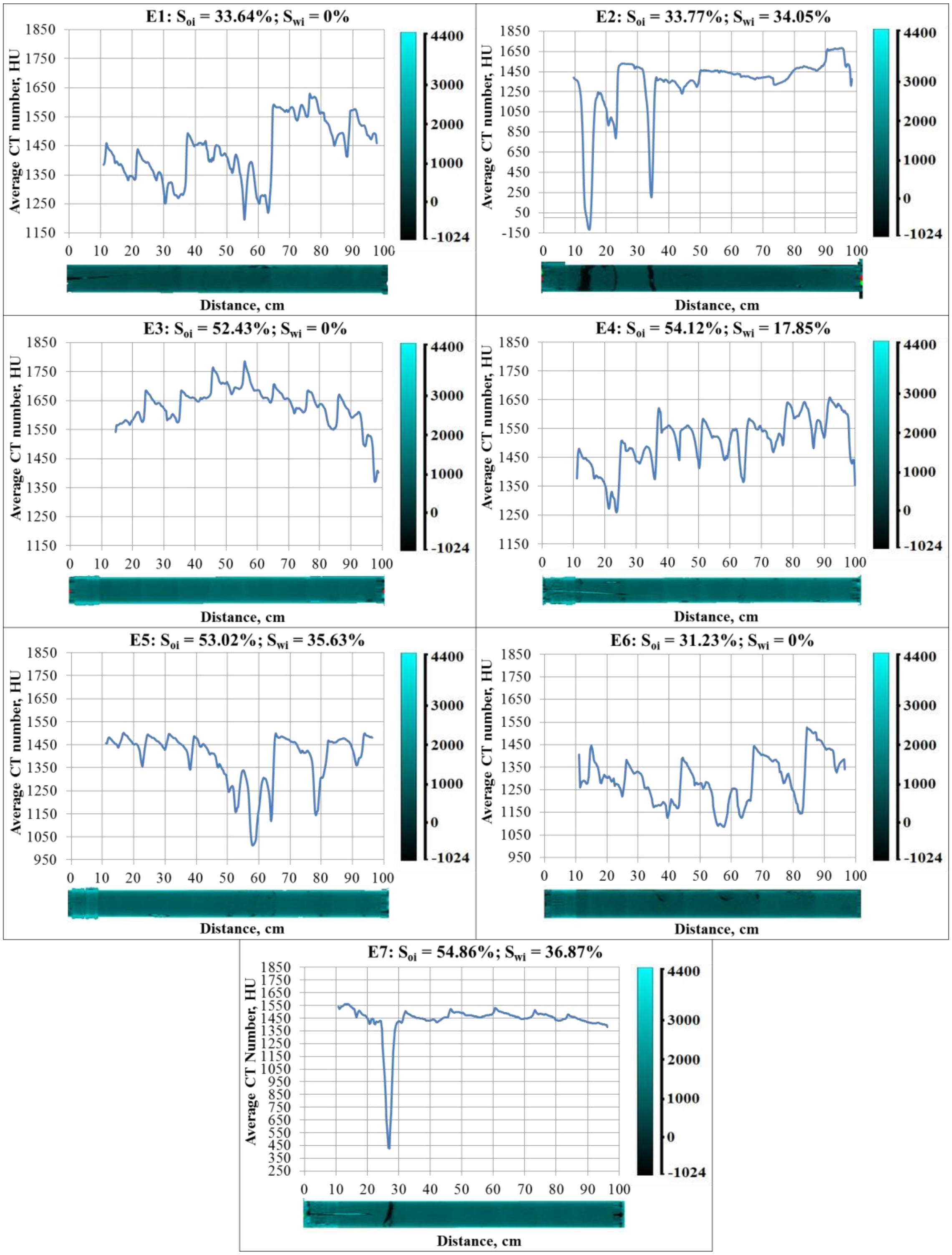

**Figure 27.** Average CT number in position for all postmortem samples

At the end of each experiment, the combustion tube was scanned in X-ray with the application of a CT scanner. The CT scan provides radiodensity in Hounsfield units (Withjack et al. 2003). Radiodensity refers to the relative inability of an X-ray to pass through material, and it is proportional to its density (Novelline et al. 1997). The density of distilled water at standard conditions is equal to 0 HU and the density of air corresponds to -1000 HU (Akin et al. 2003). The CT scan helps to understand displacement in the porous media and fractures created spontaneously during ISC due to the highly energetic nature of the combustion front, which causes expansion in gases. This gas expansion rearranges unconsolidated sand and forms fingers (Hascakir, Glatz, et al. 2011).

Figure 27 represents the average CT number versus distance graphs. The average CT number provides quantitative information on the sample density. For the CT number versus distance graphs, 0-10 cm interval is not represented because band heaters were installed within named positions on the tube. Band heaters increase the average density in a cross section and create artifacts on cross-sectional images. At the bottom of each graph, a combustion tube reconstruction from CT images is attached. To the right of each graph a scale in Hounsfield units is placed to assist in interpreting the combustion tube reconstruction, while the average CT number provides quantitative data.

In E1, the average CT number increases by the end of the combustion tube. As mentioned before, in E1, the combustion front swept only 50 cm of the tube. The volume located between 50 and 65 cm was affected by the heat of combustion and shows lower density. The untouched zone is located between 65 and 101.2 cm. Significant drops in the average CT number correspond to positions 21, 30, 35, 55, 60, 64, and 89 cm.

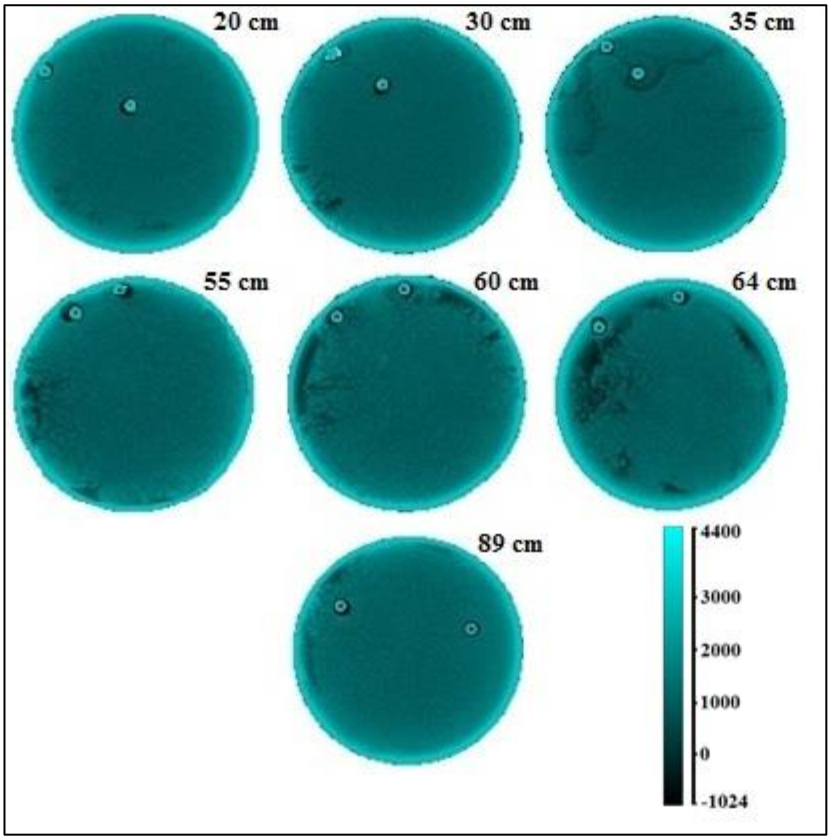

**Figure 28.** Cross-sectional images for E1: $S_{oi}$ = 33.64%; $S_{wi}$ = 0%

Cross-sectional images of the combustion tube for E1 are represented in Figure 28. Minor fractures can be mentioned in positions 21, 30, 35, and 89 cm. The lowest average CT numbers correspond to positions 55 and 64 cm (Figure 27). As can be seen in Figure 28, large fractures were created in cross-sections corresponding to those positions.

In E2, density is almost uniformly distributed along the combustion tube (Figure 27). Three longitude fractures were created in positions corresponding to 15, 23, and 35 cm (Figure 29).

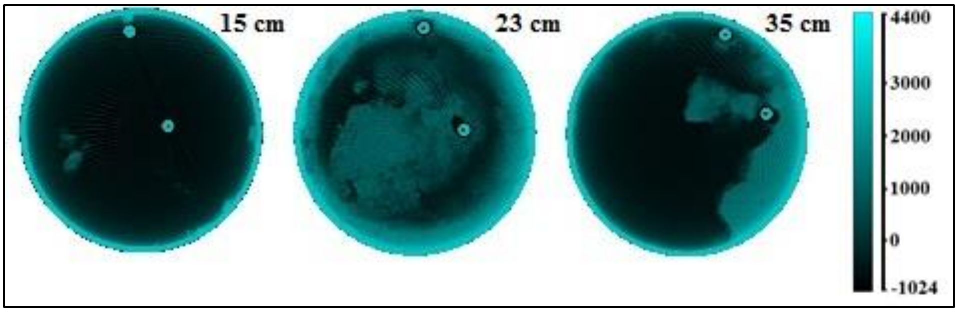

**Figure 29.** Cross-sectional images for E2: $S_{oi}$ = 33.77%; $S_{wi}$ = 34.05%

The first fracture located 15 cm below the top of the combustion tube had a large fissure opening of nearly 5 cm. Fractures can affect ISC dramatically. Referring back to the gas composition versus time graph for E2 (Figure 15), there is a significant drop in the $CO_2$ concentration that occurred at 3 hours. At this time, the front position corresponded to 35 cm (Figure 10), and the fracture was located in the exact same position. Creating an easy pathway for air, fractures decrease fuel consumption, and as a result, the front temperature falls (Figure 18). Fractures can be a possible reason for ISC collapse.

The highest average CT number corresponds to E3. The lowest CT numbers are observed for the first 10-20 cm of the combustion tube. This zone represents a burned zone. For the rest of the combustion tube length, the average CT number is around 1640

HU, indicating a huge untouched zone. Minor fluctuations in density distribution along the combustion tube can be observed in positions 34, 84, and 97 cm. As can be seen in Figure 30, two fractures are located in positions 84.4 and 96.7 cm. One can also observe air bypassing that occurred around the thermocouple in position 34 cm. It is represented by a black environ around two bright dots, which stand for metal thermowells.

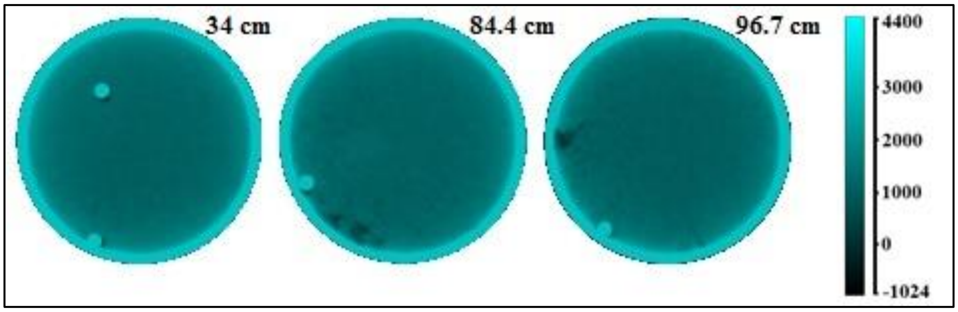

**Figure 30.** Cross-sectional images for E3: $S_{oi}$ = 52.43%; $S_{wi}$ = 0%

CT number variations for E4 are not as uniform as for E3 (Figure 27). The average CT number increases by the end of the combustion tube. This overlaps with the postmortem analysis of E4 (Figure 25). As can be seen, a color change starts at 37 cm. Significant drops in the average CT number values can also be mentioned for E4. The most notable fluctuations in density can be highlighted in positions 24, 36, 44, 50, 58, 64, 74, 76, 87, and 90 cm. On the cross-sectional images for the named positions (Figure 31) fractures, air bypassing and a hole from a previously inserted thermowell can be found. When the combustion tube was sealed and thermowells were installed, the fitting (which sealed one of the thermowells) was broken, so it was necessary to take the thermowell out, replace the fitting, and reinsert the thermowell. As can be seen in Figure 31, the thermowell did not follow its previous path through the sand pack but created a new one. The old trajectory of the thermowell can be followed from cross-sectional images starting from 24 up to 76.5 cm. A void space, created by a thermowell, served as an easy pathway for the injected air.

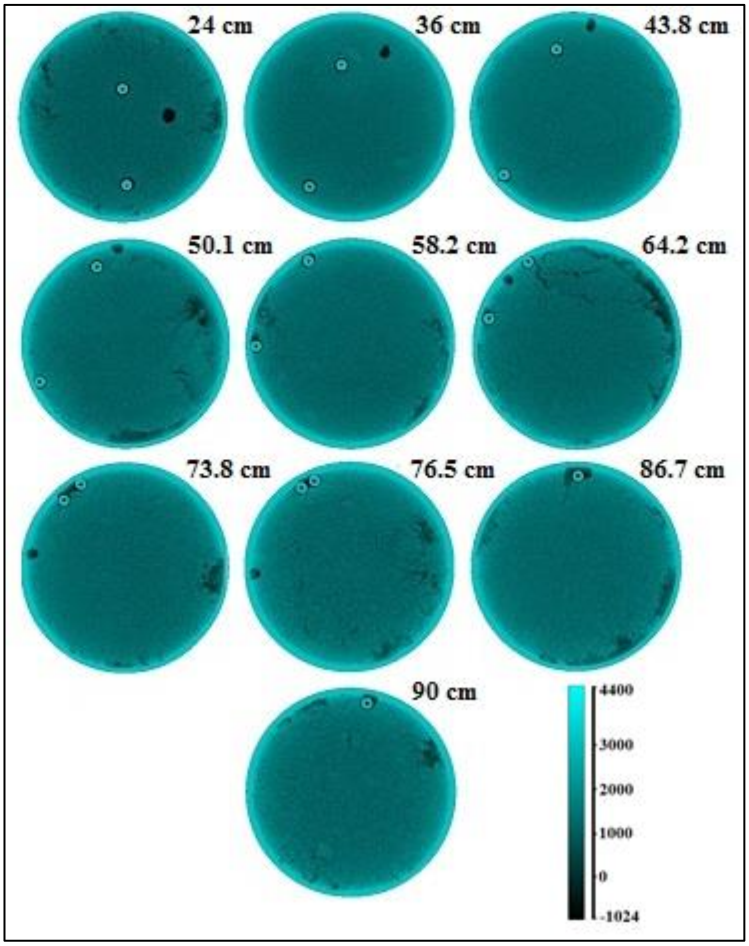

**Figure 31.** Cross-sectional images for E4: $S_{oi}$ = 54.12%; $S_{wi}$ = 17.85%

An example of air bypassing that occurred during the E4 run is represented in **Figure 32**. Injected air passed through the zone of the lowest flow resistivity that was created near the thermowell. As a result, air did not distribute effectively in the horizontal plane, and fuel was not consumed evenly in the cross section. Because heat generation is defined in energy per amount (J/kg) unit, if less coke is burned, less heat will be produced, which will lead to the combustion front temperature decrease (Burger 1972).

**Figure 32.** Air bypassing around the thermowell (from E4 postmortem)

For E5, density distribution along the combustion tube appears to be more uniform (Figure 27). Average CT number values do not exceed 1500 HU and mainly vary around the value of 1470 HU. In E5, at least two fractures created at 20 and 50 cm of the combustion tube were expected. This conclusion was based on the behavior observed in E2 and similar behavior observed in E5 (Figure 18). In E2, fractures were created in positions corresponding to 15 and 35 cm (Figure 29). Possible signs of fractures include a temperature peak approaching 600 $^{o}$C followed by the $CO_2$ concentration drop. These signs were observed in E5 at 3.2 and 4 hours (Figure 18). At this time, the combustion front was located around 20 and 50 cm, respectively. As can be seen in Figure 33, fractures appeared around 23 and 52 cm. Fractures were also created at 38, 58, 64, and 79 cm of the combustion tube.

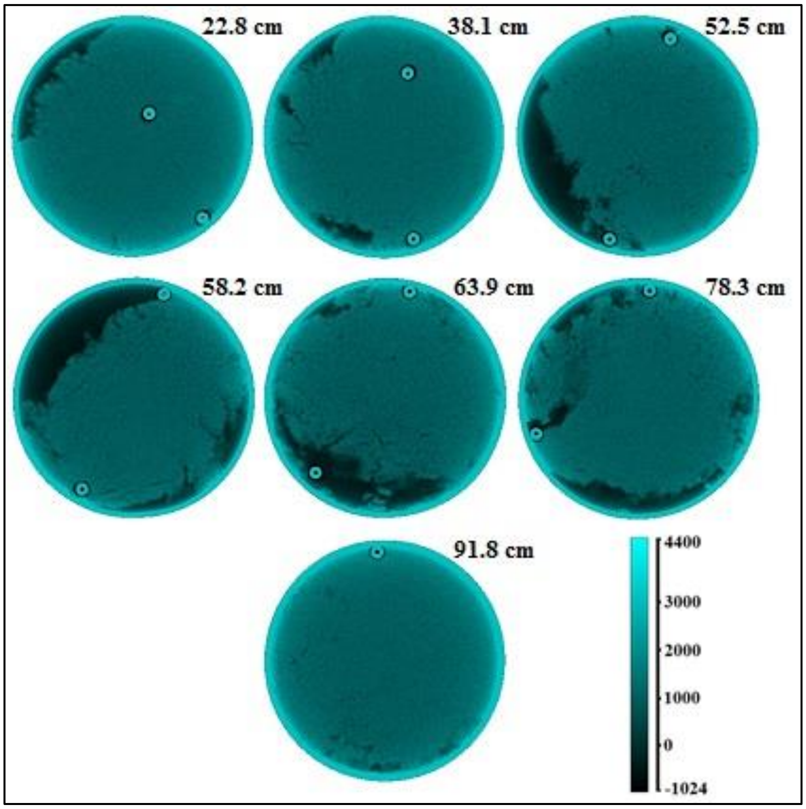

**Figure 33.** Cross-sectional images for E5: $S_{oi}$ = 53.02%; $S_{wi}$ = 35.63%

In E6, the average CT number increased by the end of combustion tube, as in E1. In E6, fractures and air bypasses created along the combustion tube should also be noted.

The most significant density fluctuations are associated with the following positions: 11.5, 24.9, 36.6, 55.8, 63, 82.5, and 93.9 cm. Cross-sectional images for the named positions are represented in Figure 34.

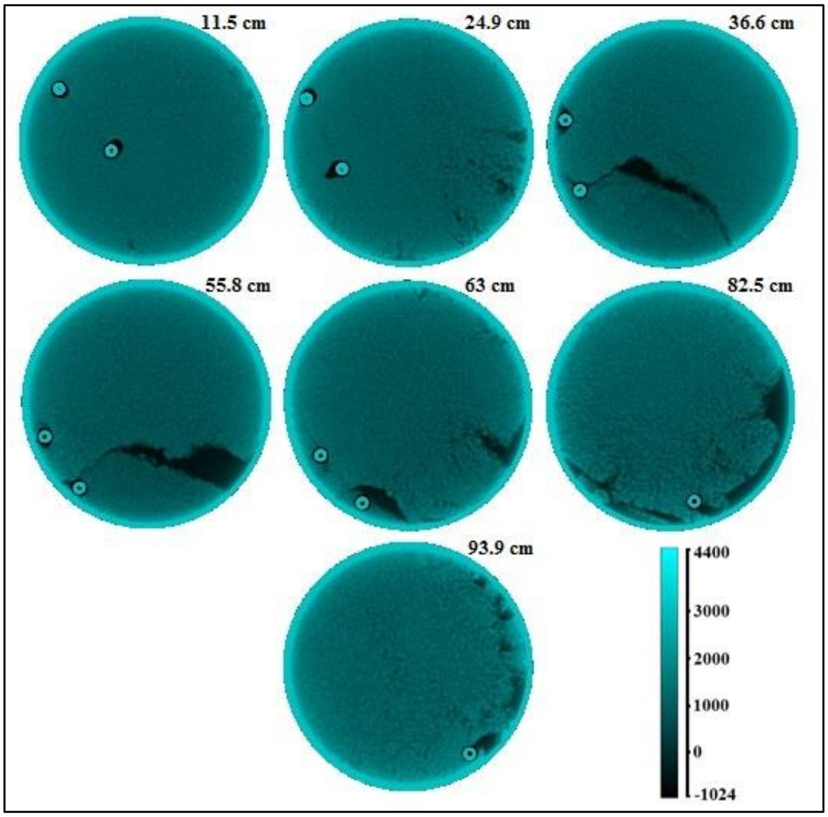

**Figure 34.** Cross-sectional images for E6: $S_{oi}$ = 31.23%; $S_{wi}$ = 0%

In E7, an average CT number versus time curve forms a nearly straight line. In this run, the combustion front swept nearly the entire combustion tube length. Comparing the average CT number graphs for E5 and E7, similarities can be found. The density distribution appears to be more uniform in E7, but an average CT number varies between

1350 and 1550 HU. Fractures were created in both cases. In E7, only one fracture, located at 27 cm of the combustion tube, can be observed. The cross-sectional image for E7 is represented in Figure 35.

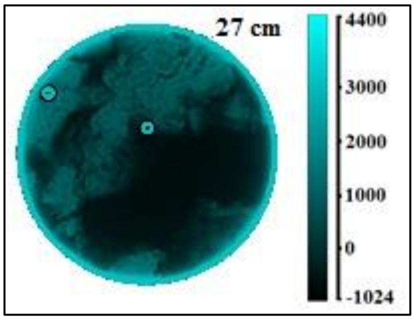

**Figure 35.** Cross-sectional image for E7: $S_{oi}$ = 54.86%; $S_{wi}$ = 36.87%

# CHAPTER IV

# NUMERICAL SIMULATION

Since the greatest oil recovery was obtained in E5, numerical studies were achieved for this experiment. The essence of this study was to obtain a chemical reaction scheme, which is capable of reproducing temperature front parameters such as peak temperature and front velocity. For this purpose, the Steam Thermal Advanced Reservoir Simulator (STARS) by Computer Modeling Group (CMG) was used (2009). This is a new generation advanced processes reservoir simulator, which enables modeling of such processes as polymer, gel, foam flooding, and thermal EOR methods, including but not limited to steam flooding, cyclic steam injection, steam with additives, and dry and wet in-situ combustion.

The combustion tube used during the experiments was modeled with a one-dimensional Cartesian grid of 102 cm length divided into 40 blocks in z direction. The surface area of each block in the xy plane corresponded to the cross-sectional area of the combustion tube. Grid properties of the numerical model are summarized in Table 12, and the grid is represented in Figure 36.

**Table 12.** Grid properties

| Parameter, unit | Value |
|---|---|
| **Number of blocks in x direction** | 1 |
| **Number of blocks in y direction** | 1 |
| **Number of blocks in z direction** | 40 |
| **Grid block dimensions, m** | 0.0647x0.0647x0.0255 |

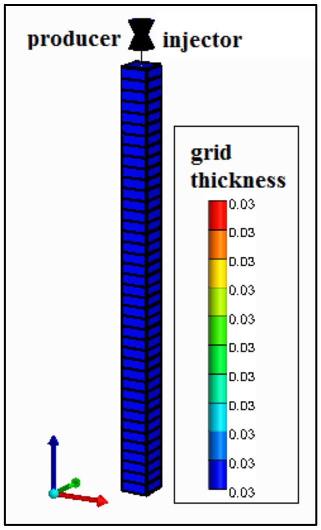

**Figure 36.** Grid sizes used in the simulation study

Reservoir rock porosity was set according to the measured porosity of the sand-clay mixture and corresponded to 32%. Sand pack permeability, thermal conductivities of rock, bitumen, water, and gas were not measured in the laboratory, so, the values for the named parameters were chosen according to CMG STARS manual recommendations (2009). A simple mixing rule was chosen to calculate the thermal conductivity of the fluid saturated rock. The mixing rule is described in the following equation:

$$k_{mix} = m_f * \left(k_w * S_w + k_o * S_o + k_g * S_g\right) + (1 - m) * k_r + \left(m - m_f\right) * k_s$$

where

$k_{mix}$ - thermal conductivity of saturated rock, J/m-hr-$^{o}$C

$k_o$ - thermal conductivity of oil, J/m-hr-$^{o}$C

$k_w$ - thermal conductivity of water, J/m-hr-$^{o}$C

$k_g$ - thermal conductivity of gas, J/m-hr-$^{o}$C

$k_s$ - thermal conductivity of solid, J/m-hr-$^o$C

$k_r$ - thermal conductivity of rock, J/m-hr-$^o$C

$S_o$ - oil saturation, frac.

$S_w$ - water saturation, frac.

$S_g$ - gas saturation, frac.

$m$ - porosity, frac.

$m_f$ - porosity, saturated with fluids only, frac.

The reservoir rock had the following parameters, as summarized in Table 13.

**Table 13.** Rock and fluid properties

| **Parameter, unit** | **Value** |
|---|---|
| **Porosity** | 0.32 |
| **Permeability, mD** | 12,700 |
| **Rock heat capacity, J/m$^3$-$^o$C** | 2,347*10$^6$ |
| **Rock thermal conductivity, J/m-hr-$^o$C** | 11,416.67 |
| **Bitumen thermal conductivity, J/m-hr-$^o$C** | 479.16 |
| **Water thermal conductivity, J/m-hr-$^o$C** | 2,229.17 |
| **Gas thermal conductivity, J/m-hr-$^o$C** | 100 |
| **Solid phase thermal conductivity, J/m-hr-$^o$C** | 18,750 |

Initial fluid saturations corresponded to those of the experiment. The pore medium was saturated with 53% initial bitumen and 35% initial water.

Air, containing 21% $O_2$ and 79% $N_2$, was injected from the top of the tube and the combustion front was propagating downwards. The injector well perforation corresponded to grid block 1 1 40, while the producer well bottomhole was located in the block 1 1 1. Initial conditions of the tube were 689 kPa and 23 $^o$C. To simulate external heating with electrical heaters, the temperature of grid blocks 1 1 36 through 1 1 40 was set to 500 °C.

A normalized Stone's model was used for the description of the three-phase flow (Stone 1973). Stone's model allows generation of three-phase flow diagram basing on two-phase relative permeability curves. Water is the wetting phase, gas is the non-wetting phase, and oil is the middle phase. Two-phase relative permeability curves, represented in Figure 37, were used to generate three-phase relative-permeability curves.

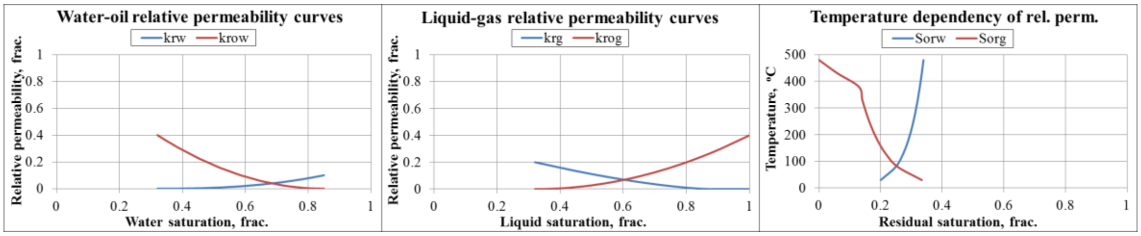

**Figure 37.** Two phase relative permeability curves

Relative permeability of oil and water changes with temperature (Davidson 1969, Poston et al. 1970, Ashrafi et al. 2012). This change is important for thermal EOR processes. Effect of temperature on relative permeability curves was introduced into the simulator with relative permeability curves endpoints for various temperatures (Table 14).

**Table 14.** Relative permeability curves endpoints temperature dependency

| **Temperatures** | $S_{orw}$ | $S_{org}$ |
|---|---|---|
| **30 °C** | 0.200 | 0.334 |
| **80 °C** | 0.249 | 0.255 |
| **130 °C** | 0.273 | 0.215 |
| **180 °C** | 0.289 | 0.189 |
| **230 °C** | 0.302 | 0.169 |
| **280 °C** | 0.312 | 0.153 |
| **330 °C** | 0.320 | 0.140 |
| **380 °C** | 0.327 | 0.129 |
| **430 °C** | 0.333 | 0.06 |
| **480 °C** | 0.338 | 0 |

Eight chemical pseudo-components were identified in the model. The components appear in four phases, namely aqueous, oleic, gaseous, and solid. The aqueous phase is represented with one component ($H_2O$). Due to the lack of information about Peace River bitumen composition, the oleic phase consisted of two components, representing initial bitumen and upgraded produced oil, named respectively as Heavy oil and Light oil. The four gaseous components included injected and produced gases: $O_2$, $N_2$, $CO_2$, and CO. The solid phase was represented with a Coke component. The components' properties are summarized in Table 15.

**Table 15.** Properties of components

| Component | Molecular weight, g/mol | Critical temperature, °C | Critical pressure, kPa | Density, kg/m$^3$ |
|---|---|---|---|---|
| **$H_2O$** | 18.02 | 374.15 | 2,2048 | 1,000 |
| **Heavy oil** | 527.5 | 614 | 838 | 1,008.2 |
| **Light oil** | 156.7 | 344 | 1,983 | 977 |
| **$CO_2$** | 44 | 31.05 | 7,376.46 | - |
| **$O_2$** | 31.99 | -118.55 | 5,046 | - |
| **CO** | 28 | -140.25 | 3,496 | - |
| **$N_2$** | 28 | -146.95 | 3,394 | - |
| **Coke** | 13 | - | - | 916 |

ISC is non-isothermal process, so, the simulation requires a temperature dependency of liquid components viscosity. CMG STARS allows introduction of the viscosity-temperature dependency as a table, or in the form of coefficients $a$ and $b$, used for solving the following equation:

$$\mu_i = a * e^{\left(\frac{b}{T_i}\right)}$$

where

$\mu_i$ - liquid component viscosity, cp

$T$ - temperature, K

$a$ - viscosity-temperature dependency coefficient, cp

$b$ - viscosity-temperature dependency coefficient, K

Coefficients $a$ and $b$ can be obtained from two points on the $\mu = f(T)$ curve by solving the following equations:

$$\mu_1 = a * e^{\left(\frac{b}{T_1}\right)}$$

$$\mu_2 = a * e^{\left(\frac{b}{T_2}\right)}$$

$$b = \frac{ln(\mu_1) - ln(\mu_2)}{\frac{1}{T_1} - \frac{1}{T_2}}$$

$$a = \frac{\mu_1}{e^{\left(\frac{b}{T_1}\right)}}$$

The viscosity of the original bitumen and the produced oil were measured in the laboratory (Figure 38). Coefficients $a$ and $b$, obtained for the original bitumen and the produced oil, are summarized in Table 16.

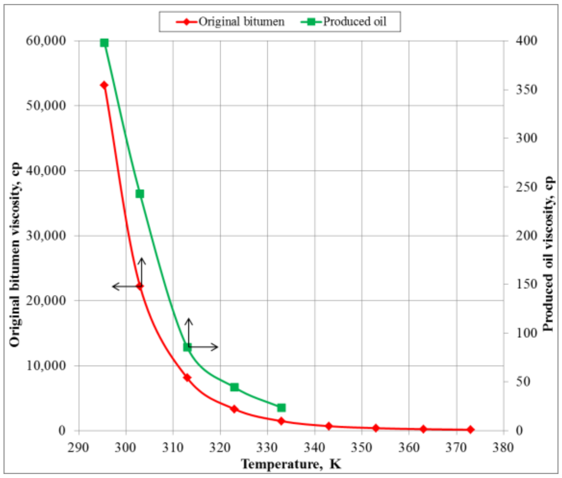

**Figure 38.** Viscosity variation with temperature

**Table 16.** Viscosity correlation coefficients used in the simulation study

| **Component** | **Coefficient, unit** | |
|---|---|---|
| | ***a*, cp** | ***b*, K** |
| **Original bitumen** | $1.601*10^{-8}$ | 8,519.51 |
| **Produced oil** | $4.859*10^{-9}$ | 7,425.551 |

The reaction rates of ISC are described with the following equation:

$$r = \frac{dC_f}{dt} = k * P_{O_2}^{\alpha} * C_f^{\beta}$$

where

$r$ - reaction rate

$k$ - reaction rate constant

$C_f$ - fuel concentration, kg/m$^3$

$P_{O_2}$ - oxygen partial pressure, kPa

$\alpha$ - reaction order in respect to oxygen partial pressure

$\beta$ - reaction order in respect to fuel concentration

The reaction rate constant is defined with the Arrhenius equation:

$$k = A * e^{\left(-\frac{E_a}{R*T}\right)}$$

where

$A$ - frequency factor

$E_a$ - activation energy, J/mol

The chemical reactions occurring during ISC were simplified to two reactions: the cracking of bitumen to light oil and coke, and coke burning:

$$(R1)\ 1\ Heavy\ oil =\ 2.35\ Light\ oil + 13\ Coke$$

$$(R2)\ 1\ Coke + 1.1\ O_2 = 0.74\ CO_2 + 0.26\ CO + 0.5\ H_2O$$

The main parameters that define chemical reactions are activation energy, frequency factor, and reaction enthalpy. The kinetic parameters of reactions are summarized in Table 17.

**Table 17.** Kinetic parameters of reactions

| **Reaction** | **Reaction kinetic parameters** | | |
|---|---|---|---|
| | **Frequency factor** | **Activation energy, J/mol** | **Enthalpy, J/mol** |
| **R1** | $10^{12}$ | * | 0 |
| **R2** | $6*10^5$ | 58,617.96 | $4.75*10^5$ |

* the cracking reaction was set as temperature dependent; values are summarized in Table 18.

**Table 18.** Activation energy values for the cracking reaction

| **Temperature, $^oC$** | **Activation energy, J/mol** |
|---|---|
| **50** | $10^6$ |
| **100** | 62,804.86 |

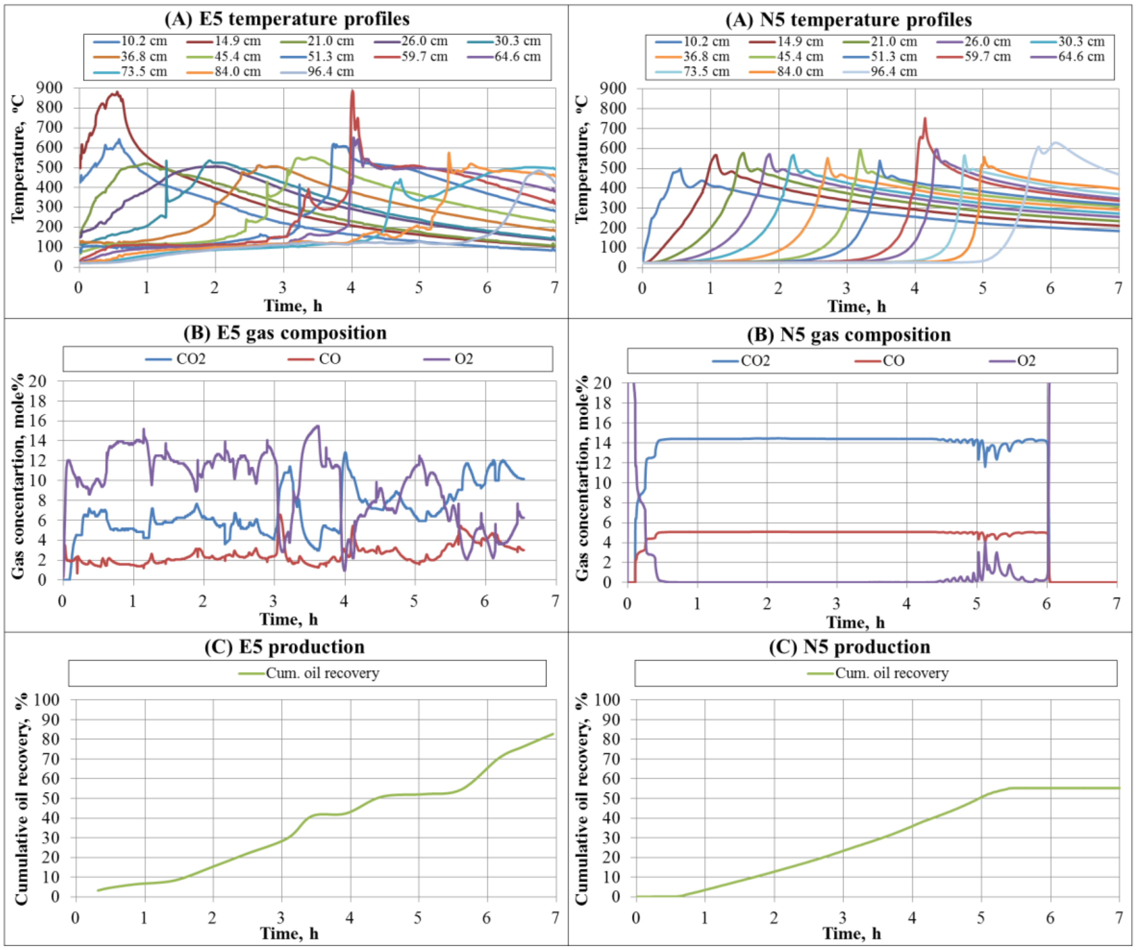

**Figure 39.** Experimental (E5) and numerical simulation (N5) results

The simplified model reproduced trends observed during the experiment (Figure 39). Individual temperature profiles registered during the experiment and achieved in numerical simulation are represented in Figure 40. The first temperature peak, registered by the thermocouple in position 14.9 cm, was not reproduced, as it resulted from the burning of coke created under the $N_2$ injection conditions.

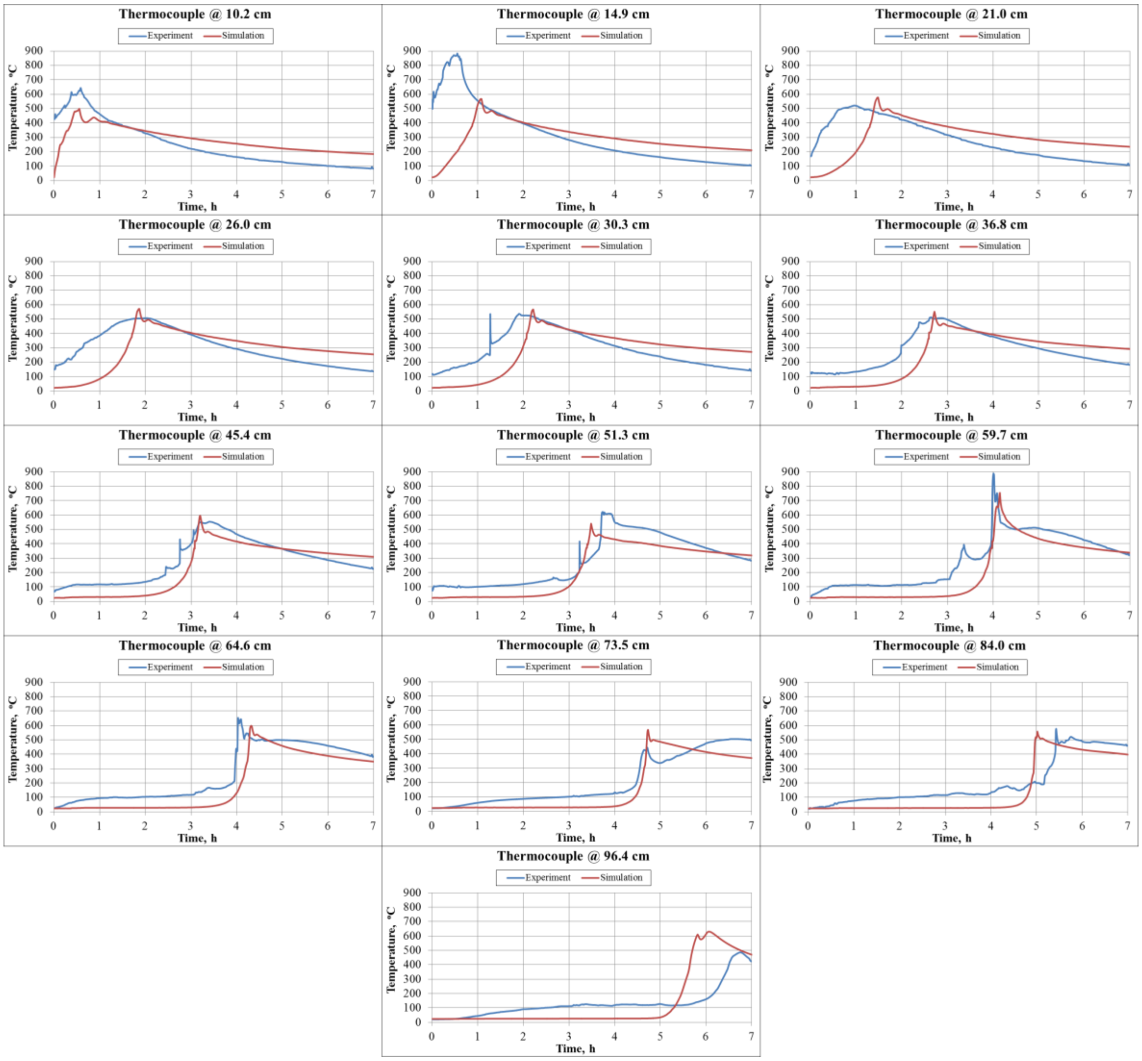

**Figure 40.** Temperature matches for each thermocouple position for E5

The numerical model showed a stable combustion front propagation along the combustion tube. Good matches were received for thermocouples in positions 26, 30.3, 36.8, 45.4, 59.7, 64.6, and 73.5 cm.

As can be seen in Figure 39 A, the numerical model showed a good match with the combustion front velocity. In E5, the combustion front velocity, estimated between positions 84 and 96.4 cm, corresponded to 12.4 cm/h. While in the numerical study, the combustion front velocity, estimated between the same positions, corresponded to 11.8 cm/h.

Gas composition was not reproduced perfectly (Figure 39 B) as the numerical model did not reflect the transition between a stable and an unstable combustion period. With the average CT number, it was proved that the combustion tube media was not uniform (Figure 27), which showed a reflection in fluctuations on the gas composition graph (Figure 15). This was also not represented in the numerical model because it was uniform. Perfect matches were not obtained because of the heterogeneities in the oil and rock composition, fractures created in the combustion tube, and heterogenities of the packing force. However, in the stable region, the average $CO_2$ value approached 12%, while the numerical model indicated the $CO_2$ value to be around 14%. During the experiment, the average CO level was around 3%, and reached peak values of around 5-6%. The numerical model predicted the CO level to be more constant, accounting 5%.

Production was also not matched perfectly (Figure 39 C). The difference between the cumulative oil recovery, achieved in the experiment and in the simulation, was 27%.

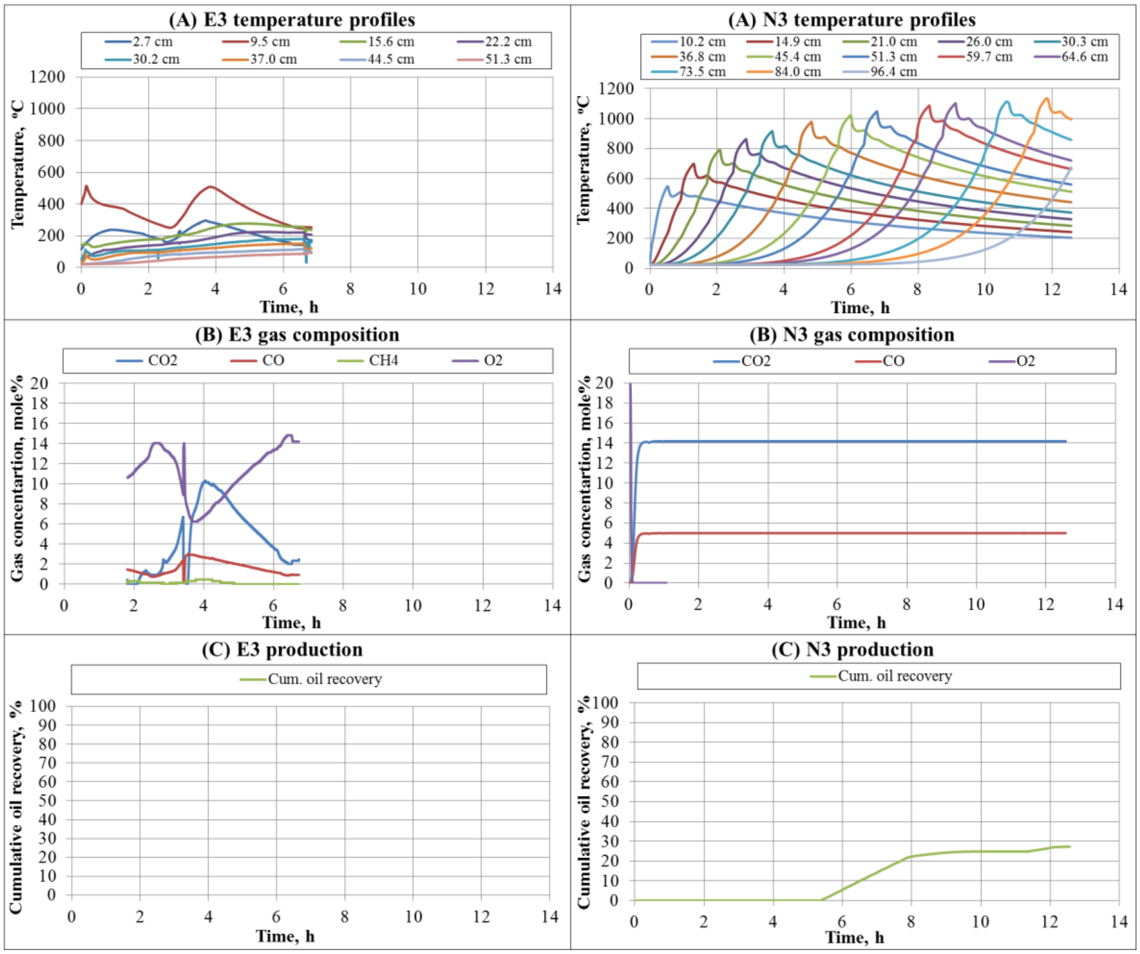

**Figure 41.** Experimental (E3) and numerical simulation (N3) results

To estimate the effect of water on ISC numerically, the initial water saturation was set to 0%, and the simulation study was repeated. Conditions of this numerical run were similar to those of E3. Results of this study are summarized in Figure 41.

As can be seen in Figure 41, the kinetic model proposed for E5 was not able to reproduce E3 experimental trends. To mimic experimental results, the model should be tuned. The experimental results indicated that low amount of initial water saturation cannot maintain HTO reactions. This was not observed in the numerical study.

However, some observations from the numerical study overlap with experimental trends. In N5, the combustion front velocity was estimated as 11.8 cm/h. While in N3, the combustion front velocity, estimated between positions 64.6 and 73.5 cm, corresponded to only 7.25 cm/h. The decrease in the initial water saturation resulted in the combustion front velocity decrease.

The decrease in fluid mobility reflected in the higher combustion front temperatures (Figure 41 A) and in the decreased oil production (Figure 41 C).

# CHAPTER V

# CONCLUSIONS AND RECOMMENDATIONS

Seven ISC tube experiments were performed to investigate the effect of the initial water and oil saturation on dry forward ISC performance. Research was performed on the Peace River bitumen (7.5 $^o$API). During the experimental runs, the initial bitumen saturation varied between 31.23% and 54.86%. The initial water saturation varied between 0% and 36.87%.

The Peace River bitumen is a good candidate for ISC application. However, experimental results indicated that the presence of the initial water is one of the factors determining the success of dry forward ISC. Better ISC front propagation characteristics were achieved for the runs with higher initial water saturation. The stability of the ISC front was not achieved during the experiments in which initial water saturation was kept at 0%.

It was also proved that initial water saturation improves heat transfer in the reservoir. The effect of initial water saturation on dry forward ISC performance was also found in the combustion front velocity. Analysis of the experimental data clearly indicated that the combustion front velocity increases with the increasing initial water saturation.

Experimental results also indicated that the initial water saturation affects ISC reaction kinetics, as the average value of the $CO_2$ concentration in the effluent gas increases with the increase in the initial water saturation. A low amount of initial water cannot support

HTO reactions. With the increasing initial water saturation, the LTO mode changes to the HTO.

In addition, a different type of coke-like residue was formed during the experiments' preheating stage, where the initial water saturation was higher.

The initial water saturation also affected the value of the average and the maximum combustion front temperatures. Both temperature characteristics increased with the increase in the initial water saturation.

The cumulative oil recovery, one of the most important factors for an economical evaluation of the ISC project success, also showed a tendency to increase with the increasing initial water saturation. A dependency was found between the initial water saturation and the production delay time. The gap between the air injection start time and the production start time revealed a tendency to decrease with the increasing initial water saturation.

The initial water saturation also determined in-situ upgrade of oil. Lighter oil was received as an outcome for the cases, in which the initial water saturation was higher.

One experiment was simulated numerically. It was proved, that with the lack of information on oil, a simplified reaction scheme of just two reactions can be used. The acquired model was capable of reproducing experimental trends, but perfect matches were not achieved.

For the further improvement of numerical simulation, oxidation behavior of the Peace River bitumen should be investigated in order to generate more adequate kinetic reaction scheme. This will allow the numerical model to reproduce transition period observed in the experiments.

Different type of coke-like residue was formed in the top section of the combustion tube for the cases in which initial water saturation existed. This type of coke was formed under the nitrogen injection conditions and its properties differ from the properties of the coke-like residue left unconsumed in the burned zone. Better matches can be achieved for the temperature profiles with the introduction of the second type of coke into the numerical model.

For the better match of production, wettability characteristics should be investigated for the Peace River bitumen and two-phase relative permeability curves should be generated.

Sensitivity study should be performed to check the effect of the grid size.

# NOMENCLATURE

| | |
|---|---|
| EOR | Enhanced Oil Recovery |
| HWI | Hot Water Injection |
| ISC | In-Situ Combustion |
| SARA | Saturate, Aromatic, Resin, Asphaltene |
| LTO | Low Temperature Oxidation |
| HTO | High Temperature Oxidation |
| CT | Computed Tomography |
| $m_{sp}$ | Mass of Packed Sample, g |
| $m_{ig}$ | Mass of Injected Gas, g |
| $m_{sp-m}$ | Mass of Postmortem Sample, g |
| $m_{pl}$ | Mass of Produced Liquid, g |
| $m_{pg}$ | Mass of Produced Gas, g |
| $q_i$ | Injection Flow Rate, $m^3$/h |
| $t_i$ | Injection Time, h |
| $P_i$ | Injection Pressure, kPa |
| $M$ | Gas Mixture Molar Mass, kg/mol |
| $z\,|(689\ kPa, 300\ K)$ | Gas Mixture Compressibility Factor at 689 kPa and 300 K |
| $R$ | Universal Gas Constant, 8.31 J/mol-K |
| $T_i$ | Injection Temperature, K |
| $y_i$ | Mixture Component Molar Fraction, frac. |

| | |
|---|---|
| $M_i$ | Mixture Component Molar Mass, kg/mol |
| STARS | Steam Thermal Advanced Reservoir Simulator |
| CMG | Computer Modeling Group |
| $k_{mix}$ | Thermal Conductivity of Saturated Rock, J/m-hr-$^{o}$C |
| $k_o$ | Thermal Conductivity of Oil, J/m-hr-$^{o}$C |
| $k_w$ | Thermal Conductivity of Water, J/m-hr-$^{o}$C |
| $k_g$ | Thermal Conductivity of Gas, J/m-hr-$^{o}$C |
| $k_s$ | Thermal Conductivity of Solid, J/m-hr-$^{o}$C |
| $k_r$ | Thermal Conductivity of Rock, J/m-hr-$^{o}$C |
| $S_o$ | Oil Saturation, frac. |
| $S_w$ | Water Saturation, frac. |
| $S_g$ | Gas Saturation, frac. |
| $m$ | Porosity, frac. |
| $m_f$ | Porosity, Saturated With Fluids Only, frac. |
| $S_{orw}$ | Residual Oil Saturation for Water Injection, frac. |
| $S_{org}$ | Residual Oil Saturation for Gas Injection, frac. |
| $\mu_i$ | Liquid Component Viscosity, cp |
| $T$ | Temperature, K |
| $a$ | Viscosity-Temperature Dependency Coefficient, cp |
| $b$ | Viscosity-Temperature Dependency Coefficient, K |
| $r$ | Reaction Rate |
| $k$ | Reaction Rate Constant |

| | |
|---|---|
| $C_f$ | Fuel Concentration, kg/m$^3$ |
| $P_{O_2}$ | Oxygen Partial Pressure, kPa |
| $\alpha$ | Reaction Order in Respect to Oxygen Partial Pressure |
| $\beta$ | Reaction Order in Respect to Fuel Concentration |
| $A$ | Frequency Factor |
| $E_a$ | Activation Energy, J/mol |

# REFERENCES

Akin, S., Kovscek, A.R. 2003. Computed tomography in petroleum engineering research, applications of X-ray computed tomography in the geosciences. London, UK: Special Publication, Geological Society.

Alamatsaz, A.R., Moore, R.G., Mehta, S.A. , Ursenbach, M.G. . 2011. Experimental investigation of in situ combustion at low air fluxes. SPE Western North American Region Meeting, Anchorage, Alaska, USA. SPE-144517-MS.

Alexander, J.D., Martin, W.L., Dew, J.N. 1962. Factors affecting fuel availability and composition during in situ combustion. JPT **14** (10). SPE-296-PA.

Ashrafi, M., Souraki, Y., O., Torsaeter. 2012. Effect of temperature on Athabasca type heavy oil-water relative permeability curves in glass bead packs. Energy and Environment Research **2** (2). 20109-71316-1-PB.

Attanasi, E.D., Meyer, R.F. 2010. Natural bitumen and extra-heavy oil. World Energy Council. London, UK. http://www.worldenergy.org/documents/ser_2010_report_1.pdf.

Bae, J.H. 1977. Characterization of crude oil for fireflooding using thermal analysis methods. SPE Journal **17** (3). SPE-6173-PA.

Bagci, S. 1998. Estimation of combustion zone thickness during in situ combustion processes. Energy & Fuels **12** (6). ef980013m.

Bagci, S., Celebioglu, S. 2004. Light oil combustion with metallic additives in limestone medium. Canadian International Petroleum Conference, Calgary, Alberta, Canada. PETSOC-2004-086.

Bailey, H.R., Larkin, B.K. 1959. Heat conduction in underground combustion. Trans., AIME **216**. 1134-G.

Bailey, H.R., Larkin, B.K. 1960. Conduction-convection in underground combustion. Trans., AIME **219**. SPE-1482-G.

Barth, T., Borgund, A.E., Hopland, A.L. 1989. Generation of organic compounds by hydrous pyrolysis of Kimmeridge oil shale - bulk results and activation energy calculations. Organic Geochemistry **14** (1). 0146-6380/89.

Bayliss, P., Levinson, A. 1976. Mineralogical review of the Alberta oil sand deposits (lower Cretaceous, Mannville group). Bulletin of Canadian Petroleum Geology **24** (2)

Belgrave, J.D.M., Moore, R.G., Ursenbach, M.G., Bennion, D.W. 1993. A comprehensive approach to in-situ combustion modeling. SPE Advanced Technology Series **1** (1). SPE-20250-PA.

Benham, A.L., Poettman, F.H. 1958. The Thermal Recovery Process - An Analysis of Laboratory Combustion Data. JPT **10** (9). SPE-1022-G.

Bousaid, I.S., Ramey, H.J. 1968. Oxidation of crude oil in porous media. SPE Journal **8** (2). SPE-1937-PA.

Brons, G., Siskin, M. 1994. Bitumen chemical changes during aquathermolytic treatments of Cold Lake tar sands. Fuel **73** (2). 90112-0.

Burger, J.G. 1972. Chemical aspects of in-situ combustion - heat of combustion and kinetics. SPE Journal **12** (5). SPE-3599-PA.

Butler, R. M. 1991. Thermal recovery of oil and bitumen. New Jersey, USA, Prentice Hall Inc.

Castanier, L. M., Baena, C. J., Holt, R. J., Brigham, W. E., Tavares, C. 1992. In situ combustion with metallic additives. SPE Latin America Petroleum Engineering Conference, Caracas, Venezuela. SPE-23708-MS.

Chattopadhyay, S. K., Ram, B., Bhattacharya, R.N., Das, T.K. 2004. Enhanced oil recovery by in-situ combustion process in santhal field of Cambay basin, Mehsana, Gujarat, India - a case study. SPE/DOE Symposium on Improved Oil Recovery, Tulsa, Oklahoma, USA. SPE-89451-MS.

Chen, H.H., Mojelski, T.W., Payznat, J.D., Lown, E.M., Strausz, O.P. 1990. Hydrous pyrolysis of Alberta oil sands. 1990 Eastern Oil Shale Symposium, Lexington, Kentucky, USA, IMMR90/201.

Christensen, J. R., Darche, G., Dechelette, B., Ma, H., Sammon, P.H. 2004. Applications of dynamic gridding to thermal simulations. SPE International Thermal Operations and Heavy Oil Symposium and Western Regional Meeting, Bakersfield, California. SPE-86969-MS.

Chu, C. 1963. Two-dimensional analysis of a radial heat wave. JPT **15** (10). SPE-560-PA.

Chu, C. 1964. The vaporization-condensation phenomenon in a linear heat wave. SPE Journal **4** (2). SPE-680-PA.

CMG (Computer Modeling Group). STARS (version 2009) [Computer programm]. Calgary, Canada. Available at http://www.cmgl.ca.

Conti, J., Holtberg, P. 2011. International energy outlook. U.S. Energy Information Administration. Washington, DC, USA. http://www.eia.gov/forecasts/ieo/pdf/0484(2011).pdf.

Crookston, R.B., Culham, W.E., Chen, W.H. 1979. A numerical simulation model for thermal recovery processes. SPE Journal **19** (1). SPE-6724-PA.

Davidson, L.B. 1969. The effect of temperature on the permeability ratio of different fluid pairs in two-phase systems. JPT **21** (8). SPE-2298-PA.

Dayal, H.S., Bhushan, B.V., Mitra, S., Sinha, S.K, Sur, S. 2010. In-situ combustion : opportunities and anxieties. SPE Oil and Gas India Conference and Exhibition, Mumbai, India. SPE-126241-MS.

de Zwart, A. H., van Batenburg, D. W., Blom, C. P. A., Tsolakidis, A., Glandt, C. A. , Boerrigter, C. A. 2008. The modeling challenge of high pressure air injection. SPE/DOE Symposium on Improved Oil Recovery, Tulsa, Oklahoma, USA. SPE-113917-MS.

Dechelette, B., Heugas, O., Quenault, G., Bothua, J., Christensen, J.R. 2006. Air injection-improved determination of the reaction scheme with ramped temperature experiment and numerical simulation. JCPT **45** (1). PETSOC-06-01-03.

Dehghani, K., Kamath, J. 2001. High-temperature blowdown experiments in a vuggy carbonate core. SPE Journal **6** (3). SPE-74136-PA.

Dehghani, K., Meyer, R.F., Duran, H., Kumar, M., deZabala, E.F. 1997. An experimental and numerical study of in-situ steamdrive during cyclic steaming. SPE Reservoir Engineering **12** (2). SPE-30749-PA.

DOE. 2013. EOR drawings, http://www.netl.doe.gov/technologies/oil-gas/publications/eordrawings/bw/bwinsitu_comb.pdf (downloaded July 28 2013).

Drici, O., Vossoughi, S. 1985. Study of the surface area effect on crude oil combustion by thermal analysis techniques. JPT **37** (4). SPE-13389-PA.

Druganova, E., Surguchev, L. M., Ibatullin, R. R. 2010. Air injection at Mordovo-Karmalskoye field: simulation and IOR evaluation. SPE Russian Oil and Gas Conference and Exhibition, Moscow, Russia. SPE-136020-MS.

Dutta, R., Dutta, W., McCaffrey, M., Gray, K. 2000. Thermal cracking of Athabasca bitumen: influence of steam on reaction chemistry. Energy & Fuels **14** (3). ef990223e

Dutta, R., McCaffrey, M., Gray, M. 1999. Effect of steam on coking chemistry of Athabasca bitumen. Abstracts Of Papers Of The American Chemical Society **218**. 08-99-0805.

Farouq Ali, S.M., S., Thomas. 1994. A realistic look at enhanced oil recovery. Scientia Iranica **1** (3). si010304.

Freitag, N.P., Exelby, D.R., Neate, C.J. 2006. A SARA-based model for simulating the pyrolysis reactions that occur in high-temperature EOR processes. JCPT **45** (3). PETSOC-06-03-02.

Fumoto, E., Sato, S., Takanohashi, T. 2010. Production of light oil by oxidative cracking of oil sand bitumen using iron oxide catalysts in a steam atmosphere. Energy & Fuels **25** (2). ef101068m.

Gerritsen, M. , Kovscek, A. , Castanier, L. M., Nilsson, J., Younis, R. , He, B. . 2004. Experimental investigation and high resolution simulator of in-situ combustion processes; 1. Simulator design and improved combustion with metallic additives. SPE International Thermal Operations and Heavy Oil Symposium and Western Regional Meeting, Bakersfield, California, USA. SPE-86962-MS.

Glatz, G., Hascakir, B., Clemens, T., Castanier, L. M., Kovscek, A. R. 2011. Kinetic cell and combustion tube results for a central european crude. SPE Annual Technical Conference and Exhibition, Denver, Colorado, USA. SPE-146089-MS.

Gutierrez, D., Moore, R.G., Ursenbach, M.G., Mehta, S.A. 2012. The ABCs of in-situ-combustion simulations: from laboratory experiments to field scale. JCPT **51** (4). SPE-148754-PA.

Gutierrez, D., Skoreyko, F., Moore, R. G., Mehta, S. A., Ursenbach, M. G. 2009. The challenge of predicting field performance of air injection projects based on laboratory and numerical modelling. JCPT **48** (4). PETSOC-09-04-23-DA.

Hamm, R.A., Ong, T.S. 1995. Enhanced steam-assisted gravity drainage: a new horizontal well recovery process for Peace River, Canada. JCPT **34** (4). PETSOC-95-04-03.

Hascakir, B., Glatz, G., Kovscek, A.R. 2011. In-situ combustion dynamics visualized with X-ray computed tomography. SPE Journal **16** (3). SPE-135186-PA.

Hascakir, B., Ross, C.M., Castanier, L.M., Kovscek, A.R. 2011. Fuel formation during in-situ combustion of heavy oil. SPE Annual Technical Conference and Exhibition, Denver, Colorado, USA. SPE-146867-MS.

Hein, F.J. 2000. Historical overview of the Fort McMurray area and oil sands industry in northeast Alberta. Alberta Geological Survey. Edmonton, Alberta, Canada. gov.ab.ca/publications/ESR/PDF/ESR_2000_05.pdf.

Hongfu, F., Yongjian, L., Liying, Z., Xiaofei, Z. 2002. The study on composition changes of heavy oils during steam stimulation processes. Fuel **81** (13). S001623610200100X.

Howabd, F.A. 1923. Method of operating oil wells. USA Patent No. 1473348.

Jain, P., Stenby, E.H., Solms, N.V. 2010. Compositional simulation of in-situ combustion EOR: a study of process characteristics. SPE Improved Oil Recovery Symposium, Tulsa, Oklahoma, USA. SPE-129869-MS.

Johnson, L., Romanowski, L. 1987. Evaluation of steam-to-oxygen ratios for forward combustion in Asphalt Ridge tar sand. Western Research Inst. Laramie, Wyoming, USA. http://www.netl.doe.gov/kmd/cds/disk44/k-thermal recovery/doemc11076-2441.pdf.

Lee, D.G., N.A., Noureldin. 1989. Effect of water on the low-temperature oxidation of heavy oil. Energy & Fuels **3** (6). ef00018a009.

Lewan, M. D. 1985. Evaluation of petroleum generation by hydrous pyrolysis experimentation. Philosophical Transactions of the Royal Society of London, Series A: Mathematical and Physical Sciences **315** (1531). 37708.

Lewan, M.D. 1991. Primary oil migration and expulsion as determined by hydrous pyrolysis. 13th World Petroleum Congress, Buenos Aires, Brazil. WPC-24124.

Liang, J., Guan, W., Wang, B. 2013. Feasibility study of in-situ combustion huff and puff for EOR in super-deep heavy oil reservoir. 6th International Petroleum Technology Conference, Beijing, China. IPTC-16408-MS.

Mahasneh, M. A. 2012. Determine factors affecting fuel availability and composition by cell oxidation during laboratory test for in-situ combustion. Contemporary Engineering Sciences **5** (4). CES1-4-2012-2.

Mamora, D.D., Ramey, H.J., Brigham, W.E., Castanier, L.M. 1993. Kineics of in situ combustion. Stanford University. http://www.osti.gov/bridge/servlets/purl/10175378-2qlsvu/10175378.pdf.

Marjerrison, D.M., Fassihi, M.R. 1992. A Procedure for Scaling Heavy-Oil Combustion Tube Results to a Field Model. SPE/DOE Enhanced Oil Recovery Symposium, Tulsa, Oklahoma, USA. SPE-24175-MS.

Markano, N., Benneth, B., Larter, S. 2013. The geomechanical toolbox to monitoring thermal recovery operations in oil sands and heavy oil reservoirs. GeoConvention 2013: Integration, Calgary, Canada. 467.

Markano, N., Huang, H., Bennett, B., Showdon, L., Larter, S. 2010. Using molecular transformations to monitor in situ upgrading operations in oil sands and heavy oil reservoirs. AAPG Hedberg conference, Vail, Colorado, USA. 74.

Martin, W.L., Alexander, J.D., Dew, J.N. 1958. Process variables of in situ combustion. Trans., AIME **213**. SPE-914-G.

Meyer, R.F., Attanasi, E.D., Freeman, P.A. 2007. Heavy oil and natural bitumen resources in geological basins of the world. U.S. Geological Survey. Reston, Virginia, USA. http://pubs.usgs.gov/of/2007/1084/.

Monin, J.C., Audibert, A. 1988. Thermal cracking of heavy-oil/mineral matrix systems. SPE Reservoir Engineering **3** (4). SPE-16269-PA.

Moritis, G. 2002. California steam EOR produces less; other EOR continues. Oil & Gas Journal **100** (15). 301388.

Mossop, G.D. 1982. Geology of the Athabasca Oil Sand. Science **207** (4427). 1683886

Novelline, R.A., L.F., Squire. 1997. Squire's fundamentals of radiology, 5 edition. Cambridge, Massachusetts, Harvard University Press.

Peters, K.E., Moldowan, J.M., Sundararaman, P. 1990. Effects of hydrous pyrolysis on biomarker thermal maturity parameters: Monterey Phosphatic and Siliceous members. Organic Geochemistry **15** (3). 146-6380.

Poston, S.W., Ysrael, S., Hossain, A.K.M.S., Montgomery III, E.F. 1970. The effect of temperature on irreducible water saturation and relative permeability of unconsolidated sands. SPE Journal **10** (2). SPE-1897-PA.

Prats, M. 1982. Thermal recovery. New York, H.L. Doherty Memorial Fund of AIME : SPE of AIME.

Ramey, H.J. 1959. Transient heat conduction during radial movement of a cylindrical heat source - applications to the thermal recovery process. Trans., AIME **216**. SPE-1133-G.

Sarathi, P.S. 1999. In-situ combustion handbook - principles and practices. Bartlesville, Oklahoma, USA, National Technology Information Service.

Satman, A. 1979. In-situ combustion models for the steam plateau and for fieldwide oil recovery. PhD, Energy Resources Engineering, Stanford University, Stanford, California, USA.

Shen, C. 2002. Limitations and potentials of in-situ combustion processes for heavy oil reservoirs. Canadian International Petroleum Conference, Calgary, Alberta, Canada. PETSOC-2002-217.

Smith, J.T., Farouq Ali, S.M. 1971. Simulation of in-situ combustion in a two-dimensional system. Fall Meeting of the Society of Petroleum Engineers of AIME, New Orleans, Louisiana, USA. SPE-3594-MS.

Spreight, J. G. 2009. Enhanced recovery methods for heavy oil and tar sands. Houston, Gulf Publishing Company.

Stone, H.L. 1973. Estimation of three-phase relative permeability and residual oil data. JCPT **12** (4). PETSOC-73-04-06.

Svrcek, W.Y., Mehrotra, A.K. 1989. Properties of Peace River bitumen saturated with field gas mixtures. JCPT **28** (2). PETSOC-89-02-01.

Taber, J.J., Martin, F.D., Seright, R.S. 1997. EOR Screening criteria revisited - Part 1: introduction to screening criteria and enhanced recovery field projects. SPE Reservoir Engineering **12** (3). SPE-35385-PA.

Takamura, K., Chow, R.S. 1983. A mechanism for initiation of bitumen displacement from oil sand. JCPT **22** (6). PETSOC-83-06-01.

Tingas, J., Greaves, M., Young, T. J. 1996. Field scale simulation study of in-situ combustion in high pressure light oil reservoirs. SPE/DOE Improved Oil Recovery Symposium, Tulsa, Oklahoma, USA. SPE-35395-MS.

Urban, D.L., Udell, K.S. 1990. The effects of steam on the combustion of oil on sand. SPE Reservoir Engineering **5** (2). SPE-18073-PA.

van Batenburg, D. W., Bosch, M., Boerrigter, P. M., de Zwart, A. H., Vink, J. C. 2011. Application of dynamic gridding techniques to IOR/EOR-processes. SPE Reservoir Simulation Symposium, The Woodlands, Texas, USA. SPE-141711-MS.

Vossoughi, S., Willhite, G. P., Kritikos, W. P., Guvenir, I. M., El Shoubary, Y. 1982. Automation of an in-situ combustion tube and study of the effect of clay on the in-situ combustion process. SPE Journal **22** (4). SPE-10320-MS.

Wang, J., McGee, B., Kantzas, A. 2006. Calculations of the effect of boiling water on bitumen production. Canadian International Petroleum Conference, Calgary, Alberta, Canada. PETSOC-2006-046.

Wilson, L.A., Reed, R.L., Reed, D.W., Clay, R.R., Harrison, N.H. 1963. Some effects of pressure on forward and reverse combustion. SPE Journal **3** (2). SPE-457-PA.

Withjack, E.M., Devier, C., Michael, G. 2003. The role of X-ray computed tomography in core analysis. SPE Western Regional/AAPG Pacific Section Joint Meeting, Long Beach, California, USA. SPE-83467-MS.

Xia, T.X., Greaves, M. 2001. Downhole upgrading Athabasca tar sand bitumen using THAI - SARA analysis. SPE International Thermal Operations and Heavy Oil Symposium, Porlamar, Margarita Island, Venezuela. SPE-69693-MS.

Xu, H.H., Okazawa, N., Moore, R.G. , Mehta, S.A., Laureshen, C.J., Ursenbach, D.W., Mallory, D. 2000. In situ upgrading of heavy oil. Canadian International Petroleum Conference, Calgary, Alberta. PETSOC-2000-030.

# APPENDIX A

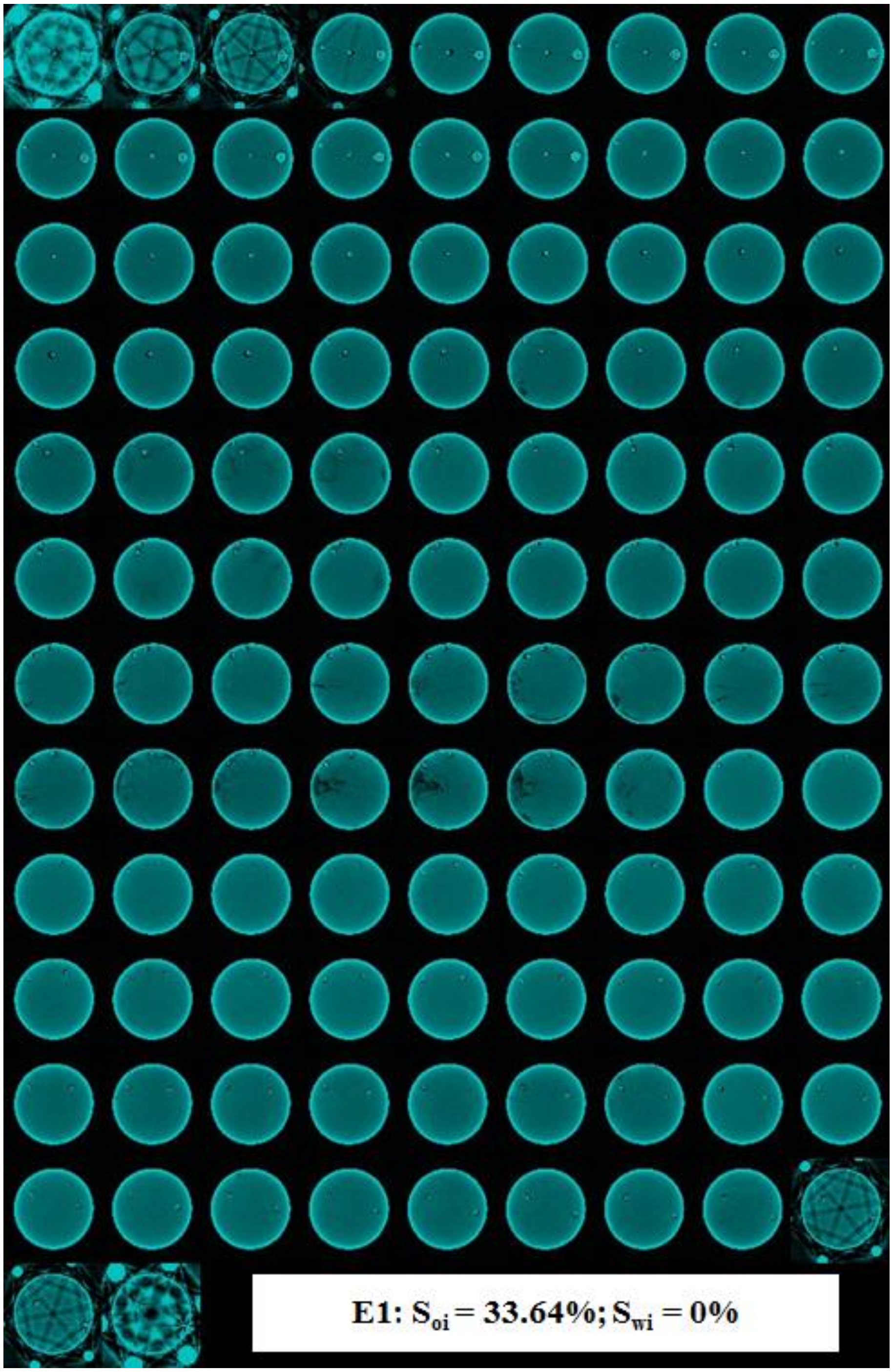

**Figure 42.** E1 combustion tube cross-sectional CT images, every 9 mm interval

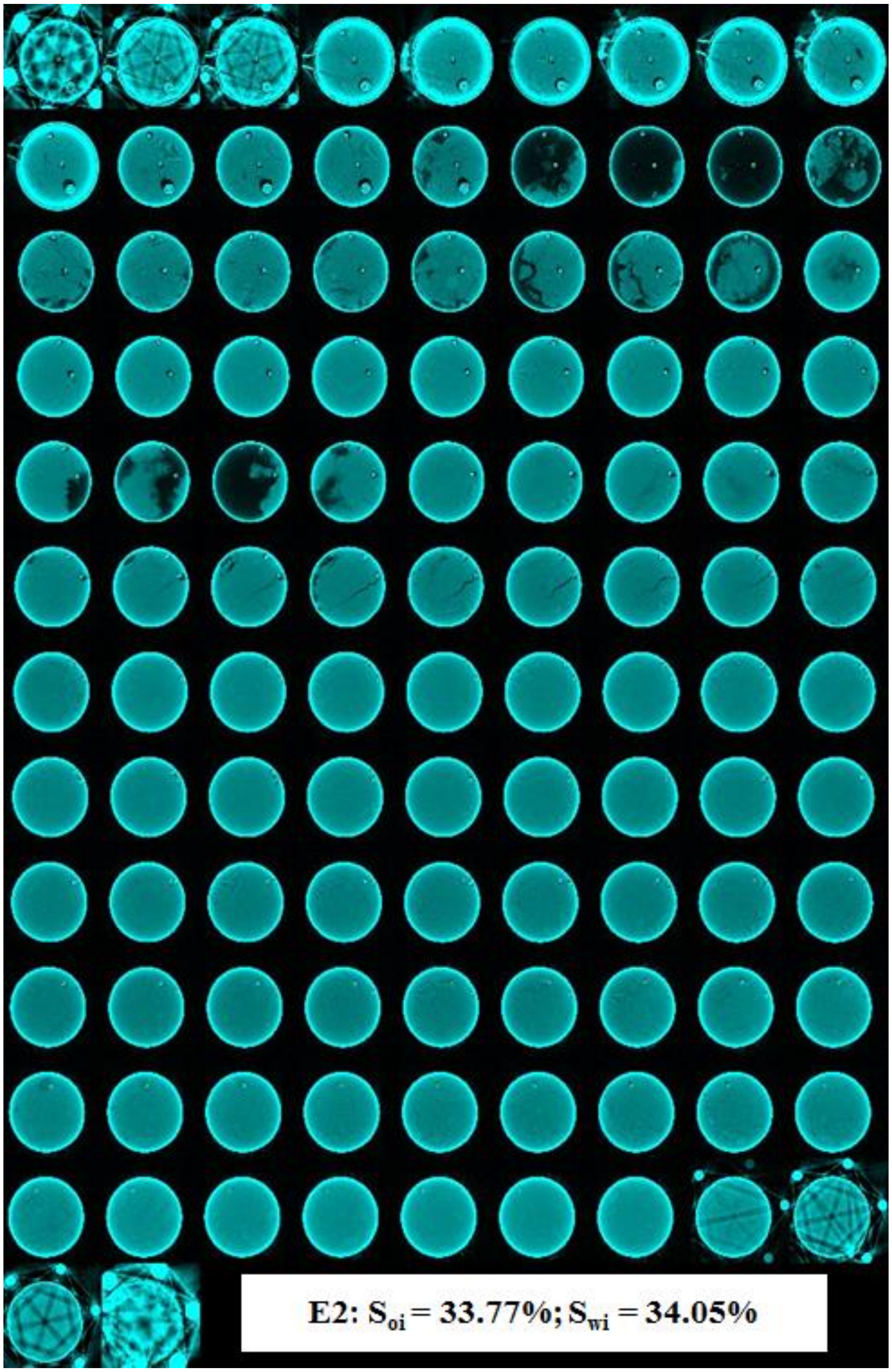

**Figure 43.** E2 combustion tube cross-sectional CT images, every 9 mm interval

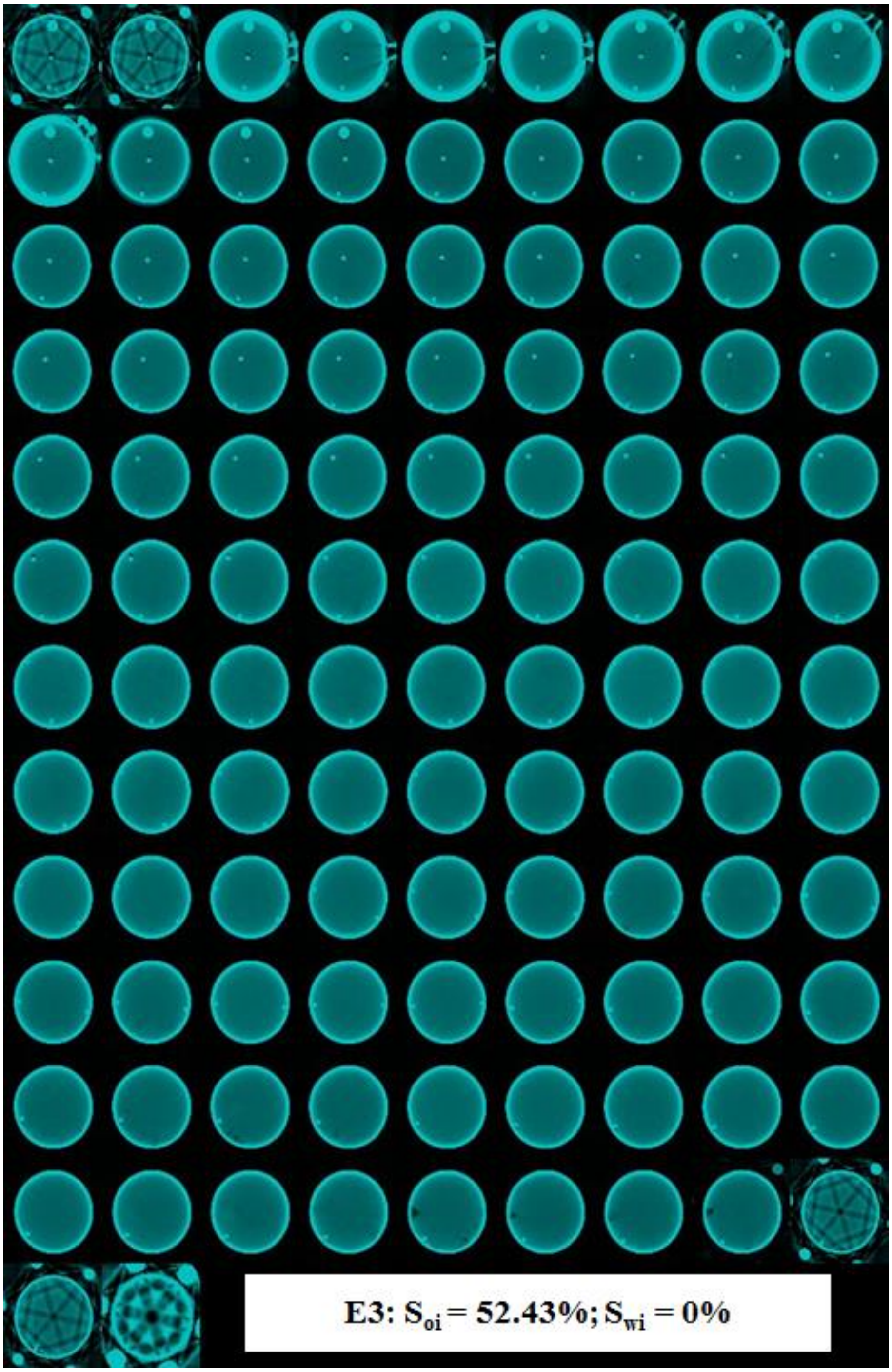

**Figure 44.** E3 combustion tube cross-sectional CT images, every 9 mm interval

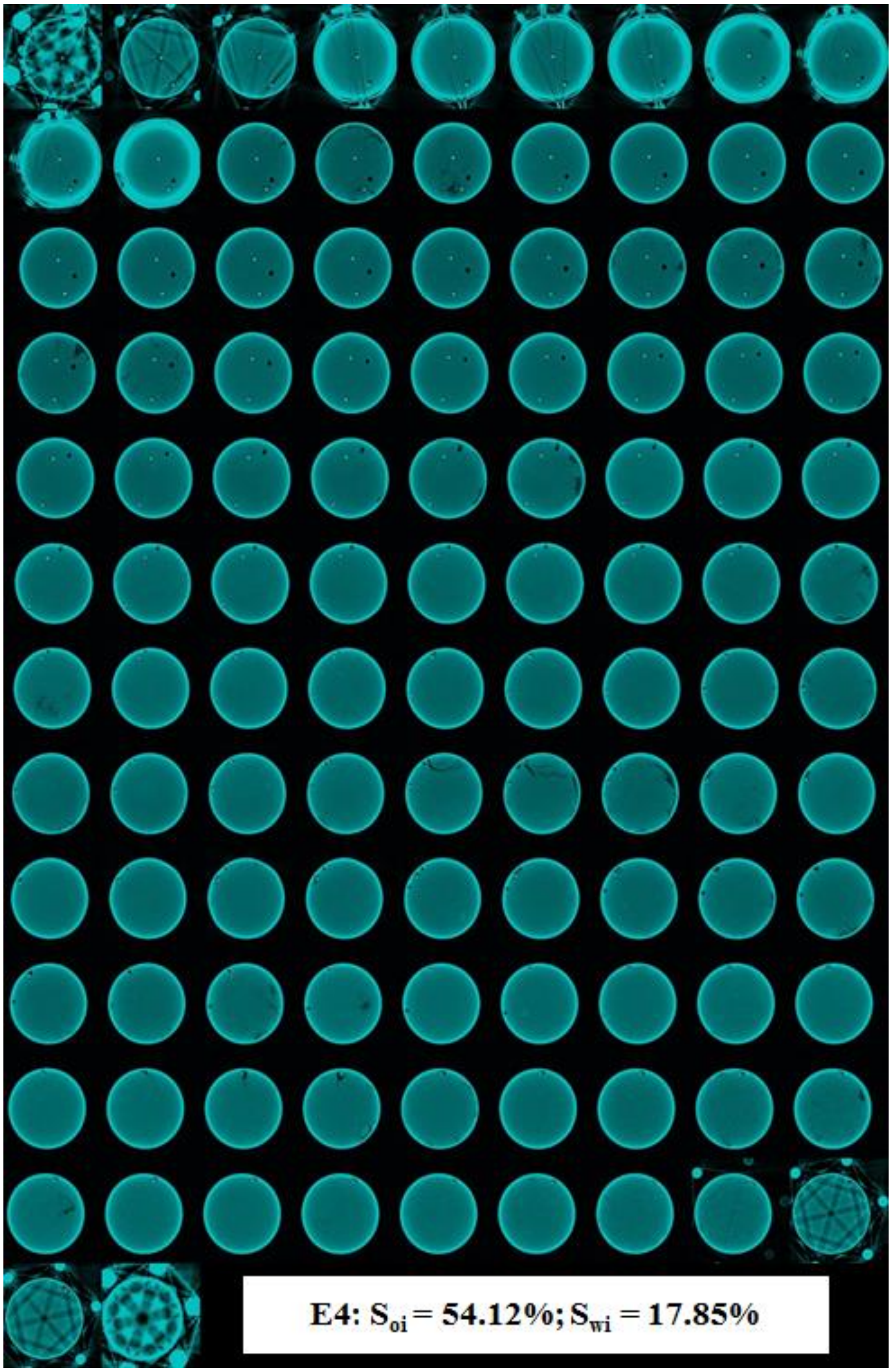

**Figure 45.** E4 combustion tube cross-sectional CT images, every 9 mm interval

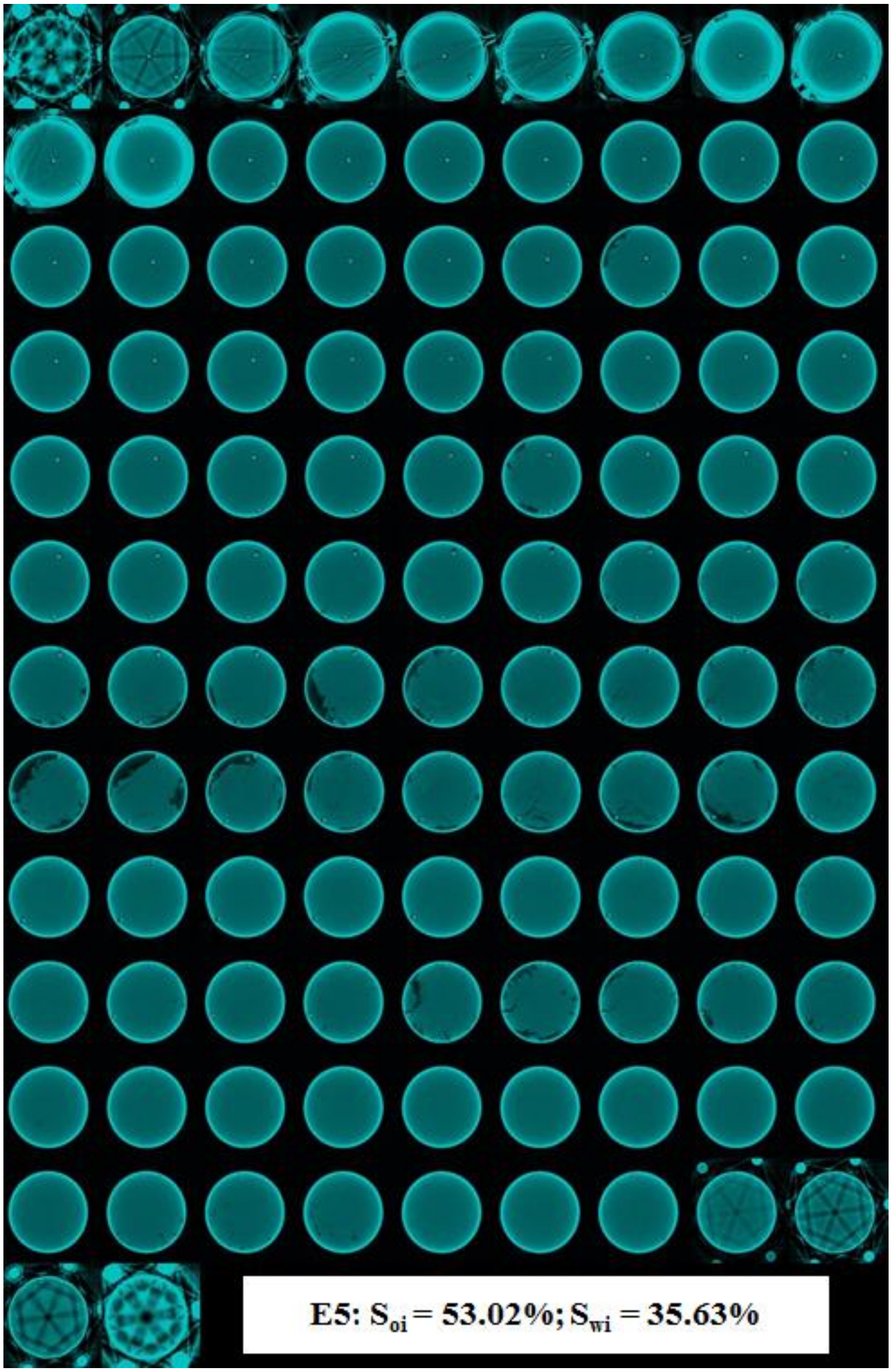

**Figure 46.** E5 combustion tube cross-sectional CT images, every 9 mm interval

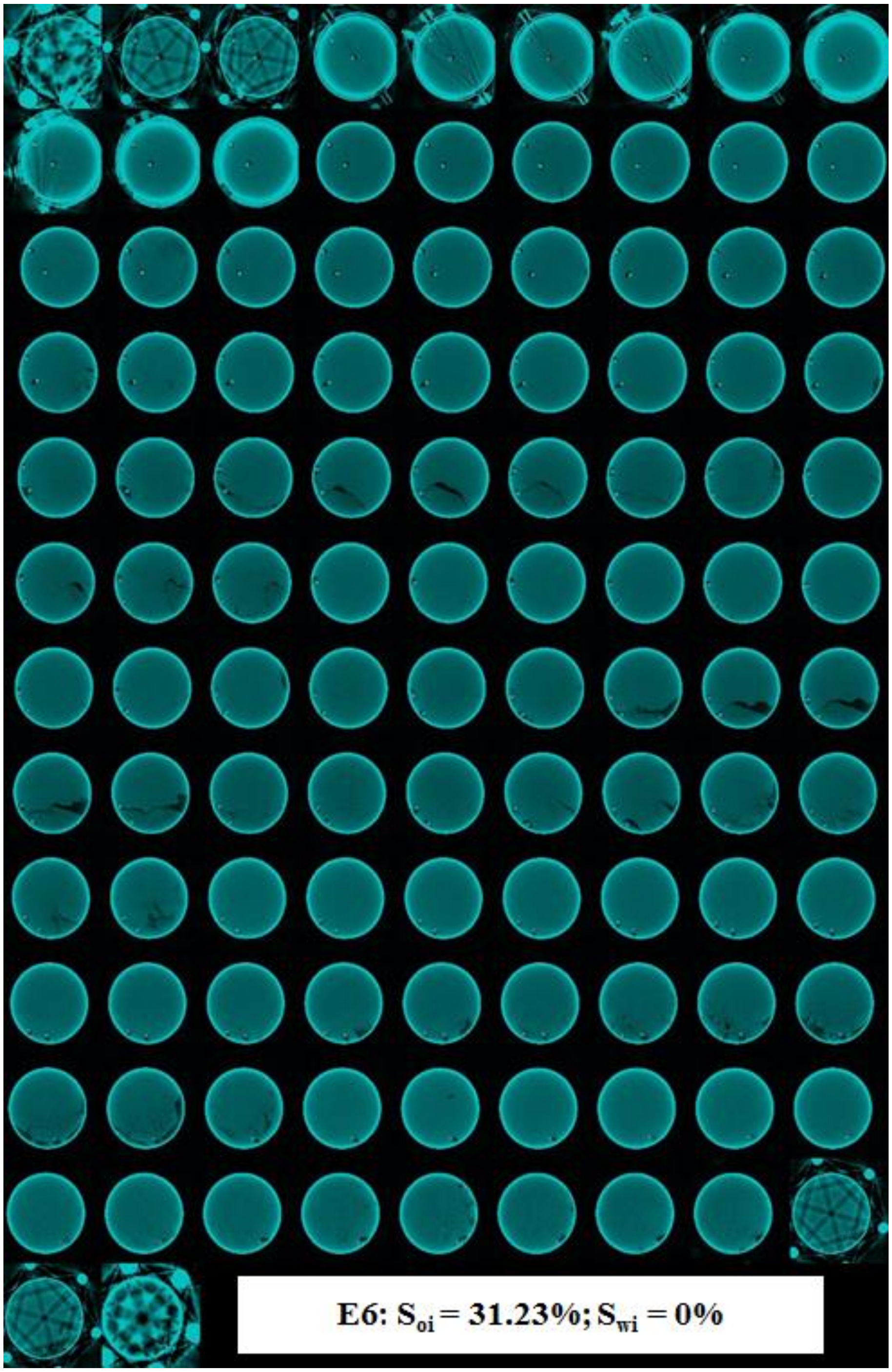

**Figure 47.** E6 combustion tube cross-sectional CT images, every 9 mm interval

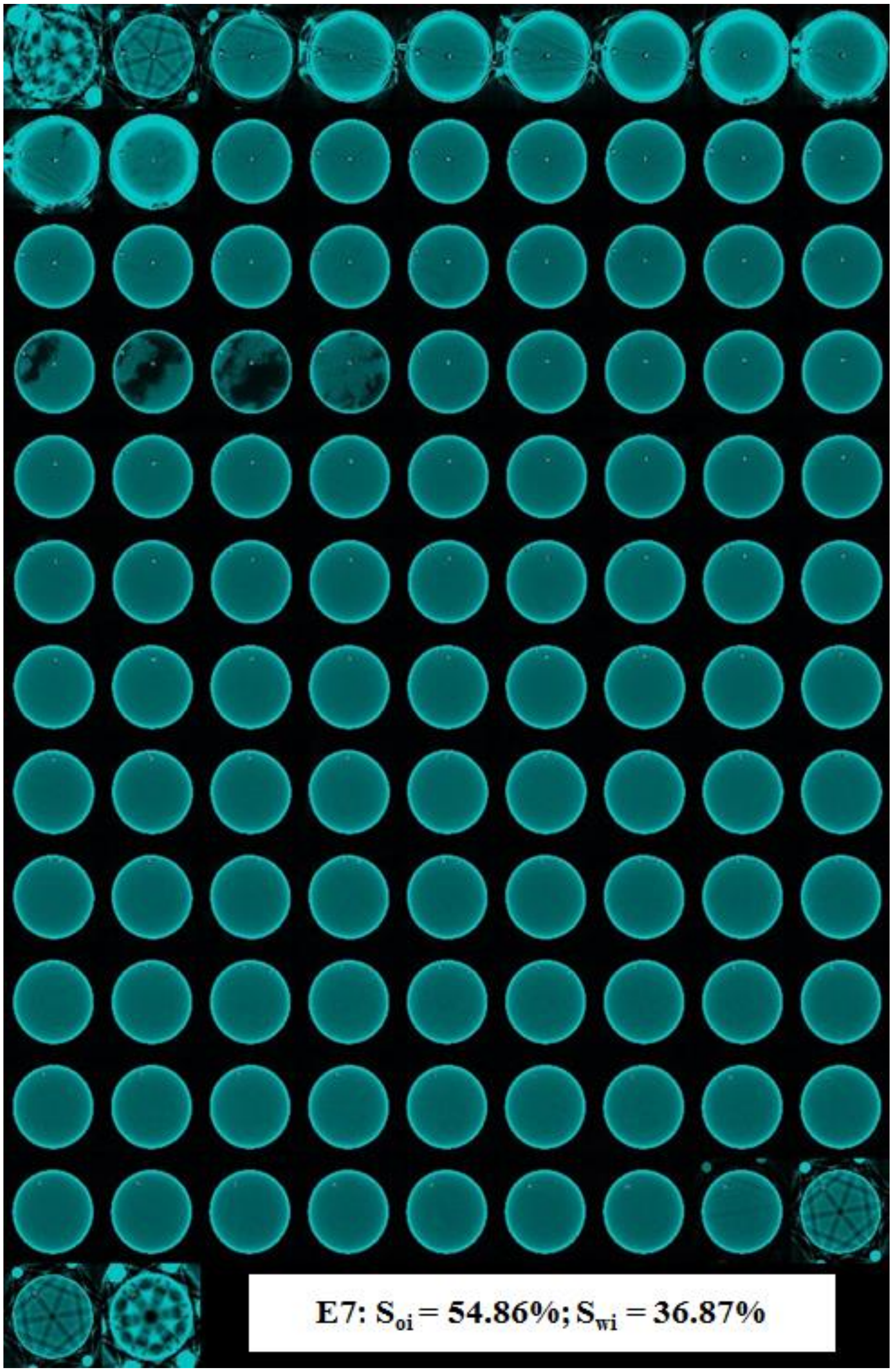

**Figure 48.** E7 combustion tube cross-sectional CT images, every 9 mm interval